Spring 5-15-2018

Increasing pH in cancer: enabling a new therapeutic paradigm using novel carbonate nanoparticles

Avik Som
Washington University in St. Louis

Recommended Citation

Som, Avik, "Increasing pH in cancer: enabling a new therapeutic paradigm using novel carbonate nanoparticles" (2018). *McKelvey School of Engineering Theses & Dissertations*. 332.
https://openscholarship.wustl.edu/eng_etds/332

WASHINGTON UNIVERSITY IN ST. LOUIS

School of Engineering & Applied Science

Department of Biomedical Engineering

Dissertation Examination Committee:

Samuel Achilefu, Chair
Jason Mills
Shelly Sakiyama-Elbert
Srikanth Singamaneni
Lihong Wang

Increasing pH in Cancer: Enabling a New Therapeutic Paradigm Using Novel Carbonate Nanoparticles

by
Avik Som

A dissertation presented to
The Graduate School
of Washington University in
partial fulfillment of the
requirements for the degree
of Doctor of Philosophy

May 2018
St. Louis, Missouri

Table of Contents

List of Figures

Chapter 1: Introduction

Chapter 2: Effect of extracellular pH on stromal cells

Chapter 3: Simulation of pH modulation using $CaCO_3$

Chapter 4: Synthesis and Stabilization of Nano-$CaCO_3$

Chapter 5 Biodistribution and Toxicity screening of $CaCO_3$ *in vivo*

Chapter 6 Systemic Administration of Nano-$CaCO_3$ inhibits tumor growth and metastasis via local pH increase

Acknowledgments

First, I'd like to thank my parents and sister for being so supportive during this process of discovery. My father for teaching me how to pursue math, science, and school, and my mother for teaching me how to communicate and be creative. I'd like to thank my sister for believing in me and supporting me.

I'd like to thank my mentor, Professor Samuel Achilefu who has given me incredible freedom and advice at the expense of many many hours into the night. Dr. Achilefu has been an incredible mentor in both supporting my aspirations as well as giving me an idol to live up to, both as a scientist and as a person.

I'd like to thank my committee, Dr. Wang, Dr. Mills, Dr. Sakiyama-Elbert, Dr. Singamaneni, and Dr. Achilefu, for bearing with me during the tumult, and giving insight and being willing to meet at just about any time.

I'd also like to thank the staff of the MSTP and the Biomedical Engineering Department for their wondrous support while completing the process, as well as to the tremendous number of people who have helped me create and excel in both my research and my co-curriculars.

This research would have been impossible without the work of my collaborators, in particular Ramesh Raliya and Nathan Reed of the Biswas Group, Scott Beeman of the Garbow group, Limei Tian and Siri of the Singamaneni Group, and many members of the Optical Radiology lab, including Walter Akers, Kvar Black, Gail Sudlow, Nalini Kotagiri, Rui Tang, Deep Hathi, Sharon Bloch, Denny Shen, Bao Xu, Julie Prior, and Lynne Marsala. It would be impossible without Brenda Phelps, and would be significantly less interesting

without Dolon Maji, LeMoyne Habimana-Griffin, Jessica Miller, Suman Mondal, Tauseef Charanya, Rebecca Gilson, and Annelise Mah.

I would like to also thank the National Cancer Institute, NCI Ruth Kirschstein Fellowship F30 CA189435 and the Medical Scientist Training Program at Washington University for supporting me in this work. This work was supported in part by grants from the US National Institutes of Health (NCI R01 CA171651 and P50 CA094056 and NIBIB R01 EB021048).

Finally, a thank you to Washington University, which has given me an institutional warmth and support I had no idea was possible.

Avik Som

Washington University in St. Louis

May 2018

Dedicated to my family:

Dr. Sukhamoy Som, Sreelata Som, and Avira Som
Kamal Kanti Som, Basanti Som
Prasanna Kumar Mitra, Dipalika Mitra

ABSTRACT OF THE DISSERTATION

Increasing pH in cancer: enabling a new therapeutic paradigm using novel carbonate nanoparticles

by

Avik Som

Doctor of Philosophy in Biomedical Engineering

Washington University in St. Louis, 2018

Professor Samuel Achilefu, Chair

Enormous progress has been made to treat cancer, and yet the mortality rate of cancer remains unacceptably high. High clinical resistance to molecularly targeted therapeutics has pushed interest again towards inhibiting universal biochemical hallmarks of cancer. Recent evidence suggests that malignant tumors acidify the local extracellular environment to activate proteases for degrading the tumor matrix, which facilitates metastasis, and explains why more aggressive tumors are more acidic. Current therapies have only focused on using the low pH for enhancing drug release in tumors, thereby still relying on the traditional paradigm of intracellular inhibition of pathways, a method that continues to have mixed results.

In this dissertation we explore the development of a novel platform that can be made to monitor and modify the critical tumor extracellular environment. The platform enables a shift in the paradigm of current cancer therapy from a predominantly intracellular approach to an extracellular synergistic method of targeting cancer. In the process, we demonstrate the synthesis of a novel type of $CaCO_3$ nanoparticle, its stabilization, the increase of pH in vivo, a mathematical justification and simulation, and the subsequent inhibition of tumor growth and metastasis. By neutralizing the tumor extracellular microenvironment, the platform aims to prevent tumor progression and metastasis as well as minimize the

traditional intracellular based pathways of resistance. Because of the broad universal aspect of low extracellular pH in cancer, particularly in the more malignant tumors, we expect this platform will also have wide applicability, with particular potency on the most aggressive of cancers.

Chapter 1: Introduction

1.1. Cancer Therapy

In spite of the declaration of "War on Cancer" 40 years ago, cancer remains a major public health concern worldwide, causing nearly 1 in 4 deaths in the US alone. [1,2] In 2013, 580,535 cancer deaths are expected in the US. [1] These statistics point to the enormous challenges in winning the "War on Cancer" and indicate the need to rethink treatment paradigms that will improve treatment outcomes.

1.1.1 Molecularly targeted chemotherapeutics:

Cancer is now accepted as a disease caused by genomic instability and epigenetic factors. [3,4] This understanding has ushered in a new set of drugs that target specific molecular pathways used by cancer cells to proliferate and elude the host defense system. Through genomic, proteomic, and metabolomics analyses, several highly successful molecularly targeted therapeutics have been developed such as Dasatinib, which targets tyrosine kinases in chronic myeloid leukemia, and Temsirolimus, which targets the mammalian target of rapamycin (mTOR) found in solid tumors such as renal cell carcinoma.[5,6] However, in spite of embodying the paradigm of most current therapeutic research, targeted therapeutics are rarely used for curative intent. Indeed, most targeted therapeutics require a specific subset of clinical patients to demonstrate efficacy.[7] Given an average development cost of about 1.8 billion dollars per drug, this inefficiency has clinicians turning towards alternatives, such as screening old drugs for off-label use. [8] In addition, due to the redundancy of intracellular pathways, cells are able to mutate around the targeted pathway, developing resistance. Examples include Imatinib (Anti-BCR-ABL) and anti-Her-2 therapies, whose mechanisms of resistance are now active fields of study. [9,10] Given the difficulties we face with molecularly targeted chemotherapeutics, these findings support the need to re-explore the hallmarks of cancer as a universal target for cancer therapy.

1.1.2 Hallmarks of cancer

Cancer is the disease of unrestrained growth and metastasis by cells within the body generally induced by a sequence of genetic mutations that can be clonal (from a single cell origin) or varied. [11] Cancers can effect patients at any point in the life of a human, with increasing propensity with age.[11] Although each cancer is relatively unique, with specifics based on its mutation history, much of the resulting phenotype can be said to be common in various tumors but different from the surrounding normal tissue.[11] This is of strict importance because cancer, unlike many prokaryotic or fungal infectious diseases, also shares a significant component of its antigens with the host. This makes creating both novel compounds and treatments difficult for a curative approach without also eliminating the host patients.

These unique hallmarks among cancers include: increased and limitless mitosis from self sufficiency of growth signals, insensitivity to inhibitory signals, evasion of apoptosis, immune evasion, tissue invasion, and metastasis, hypoxia, extracellular acidity, deregulated cellular energetics and increased angiogenesis.[11,12] Further, the tumor microenvironment, including cancer associated fibroblasts, pericytes, cytokines, and extracellular matrix, play an important role in cancer progression, metastasis and growth. [13] Metabolic hallmarks, such as the deregulation of glycolysis, have resulted in a unique acidic extracellular environment that is both important for tumor prognosis and for differentiating from other tissues.[14] The tumor inflammatory milieu creates a mutagenic environment, and can often induce the existing surroundings to become pro-tumor contributing to immune evasion.[15] Each of these unique hallmarks, because of their commonality, has been targeted by nanomaterial based techniques for both imaging and therapy.

1.1.3 Targeting the hallmarks of cancer for generalized chemotherapy:

Malignant tumors rely on several fundamental pathophysiological processes for survival. Targeting these processes is the favored clinical approach because the agents can be widely used to treat diverse cancer types. Thus, most clinical progress involves therapeutics targeted against DNA replication, microtubules, and glycolysis. However, each of these methods has typically severe side-effects. Anti-mitotic agents, for example, have deleterious effects on any rapidly dividing normal cells, with life threatening implications from bone marrow loss that can lead to immunodeficiency and life threatening infection.[16] With only a few exceptions, these chemotherapies are rarely curative and alternative compensatory metabolic pathways often lead to drug resistance. For example, glycolysis inhibitors are not effective because this conserved metabolic process is replaced by glutamine consumption from muscles, often leading to cachexia.[17,18]

1.2 Extracellular acidic environment is a physiologic hallmark and therapy target of cancer

In the face of these challenges, tumor extracellular acidity has been revisited as a potential target. Models on tumor extracellular pH (pHe) demonstrate a significant relationship between tumor invasiveness and the increased production of acid in most tumors. [19,20] To maintain normal intracellular pH (pHi) and to promote growth by degradation of the extracellular matrix, tumor cells actively transport the excess protons generated during enhanced glycolysis, the Warburg effect, to the extratumoral environment. [21] This leads to a sustained acidic tumor environment, with an average extracellular pH of 6.8, as opposed to the buffered and highly regulated interstitial pH of about 7.4 in the vicinity of healthy tissue.[22] Tumor cells actively use this 4 fold increase in hydrogen ion concentration to degrade the tumor matrix and thus sustain its growth. [20,21] This is possibly due to an increase in matrix metalloproteinase activity at lower pHs. This realization, that low pHe is an indispensable condition for tumor metastasis and malignancy, has increased interest in its potential as a therapeutic target.[23,24]

1.2.1 Recent work on pH sensitive chemotherapeutics:

The acidic environment of cancer is a unique condition that can be targeted to treat diverse tumor types. Groups have tried changing the low pH environment of tumors by either inhibiting carbonic anhydrases or directly neutralizing the tumor acid environment via systemic administration of oral sodium bicarbonate. [23,24] Both of these models have shown efficacy in *in vivo* animal models.[24] However, carbonic anhydrases are important in normal cell physiology and given the vast class of carbonic anhydrases available to tumors in their genetic material, whether the inhibitors can overcome the system's redundancy, such as that seen in anti-glycolytic drugs, remains unknown. The systemic administration of untargeted oral sodium bicarbonate to directly neutralize the acid environment of tumors is not practicable in clinics because of the potentially severe consequences of metabolic alkalosis.[25] In addition, both of these treatments modify pH only temporarily.

1.2.2 Nanomaterials as a potential method for neutralization.

Nanomaterials, and in particular, nanoparticles, have been able to deliver toxins locally that otherwise have systemic side-effects locally to a tumor site. Nanoparticles have been made to be pH sensitive for the delivery of other chemotherapeutics as well. However, nanomaterials have not yet been designed to change proton concentrations themselves *in vivo.* As such they may be a promising technology to enable the practical application of changing pH in tumors *in vivo* as a therapeutic paradigm.

1.3 Nanomaterials as a medically significant tool and technology

Indeed, in the most recent years, nanomaterials in general, have been used for tackling the question of treating cancer. A nanomaterial is defined as a particle or structure, in its broadest form < 1 μm, though generally produced in the range of 10 nm to 500 nm. Nanomaterials can come in a variety of shapes and share a series of interesting properties compared to their macroscopic peers, particularly as it relates to biological systems. The average cell in the body is 10 μm, and has the general capability to ingest nanoparticles < 1μm in size. [26] This has resulted in a series of advantages for classical delivery. Nanomaterials can be made to respond directly to the hallmarks of cancer, such as pH. (Figure 1.1)

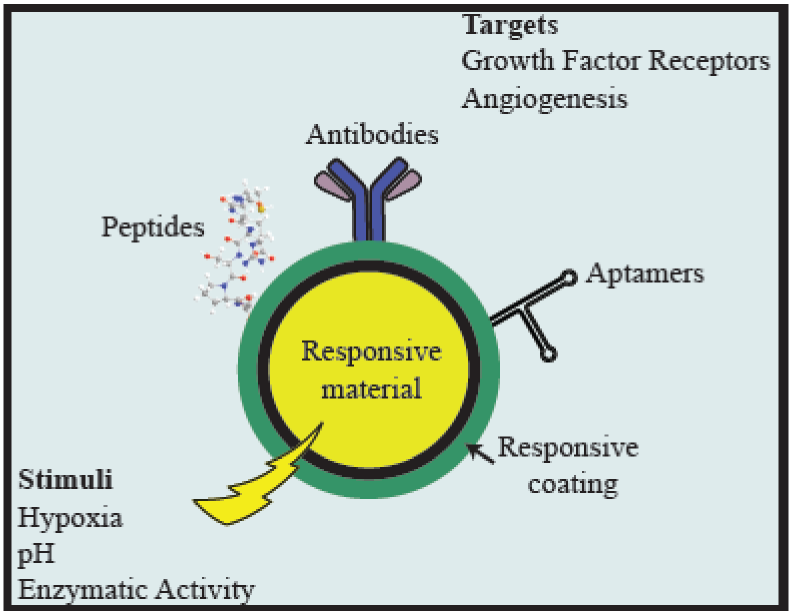

Figure 1.1: Targeting the hallmarks of cancer

Nanomaterials are unique in their ability to respond to particular stimuli and targets. Antibodies, peptides, and aptamers, can all target growth factor receptors, or markers of angiogenesis. Using material and unique properties of nanoparticles, nanomaterials are uniquely capable of responding to stimuli such as hypoxia, pH, and enzymatic activity.

1.3.1 Currently used nanomaterials in medicine

Currently existing nanomaterials have had significant use in material science, paints, and other manufacturing processes. [27,28] In addition, nanomaterials have already been applied for medical applications and reached a level of commercialization, including liposomes for drug delivery, polymeric nanoparticles for blood brain barrier, nanoemulsions and drug solubility enhancers, antibiotics, sunscreen, and quantum dots for imaging, and silica particles for fluorescence. [28] Nanomaterials as such have been primarily used in therapeutic applications, but it is clear that the capability of taking to a commercial medical outlet remains a possibility. Environmental and toxicity concerns also continue to be of interest and study. [27] While most nanomaterials have been used for intracellular delivery and targets, interesting and further trends then for nanomaterials lie in pushing into extracellular environment modulation. Nanomaterials may be a practical method of changing pH.

1.4 Advantages of nanomaterials in medicine

1.4.1 Pharmacokinetics

A significant advantage of nanomaterials refers to its pharmacokinetic properties, both in increasing the duration of effect by agents and reducing the necessary dose. Pharmacokinetics relates to the distribution, spread, and time course of material remaining in the body. Single molecule drugs range in the size range of approximately < 1 nm, and are generally cleared by both glomerular filtration of the kidneys, and liver filtration and removal via bile. As a result of this, free drug concentrations can clear quickly, in < 24 hours. [29,30] Nanoparticles are generally large enough to avoid glomerular filtration, but small enough to leak out into the tumor microenvironment. Addition of stabilizing molecules such as polyethylene glycol or polysaccharides on the nanoparticle surface can dramatically improve blood circulation times and avoidance of the macrophages of the reticuloendothelial system. This property in particular has been heavily used to enhance the half life in blood of a number of otherwise rapidly excreted therapeutics. Examples of this phenomenon include Doxil, the liposome formulation of doxorubicin. [29] In imaging applications, dendrimers nanoparticles have been used to prolong the clearance rate of gadolinium contrast agents. [31] In addition to contrast agents, nanoparticles can be functionalized with drugs and used as vehicles for delivery for diseases such as cancer[32]. In doing so they can alter the pharmacokinetics of drug release, creating more therapeutic potential. Multiple nanoparticle formulations have been used for cancer therapy, including a paclitaxel-loaded poly(lactic-co-glycolic) polymer nanoparticles, doxorubicin-cojugated PLGA nanoparticles, dendrimers with 5-Fluorouracil incorporated, lipid-based anti-neoplastic nanoparticles, and gene-delivering polyethylenimine nanoparticles[33]. Tuning size is thus very important for biodistribution.

1.4.2 Pharmacodynamics

Another advantage is in the pharmacodynamics of nanoparticles. In traditional pharmacodynamics, a free drug is an active drug, while a bound drug is inactive. A nanoparticle can be treated like an effective bound drug. Tuning release from the nanoparticle as a result becomes a potent way to increase therapeutic efficacy at local biological sites while also reducing off-target side-effects. This advantage of nanomaterials has driven a large degree of clinical efficacy by increasing the absolute amount of the underlying drug dose a person can tolerate, such as seen in Doxil, the liposome form of doxorubicin, or in more recent drugs such as in Parkinson's. [34,35]

1.4.3 Surface area to mass ratio

Surface area to mass is related as a function of 1/r, where r is the radius of the material. As a result, nanomaterials have a significantly increased surface area to mass ratio as compared to their macromaterial counterpart. The interface of a particle's surface to its environment is the basis on which a large number of chemical reactions can occur. Per unit mass, increasing the surface area to mass ratio thus greatly enhances the available reactant in the particle to the environment. This phenomenon has been used to create sensitive changes in the nanoparticle when in particular environments such as pH [36,37] , as well as potential enhance binding phenomenon due to multivalency from multiple surface ligands on a single particle.[38] (Figure 1.2)

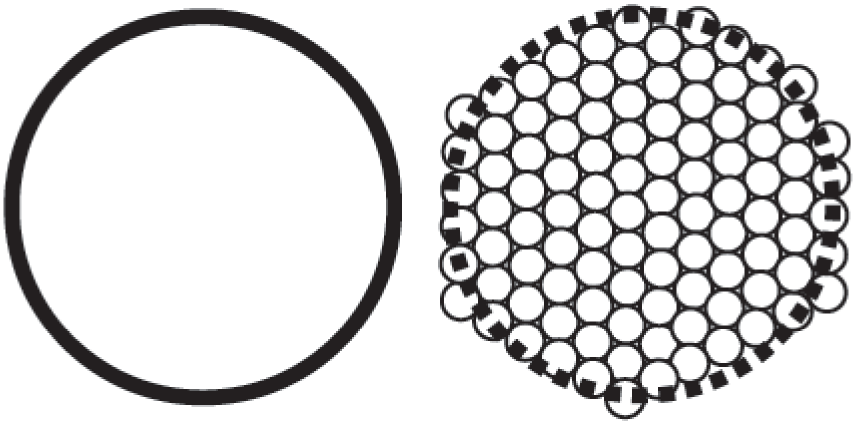

Figure 1.2: Microscopic vs Macroscopic nanomaterials

An important element of nanoparticles compared to its microparticle counterpart is the increased surface area to volume ratio. a) Representation of a microparticle of 1 μm diameter b) Representation of the number of 100 nm diameter particles able to fit in the volume of a 1 µm diameter particle, which is nearly 10x more surface area.

1.4.4 Enhanced Permeation and Retention:

In cancer and inflammation, vessels of the body can become leaky for a variety of reasons, including rapid angiogenesis, as well as a way for immune cells to enter the local area.[29] This has been proven by both casts and surface scanning images demonstrating the gaps.[29] More recently, this permeability has been reported to not be only static, but also have a temporal dynamic nature, with reports of bursts of fluid from the blood into the tumor interstitial area. [39] Further, in cancer, in particular, the growth of cells with a lack of traditional coordination, often means the lack of lymphatics, the body's natural sewage system. As a result, fluid and particles that enter via these leaks, tends to not be cleared as rapidly as they would be in normal tissue. [40] These leaks are size dependent, and have been found to hover around the nanoparticle size range (10-

500 nm) depending on disease or cancer type. This as a result causes a selective increase in the concentration and aggregation of nanoparticles within the area of diseased tissue, allowing a natural targeting due to size. [40] In addition, because of the size, nanoparticles can have increased diffusion capabilities into the tissue as compared to the macromolecular constructs, with smaller particles going farther. The lower limit of size is limited finally by the glomerular apparatus. The upper limit of size is limited by this leakiness of blood vessels. (Figure 1.3)

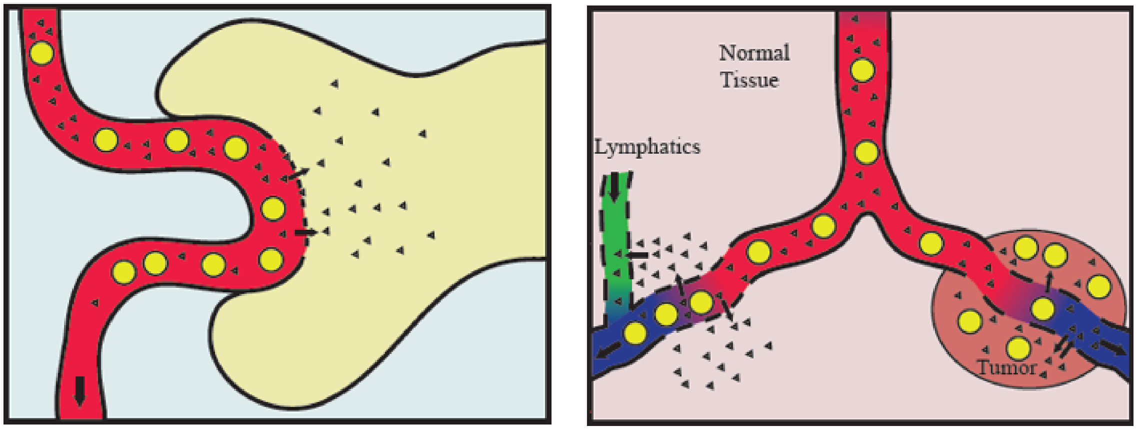

Figure 1.3 Pharmacokinetics: Evading glomerular filtration and tumor retention by enhanced permeation and retention (EPR)

Nanoparticles are unique in how their size affects their *in vivo* performance. a) (Left) Small molecules (triangles) filter easily in the fenestrations seen in the glomerular renal filtration system, whereas larger nanoparticles can avoid this filtration and continue on to the target. b) (Right) Representation of the EPR effect, where, due to their size, nanoparticles selectively penetrate into the tumor region but not into normal tissue. In addition, the lack of lymphatics in the tumor prevents clearance causing increased size-induced retention.

1.5. Capabilities of Nanoparticles

1.5.1 Targeted delivery of compounds

Targeting of nanoparticles can be done both passively, relying on the size effect induced EPR effect, as well as by adding targeting groups, whether antibodies, peptides, or aptamers targeting specific aspects such as angiogenesis, hypoxia, or protein upregulation like folate or EGF. [41-43] These targeting groups can enhance the percentage of nanoparticles in an area, and are valuable directors in inducing cellular uptake and directing cellular delivery. [38,44]

1.5.2 Sensing the environment- nano tuning delivery

A consequence of the increased surface area to mass ratio is an increased ability to sense environments. This allows an increased reaction rate at the surface for a variety of chemical reactions including protonation, hydration, protease degradation, or a change in charge of the particle. This change effectively signals a difference externally whether for the delivery of a drug, or for imaging purposes. [45-48] Examples include pH sensitivity by nanoparticles to the acidity in the tumor microenvironment, (approximately a pH of 6.5) for therapy. [37,49-52] Nanoparticles have not yet been used to modify this environment.

1.5.3 Entering and modifying the intracellular compartment

The intracellular compartment is composed of both the cytosol and a variety of organelles. By and large, nanoparticles enter the cell via a lysosomal pathway, with a variety of specific endocytosis mechanisms. The lysosome itself has a low pH (about 5), as compared to a cytosolic pH have 7.2. Multiple nanoparticles have thus been developed to escape the lysosome, using the proton sponge effect, an effect of using poly-amines and bases to break the barrier by osmotic lysis. [53-57] Other groups have used methods such as viruses to deliver cargo to the cytosol, external stimuli to break the lysosomal membrane for delivery, and even others rely on passive diffusion across membranes post release in the extracellular environments, such as hydrophobic chemotherapies or proton channels that already exist. [58-60] All of these methods deliver components that end up changing the intracellular compartment in either composition, or more commonly delivering to change gene products (miRNA or siRNA) themselves. [53,61,62]

1.5.4 Quenching and Imaging

Nanoparticles, for imaging, can also serve as a quenching sink, a consequence of being able to deliver and generate an easy area for binding. This phenomenon has been heavily used for gold in particular, as well as other nanoparticle bases.[63-68] In addition, nanoparticles are capable of triggered release and as a result do well as a prodrugs and activatable imaging agents. [36,37,69-71]

1.5.5 Modifying the extracellular compartment

The extracellular environment has become of increasing interest because of its importance in tumor growth and metastasis. Trying to target and change this area howevser has only recently become of recent interest. The question remains whether the advantages held by nanoparticles can be used to enable a new therapeutic paradigm involving increasing the local pH of tumors *in vivo*.

1.6 Aims of the dissertation.

Given this context, the goal of this dissertation was to explore the effects of pH on tumor growth through the development of a novel pH neutralizing nanoparticle. Accordingly, we investigated the following hypotheses.

Chapter 2: The acidic extracellular pH of tumors has a downstream effect on surrounding stromal fibroblasts.

Chapter 3: The mathematical simulation of $CaCO_3$ *in vivo* will predict the ability to change pH selectively *in vivo*

Chapter 4: $CaCO_3$ can be synthesized as a nanoparticle

Chapter 5: $CaCO_3$ nanoparticles have minimal toxicity and have a systemic biodistribution that reaches the tumor

Chapter 6: Systemic administration of $CaCO_3$ nanoparticles can increase pH in vivo and inhibit tumor growth and metastasis.

1.6. Copyright Acknowledgment

Portions of this chapter including figures were included with permission from the below manuscripts or writings.

“A Novel Extracellular and Intracellular Treatment Paradigm for Eradicating Cancer”, National Institute of Health, National Cancer Institute, Ruth S. Kirchstein Fellowship, F30CA189435-02, 2013

Avik Som, Kvar Black, LeMoyne Habimana-Griffin, Samuel Achilefu, “Nanomaterials for imaging and medical therapy”, WIREs Overview, To be submitted 2016**.**

1.7 References

1 Siegel, R., Naishadham, D. & Jemal, A. Cancer statistics, 2013. *CA Cancer J Clin* **63**, 11-30, doi:10.3322/caac.21166 (2013).

2 Vincent DeVita, S. S., Anne Barker. (National Cancer Institute).

3 Christoph Lengauer, K. W. K., and Bert Vogelstein. Genetic instability in human cancers. *Nature* **396**, 643-649 (1998).

4 Jones, P. A. & Baylin, S. B. The fundamental role of epigenetic events in cancer. *Nat Rev Genet* **3**, 415-428, doi:10.1038/nrg816 (2002).

5 Copland, M. *et al.* Dasatinib (BMS-354825) targets an earlier progenitor population than imatinib in primary CML but does not eliminate the quiescent fraction. *Blood* **107**, 4532-4539, doi:10.1182/blood-2005-07-2947 (2006).

6 Stenner-Liewen, F., Grunwald, V., Greil, R. & Porta, C. The clinical potential of temsirolimus in second or later lines of treatment for metastatic renal cell carcinoma. *Expert Rev Anticancer Ther*, doi:10.1586/14737140.2013.833684 (2013).

7 Druker, B. J. Imatinib: Paradigm or Anomaly? . *Cell Cycle* **3**, 833-835 (2004).

8 Gupta, S. C., Sung, B., Prasad, S., Webb, L. J. & Aggarwal, B. B. Cancer drug discovery by repurposing: teaching new tricks to old dogs. *Trends Pharmacol Sci* **34**, 508-517, doi:10.1016/j.tips.2013.06.005 (2013).

9 Daley, G. Q. Gleevec Resistance. *Cell Cycle* **2**, 190-191 (2003).

10 Nahta, R., Yu, D., Hung, M. C., Hortobagyi, G. N. & Esteva, F. J. Mechanisms of disease: understanding resistance to HER2-targeted therapy in human breast cancer. *Nat Clin Pract Oncol* **3**, 269-280, doi:10.1038/ncponc0509 (2006).

11 Hanahan, D. & Weinberg, R. A. Hallmarks of cancer: the next generation. *Cell* **144**, 646-674, doi:10.1016/j.cell.2011.02.013 (2011).

12 Ryan, B. M. & Faupel-Badger, J. M. The hallmarks of premalignant conditions: a molecular basis for cancer prevention. *Seminars in oncology* **43**, 22-35, doi:10.1053/j.seminoncol.2015.09.007 (2016).

13 Pietras, K. & Ostman, A. Hallmarks of cancer: interactions with the tumor stroma. *Exp Cell Res* **316**, 1324-1331, doi:10.1016/j.yexcr.2010.02.045 (2010).

14 Pavlova, N. N. & Thompson, C. B. The Emerging Hallmarks of Cancer Metabolism. *Cell metabolism* **23**, 27-47, doi:10.1016/j.cmet.2015.12.006 (2016).

15 Hagerling, C., Casbon, A. J. & Werb, Z. Balancing the innate immune system in tumor development. *Trends in cell biology* **25**, 214-220, doi:10.1016/j.tcb.2014.11.001 (2015).

16 Lena E. Friberg, A. H., Hugo Maas, Laurent Nguyen, Mats O. Karlsson. Model of Chemotherapy-Induced Myelosuppression with Parameter Consistency across Drugs. *J Clin Oncol* **20**, 4713-4721 (2002).

17 Tennant, D. A., Duran, R. V. & Gottlieb, E. Targeting metabolic transformation for cancer therapy. *Nature reviews. Cancer* **10**, 267-277, doi:10.1038/nrc2817 (2010).

18 Efstathiou, E. & Logothetis, C. J. A new therapy paradigm for prostate cancer founded on clinical observations. *Clin Cancer Res* **16**, 1100-1107, doi:10.1158/1078-0432.CCR-09-1215 (2010).

19 Robert A Gatenby, E. T. G. A Reaction-Diffusion Model of Cancer Invasion. *Cancer Res* **56**, 5745-5753. (1996).

20 Gatenby, R. A., Gawlinski, E. T., Gmitro, A. F., Kaylor, B. & Gillies, R. J. Acid-mediated tumor invasion: a multidisciplinary study. *Cancer Res* **66**, 5216-5223, doi:10.1158/0008-5472.CAN-05-4193 (2006).

21 Marion Stubbs, P. M. J. M., John R. Griffiths, and C. Lidsay Bashford Causes and Consequences of tumour acidity and implications for treatment. *Molecular Medicine Today* **6**, 15-19 (2000).

22 Agatha S. E. Ojugo *et al.* Measurement of extracellular pH of solid tumors in mice by MR Spectroscopy. Comparison of exogenous 19F and 31 P probes. *NMR in Biomedicine* **12**, 495-504 (1999).

23 Lou, Y. *et al.* Targeting tumor hypoxia: suppression of breast tumor growth and metastasis by novel carbonic anhydrase IX inhibitors. *Cancer Res* **71**, 3364-3376, doi:10.1158/0008-5472.CAN-10-4261 (2011).

24 Robey, I. F. & Nesbit, L. A. Investigating mechanisms of alkalinization for reducing primary breast tumor invasion. *Biomed Res Int* **2013**, 485196, doi:10.1155/2013/485196 (2013).

25 Martin, N. K. *et al.* Predicting the safety and efficacy of buffer therapy to raise tumour pHe: an integrative modelling study. *Br J Cancer* **106**, 1280-1287, doi:10.1038/bjc.2012.58 (2012).

26 Rosenblum, L. T., Kosaka, N., Mitsunaga, M., Choyke, P. L. & Kobayashi, H. In vivo molecular imaging using nanomaterials: general in vivo characteristics of nano-sized reagents and applications for cancer diagnosis. *Molecular membrane biology* **27**, 274-285, doi:10.3109/09687688.2010.481640 (2010).

27 Aitken, R. J., Chaudhry, M. Q., Boxall, A. B. & Hull, M. Manufacture and use of nanomaterials: current status in the UK and global trends. *Occupational medicine* **56**, 300-306, doi:10.1093/occmed/kql051 (2006).

28 Salata, O. Applications of nanoparticles in biology and medicine. *Journal of Nanobiotechnology* **2** (2004).

29 Wong, A. D., Ye, M., Ulmschneider, M. B. & Searson, P. C. Quantitative Analysis of the Enhanced Permeation and Retention (EPR) Effect. *PloS one* **10**, e0123461, doi:10.1371/journal.pone.0123461 (2015).

30 Choi, H. S. *et al.* Renal clearance of quantum dots. *Nat Biotechnol* **25**, 1165-1170, doi:10.1038/nbt1340 (2007).

31 Aaron Joseph L. Villaraza, A. B., and Martin W. Brechbiel. Macromolecules, Dendrimers, and Nanomaterials in Magnetic Resonance Imaging: The Interplay between Size, Function, and Pharmacokinetics. *Chemical reviews* **110**, 2921–2959 (2010).

32 Brigger, I., Dubernet, C. & Couvreur, P. Nanoparticles in cancer therapy and diagnosis. *Adv Drug Deliv Rev* **64**, 24-36 (2012).

33 Brannon-Peppas, L. & Blanchette, J. Nanoparticle and targeted systems for cancer therapy. *Adv Drug Deliv Rev* **64** (2012).

34 Wen, Z. *et al.* Odorranalectin-conjugated nanoparticles: preparation, brain delivery and pharmacodynamic study on Parkinson's disease following intranasal administration. *Journal of controlled release : official journal of the Controlled Release Society* **151**, 131-138, doi:10.1016/j.jconrel.2011.02.022 (2011).

35 Gabizon, A. A. Pegylated Liposomal Doxorubicin: Metamorphosis of an Old Drug into a New Form of Chemotherapy. *Cancer Investigation* **19**, 424-436, doi:10.1081/cnv-100103136 (2001).

36 Fan, L. *et al.* Novel super pH-sensitive nanoparticles responsive to tumor extracellular pH. *Carbohydrate Polymers* **73**, 390-400, doi:10.1016/j.carbpol.2007.12.006 (2008).

37 Wang, C. *et al.* Imaging-Guided pH-Sensitive Photodynamic Therapy Using Charge Reversible Upconversion Nanoparticles under Near-Infrared Light. *Advanced Functional Materials* **23**, 3077-3086, doi:10.1002/adfm.201202992 (2013).

38 Hong, S. *et al.* The binding avidity of a nanoparticle-based multivalent targeted drug delivery platform. *Chemistry & biology* **14**, 107-115, doi:10.1016/j.chembiol.2006.11.015 (2007).

39 Matsumoto, Y. *et al.* Vascular bursts enhance permeability of tumour blood vessels and improve nanoparticle delivery. *Nature nanotechnology*, doi:10.1038/nnano.2015.342 (2016).

40 Barreto, J. A. *et al.* Nanomaterials: applications in cancer imaging and therapy. *Advanced materials* **23**, H18-40, doi:10.1002/adma.201100140 (2011).

41 Farokhzad, O. C. *et al.* Targeted nanoparticle-aptamer bioconjugates for cancer chemotherapy in vivo. *Proceedings of the National Academy of Sciences of the United States of America* **103**, 6315-6320, doi:10.1073/pnas.0601755103 (2006).

42 Chariou, P. L. *et al.* Detection and imaging of aggressive cancer cells using an epidermal growth factor receptor (EGFR)-targeted filamentous plant virus-based nanoparticle. *Bioconjugate chemistry* **26**, 262-269, doi:10.1021/bc500545z (2015).

43 Brannon-Peppas, L. & Blanchette, J. O. Nanoparticle and targeted systems for cancer therapy. *Advanced drug delivery reviews* **56**, 1649-1659, doi:10.1016/j.addr.2004.02.014 (2004).

44 Kocbek, P., Obermajer, N., Cegnar, M., Kos, J. & Kristl, J. Targeting cancer cells using PLGA nanoparticles surface modified with monoclonal antibody. *Journal of controlled release : official journal of the Controlled Release Society* **120**, 18-26, doi:10.1016/j.jconrel.2007.03.012 (2007).

45 Blum, A. P. *et al.* Stimuli-responsive nanomaterials for biomedical applications. *Journal of the American Chemical Society* **137**, 2140-2154, doi:10.1021/ja510147n (2015).

46 Habibi, N., Kamaly, N., Memic, A. & Shafiee, H. Self-assembled peptide-based nanostructures: Smart nanomaterials toward targeted drug delivery. *Nano today*, doi:10.1016/j.nantod.2016.02.004 (2016).

47 Ling, D. *et al.* Multifunctional tumor pH-sensitive self-assembled nanoparticles for bimodal imaging and treatment of resistant heterogeneous tumors. *Journal of the American Chemical Society* **136**, 5647-5655, doi:10.1021/ja4108287 (2014).

48 Zhu, L. & Torchilin, V. P. Stimulus-responsive nanopreparations for tumor targeting. *Integrative biology : quantitative biosciences from nano to macro* **5**, 96-107, doi:10.1039/c2ib20135f (2013).

49 Tian, J. *et al.* Cell-specific and pH-activatable rubyrin-loaded nanoparticles for highly selective near-infrared photodynamic therapy against cancer. *Journal of the American Chemical Society* **135**, 18850-18858, doi:10.1021/ja408286k (2013).

50 Chen, L. Q. *et al.* Evaluations of extracellular pH within in vivo tumors using acidoCEST MRI. *Magnetic resonance in medicine* **72**, 1408-1417, doi:10.1002/mrm.25053 (2014).

51 Catalano, V. *et al.* Tumor and its microenvironment: a synergistic interplay. *Semin Cancer Biol* **23**, 522-532, doi:10.1016/j.semcancer.2013.08.007 (2013).

52 Estrella, V. *et al.* Acidity generated by the tumor microenvironment drives local invasion. *Cancer Res* **73**, 1524-1535, doi:10.1158/0008-5472.CAN-12-2796 (2013).

53 Deng, X. *et al.* Acidic pH-induced charge-reversal nanoparticles for accelerated endosomal escape and enhanced microRNA modulation in cancer cells. *Chemical communications* **52**, 3243-3246, doi:10.1039/c5cc10396g (2016).

54 Sourav Prasanna Mukherjeea, F. M. L., Hugh J. Byrneb. Mechanistic studies of in vitro cytotoxicity of PAMAM dendrimers in mammalian cells. *NSTI-Nanotech* **3**, 171-174 (2011).

55 Gaelle Creusat, A.-S. R., Etienne Weiss, Rkia Elbaghdadi, Jean-Serge Remy, Rita Mulherkar. and Guy Zuber. Proton Sponge Trick for pH-Sensitive Disassembly of Polyethylenimine-Based siRNA Delivery Systems. *Bioconjugate chemistry* **21,**, 994–1002 (2010,).

56 Yang, S. & May, S. Release of cationic polymer-DNA complexes from the endosome: A theoretical investigation of the proton sponge hypothesis. *J Chem Phys* **129**, 185105, doi:10.1063/1.3009263 (2008).

57 Akinc, A., Thomas, M., Klibanov, A. M. & Langer, R. Exploring polyethylenimine-mediated DNA transfection and the proton sponge hypothesis. *J Gene Med* **7**, 657-663, doi:10.1002/jgm.696 (2005).

58 Wang, H. *et al.* A Near-Infrared Laser-Activated "Nanobomb" for Breaking the Barriers to MicroRNA Delivery. *Advanced materials* **28**, 347-355, doi:10.1002/adma.201504263 (2016).

59 Chakravarty, P., Lane, C. D., Orlando, T. M. & Prausnitz, M. R. Parameters affecting intracellular delivery of molecules using laser-activated carbon nanoparticles. *Nanomedicine : nanotechnology, biology, and medicine*, doi:10.1016/j.nano.2015.12.380 (2016).

60 Choi, J. W. *et al.* pH-sensitive oncolytic adenovirus hybrid targeting acidic tumor microenvironment and angiogenesis. *Journal of controlled release : official journal of the Controlled Release Society* **205**, 134-143, doi:10.1016/j.jconrel.2015.01.005 (2015).

61 Bakker, M. H., Lee, C. C., Meijer, E. W., Dankers, P. Y. & Albertazzi, L. Multicomponent Supramolecular Polymers as a Modular Platform for Intracellular Delivery. *ACS nano* **10**, 1845-1852, doi:10.1021/acsnano.5b05383 (2016).

62 Khaled, S. Z. *et al.* One-pot synthesis of pH-responsive hybrid nanogel particles for the intracellular delivery of small interfering RNA. *Biomaterials* **87**, 57-68, doi:10.1016/j.biomaterials.2016.01.052 (2016).

63 Xu, J., Yu, H., Hu, Y., Chen, M. & Shao, S. A gold nanoparticle-based fluorescence sensor for high sensitive and selective detection of thiols in living cells. *Biosensors & bioelectronics* **75**, 1-7, doi:10.1016/j.bios.2015.08.007 (2016).

64 Chinen, A. B. *et al.* Nanoparticle Probes for the Detection of Cancer Biomarkers, Cells, and Tissues by Fluorescence. *Chemical reviews* **115**, 10530-10574, doi:10.1021/acs.chemrev.5b00321 (2015).

65 Achilefu, S. *et al.* Near infrared fluorescence quenching properties of copper (II) ions for potential applications in biological imaging. **8956**, 89560K, doi:10.1117/12.2053746 (2014).

66 Dulkeith, E. *et al.* Fluorescence quenching of dye molecules near gold nanoparticles: radiative and nonradiative effects. *Physical review letters* **89**, 203002, doi:10.1103/PhysRevLett.89.203002 (2002).

67 E. Dulkeith, M. R., T. A. Klar, and J. Feldmann. Gold Nanoparticles Quench Fluorescence by Phase Induced Radiative Rate Suppression. **5**, 585-589 (2005).

68 Tansi, F. L. *et al.* Fluorescence-quenching of a liposomal-encapsulated near-infrared fluorophore as a tool for in vivo optical imaging. *Journal of visualized experiments : JoVE*, e52136, doi:10.3791/52136 (2015).

69 Chen, C. *et al.* Stimuli-responsive controlled-release system using quadruplex DNA-capped silica nanocontainers. *Nucleic Acids Res* **39**, 1638-1644, doi:10.1093/nar/gkq893 (2011).

70 Chen, J.-F., Ding, H.-M., Wang, J.-X. & Shao, L. Preparation and characterization of porous hollow silica nanoparticles for drug delivery application. *Biomaterials* **25**, 723-727, doi:10.1016/s0142-9612(03)00566-0 (2004).

71 Du, J. Z., Mao, C. Q., Yuan, Y. Y., Yang, X. Z. & Wang, J. Tumor extracellular acidity-activated nanoparticles as drug delivery systems for enhanced cancer therapy. *Biotechnol Adv*, doi:10.1016/j.biotechadv.2013.08.002 (2013).

72 Som, A. *et al.* Monodispersed calcium carbonate nanoparticles modulate local extracellular pH and inhibit tumor growth in vivo *Nanoscale* (2015).

Chapter 2: Effect of pH on the extracellular environment and surrounding stromal cells

Chapter Summary

We explored the effect of the acidic microenvironment on surrounding stromal cells. Octamer-binding transcription factor 4 (OCT-4) is an important marker of cellular de-differentiation that can be induced by environmental stressors, such as acidity. Here we demonstrate that chronic acidic stress in solid tumors induced OCT-4 expression in fibroblasts and other stromal cells in four tumor models. The results have implications for how tumors utilize pH modulation to recruit associated stromal cells, induce partial reprogramming of tumor-associated stromal cells, and respond to therapy. It demonstrates the importance of acidity on tumor growth.

2.1 Introduction

Tumor-stromal interactions play important roles in tumor growth and metastasis with direct impact on extracellular matrix enzymes, cytokines, matrix polymers such as collagen and hyaluronic acid derivatives, hypoxia, and pH. [1-5] Previous studies have shown that stromal cells, such as cancer-associated fibroblasts and perivascular cells, participate in tumor metastasis and growth. [6,7] A vexing question is how tumors recruit and alter stromal cells, including fibroblasts, from normal tissue during cancer growth and metastasis. [8-10]

The cancer microenvironment replicates in many ways the characteristics of normal stem cell environments.[11-13] Several factors, such as hypoxia and the acidic environment found in the cancer stem cell niche, are also stressors on cell metabolism and division.[11,14] Literature suggests that these same stressors can induce at least a partial reprogramming of fibroblast cells in vitro, resulting in the expression of OCT-4 in culture under conditions of metabolic stress. [15] Both in vivo and in vitro studies have shown that OCT-4 mediates cellular development. Given that the in vivo microenvironment of many solid tumors is weakly acidic (pH 6.5)[16-19], we hypothesized that acid-mediated chronic mild stress would induce a partial reprogramming of stromal cells in vivo, as indicated by increased OCT-4 expression. Our results show that in vitro replication of the chronic mildly acidic solid tumor environment induced OCT-4 expression in murine fibroblasts. We also demonstrated that OCT-4 expression increased in fibroblasts and other supporting stromal cells within tumor xenografts. This expression of OCT-4 may explain some of the stem cell-like phenotypes of stromal cells within the tumor microenvironment.

2.2 Methods

2.2.1 Statement on Ethics

All animal experiments were conducted in accordance with the approved guidelines for the care and use of laboratory animals in research, and the protocol was approved by the Washington University Animal Welfare Committee.

2.2.2 Immunofluorescent staining

Cells or tissues were stained per the manufacturer's protocol using rabbit polyclonal (ab19857, Abcam, Cambridge, MA; 1:200 dilution) or murine anti-OCT-4 (ab91194, Abcam, Cambridge, MA; 1:200 dilution), and rat anti-Vimentin (ab115189, Abcam, Cambridge, MA; 1:200 dilution). Secondary antibodies were Allophycocyanin anti-mouse IgG (A-865, Life Technologies, Grand Island, NY; 1:1000), AlexaFluor 555 anti-rabbit IgG, and anti-Rat IgG AlexaFluor 647 (Abcam, Cambridge, MA; 1:1000 dilution). Cells were visualized with an Olympus FV1000 Confocal Microscope using 488 nm, 543 nm, or 633 nm for excitation. Tissue was visualized with an Olympus BX51 upright epifluorescence microscope (Olympus America, Center Valley, PA) using excitation/emission filters of 480 nm / 535 nm, and 620 nm / 700 nm.

2.2.3 Tumor model growth

BxPC-3, MDA-MB-231, and EMT-6 cells were injected subcutaneously into the dorsal flanks of athymic nude mice, while 4T1luc cells were injected into Balb/c mice. Mice were sacrificed when the tumors were between 0.5 and 1.5 cm in diameter. In certain cases, tumors may have had exposure to the near-infrared tumor imaging agent cypate prior to excision. Tumors were excised based on gross appearance and frozen in OCT media. The average pH in 4T1 tumor models was 6.8 +/- 0.1 pH units, as measured by an invasive probe (5 mm probe). The average pH level in EMT-6 and BxPC-3 tumors was not measured, previous studies reported acidity in BxPC-3 and EMT-6 tumor models and the importance of the pH for chemotherapy resistance.[19] Tissue sections were cryosectioned at 10 μm thickness. Tissue was visualized with an Olympus BX51 upright epifluorescence microscope (Olympus America, Center Valley, PA) using excitation/emission filters of 480 nm / 535 nm, and 620 nm / 700 nm.

2.2.4 Cell culture

MDA-MB 231, 4T1luc, and BxPC-3 tumor cells, and 3T3-GFP fibroblasts were cultured alone or in co-culture in acidic (pH 6.5), slightly acidic (pH 6.8), or non-acidic (pH 7.4) media (DMEM + 10% FBS + 1% Pen Strep) in 8 well slides. Acidic media was created by titrating DMEM + 10% FBS + 1% Pen Strep media with 1 M HCl to the desired pH range. Slides were incubated for 7 days without any modifications in 5% CO2 at 37^{o}C, after which they were stained for OCT-4. A summary of techniques can be found in Figure 2.1.

2.2.5 Longitudinal study

Cells were cultured as described above in normal media overnight and then switched to acidic conditions at day 0, 1, 3, and 5 and incubated until day 7 prior to immunostaining.

2.2.6 3T3 Fibroblast growth in nude mice

3T3-GFP Fibroblast cells were grown in T75 flasks under either HCl titrated, pH 6.5 conditions, as described above, or in pH 7.4 media for 7 days, or grown in T75 flasks under normal conditions overnight. Cells were trypsinized and injected in a 50% matrigel/PBS matrix. For each "tumor" injection site, 1 million cells from the above three categories were used. Mouse 1 received the acid treated cells on its left flank and 7 day pH 7.4 treated cells in its right flank. Mouse 2 received the acid treated cells on its left flank and 1 day pH 7.4 treated cells in its right flank. Mouse 3 received 7 day control cells on its left flank and 1 day pH 7.4 treated cells in its right flank. GFP images were taken 2 weeks later using the ART Optix MX3 system.

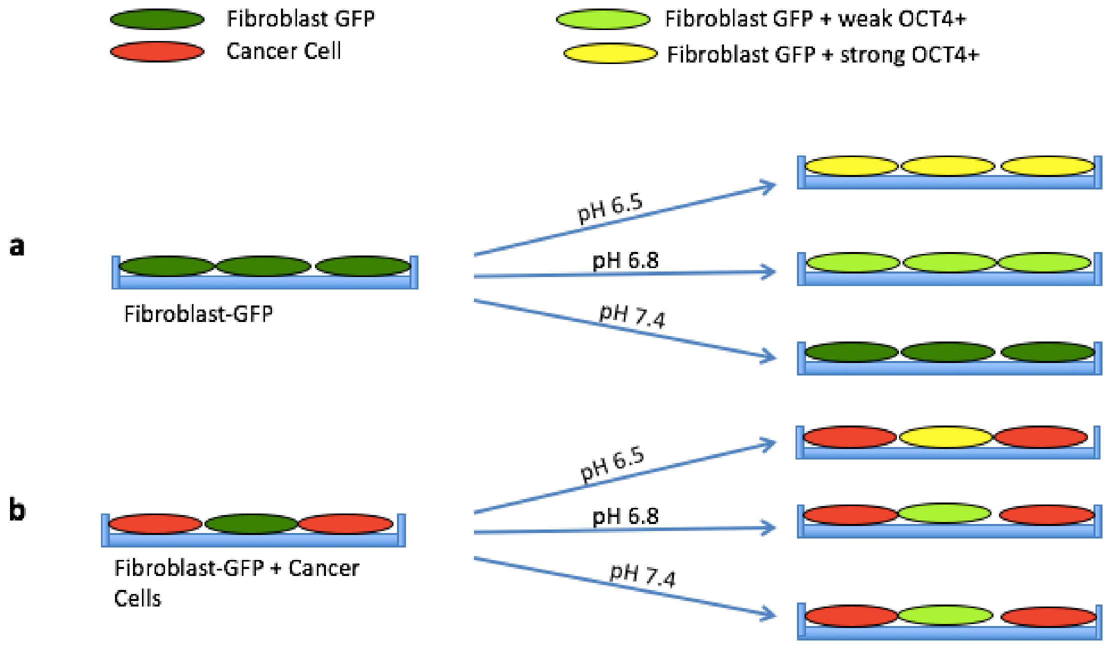

Figure 2.1: Methodology/Summary for OCT-4 induction *in vitro*. Describes the methods section schematically. **(a)** 3T3-GFP$^+$ can be treated with pH 6.5 treated medium leading to the strongest OCT-4 expression, with reduced expression going towards 7.4. **(b)** 3T3-GFP$^+$ can be co-cultured with a tumor cell line and induce the same effect with the strongest OCT-4 expression at pH 6.5.

2.3 Results

2.3.1 Exposure of cells to acidic environment induces OCT-4 expression in vitro

We used four tumor cell lines for this study: (1) the human breast cancer cell line MDA-MB-231 is OCT-4 positive and expresses the OCT-4 inducing leukemia inhibitory factor, LiF[20]; (2) the murine mammary carcinoma EMT-6 undergoes epithelial-mesenchymal transition; (3) the human pancreatic adenocarcinoma BxPC-3 has not, to our knowledge, been shown to express OCT-4 ; and (4) the murine breast cancer model 4T1luc is an aggressive tumor model with significant drug resistance. We first determined if the tumor cells could induce OCT-4 expression in nontumor cells under normal physiologic pH. Using BxPc-3 and MDA-MB-231 cells, we cultured GFP transfected 3T3 fibroblast cells (non-tumor cells) in pH 7.4 media for 7 days in the presence or absence of tumor cells. In the absence of cancer cells, OCT-4 expression in the 3T3 cells did not increase over time (Figure 2.2a). In contrast, co-culture of these fibroblasts with tumor cells at pH 7.4 resulted in increased OCT-4 expression (Figure 2.2 b, c). The enhanced nuclear localization of OCT-4 indicates that tumor cells can facilitate OCT-4 expression in surrounding healthy tissue under normal physiological pH.

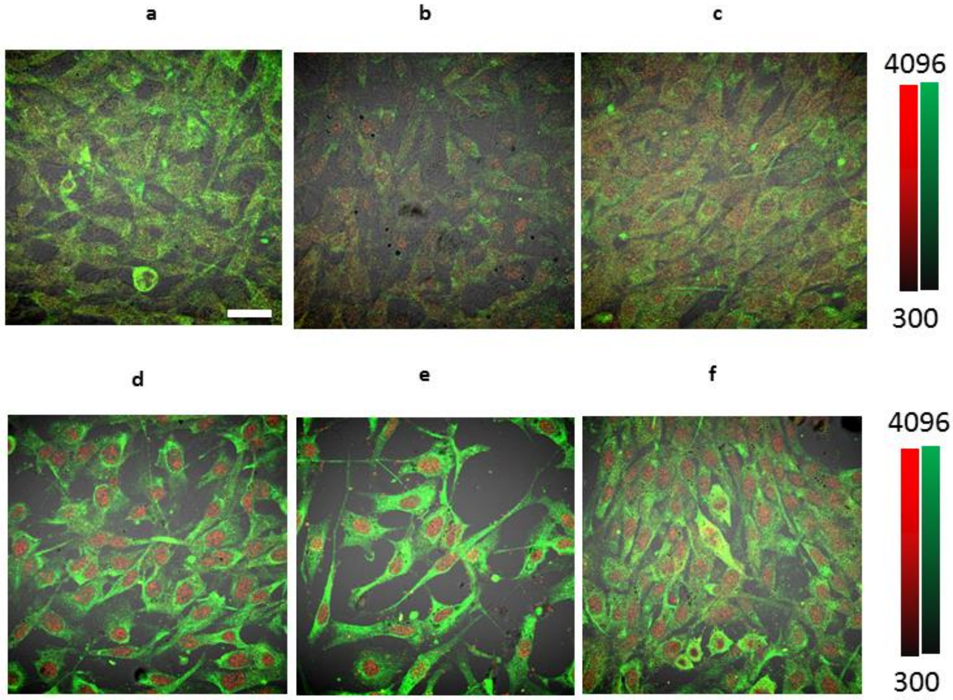

Figure 2.2: Simulation of tumor-associated pH environment *in vitro*. Confocal imaging of rabbit polyclonal anti-OCT4 (red) staining and anti-vimentin (green) in 3T3 cells under various conditions. Fibroblasts **(a)** incubated in pH 7.4 media, **(b)** co-cultured with MDA-MB-231 cells in pH 7.4 media, **(c)** co-cultured with BXPC-3 in pH 7.4 media, **(d)** incubated in pH 6.5 media, **(e)** co-cultured with MDA-MB-231 cells in pH 6.5 media, **(f)** co-cultured with BXPC-3 breast cancer cells in pH 6.5 media. All the cells were incubated for 7 days with no changes in media. Magnification is 20x. Scale bar is 100 μm.

A previous study showed that cells cultured in a highly acidic environment (pH 5) showed increased OCT-4 expression.[15] Because the extracellular pH of solid tumors rarely falls below pH 6, we investigated whether OCT-4 expression could be induced in cells cultured in a more physiologically relevant, mildly acidic medium (pH 6.5), similar to the extracellular pH of solid tumors. GFP transfected 3T3 fibroblast cells were cultured in acidic (pH 6.5) media for 7 days in the presence or absence of tumor cells. A high level and intense nuclear localization of OCT-4 expression was observed in both the presence and absence of tumor cells (Figure 2.2 d-f), suggesting the possibility of cell reprogramming under these conditions. Co-staining with vimentin shows strong cytoplasmic vimentin positivity confirming the fibroblast origin of the cells (Figure 2.2). The percentage of OCT-4 positive cells sequentially increased over time (Figure 2.3), indicating that chronic exposure of these cells to acidic environments such as those found in some solid tumors, provides a potential pathway to induce cellular stress to surrounding healthy cells. In addition, there is an inverse correlation of OCT-4 expression with acidity, OCT-4 intensity increasing as pH decreases from 7.4 to 6.5 (Figure 2.4). Very few BxPC-3 and MDA-MB-231 (GFP-negative) cells were observed because these cells do not remain adherent during staining. Similar results were obtained when cells were stained using a second OCT-4 antibody (Figure 2.5). Incubation with non-tumor cell lines, such as primary mammary epithelial cells (PMEC), under acidic conditions showed OCT-4 expression in both cell lines, while no OCT-4 expression was seen under non-acidic conditions. (Figure 2.6)

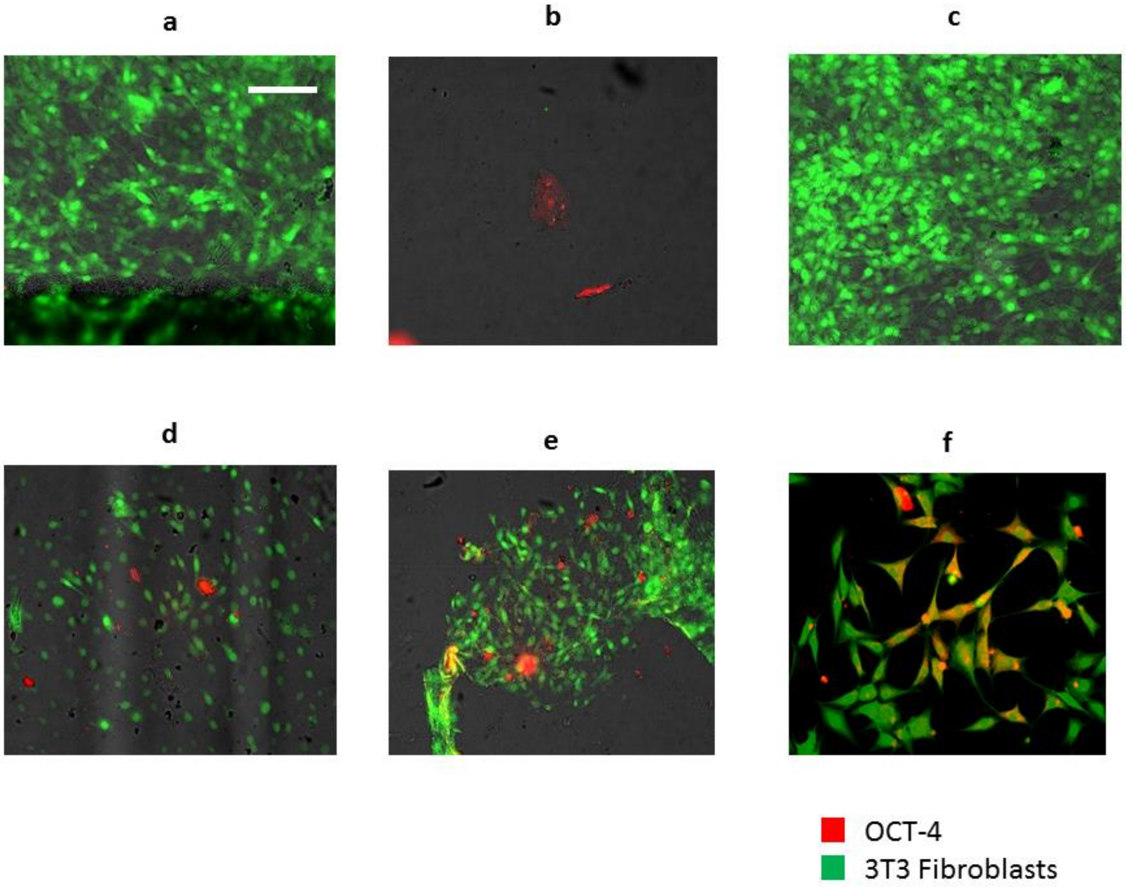

Figure 2.3: Time course of OCT-4 expression. **(a)** OCT-4 expression of GFP$^+$ fibroblasts cultured for 7 days in normal pH 7.4 media. **(b)** OCT-4 expression MDA-MB-231 cells, positive control. **(c)** OCT-4 expression of GFP$^+$ fibroblasts cultured for 6 days in normal pH 7.4 media and 1 day in pH 6.5 media. **(d)** OCT-4 expression of GFP$^+$ fibroblasts cultured for 4 days in normal pH 7.4 media and 3 day in pH 6.5 media. **(e)** OCT-4 expression of GFP$^+$ fibroblasts cultured for 2 days in normal pH 7.4 media and 5 day in pH 6.5 media. **(f)** OCT-4 expression of GFP$^+$ fibroblasts cultured for 7 days in pH 6.5 media. Red represents OCT-4$^+$ cells, and green represents GFP+ fibroblasts. Scale bar represents 100 μm.

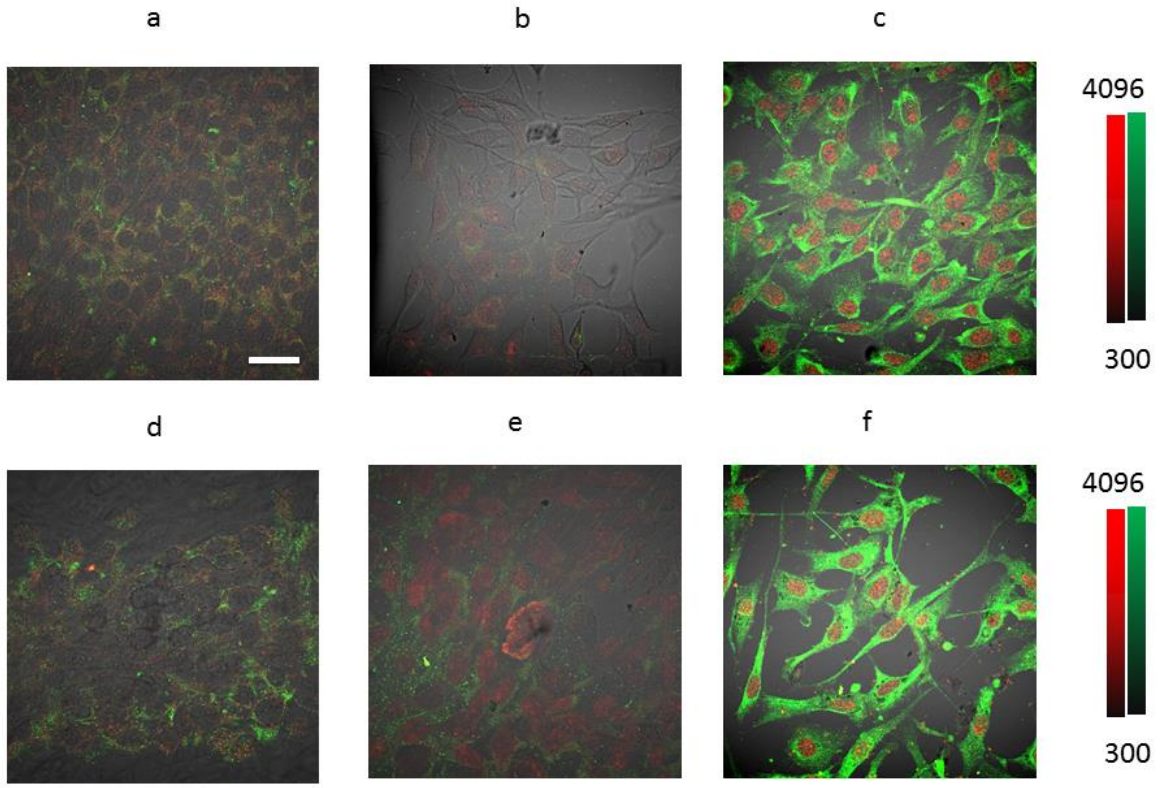

Figure 2.4: Effect of pH gradient on OCT-4 expression in 3T3 fibroblast cells. (a) Fibroblasts incubated in media (pH 7.4) for 7 days with no changes in media **(b)** Fibroblasts incubated in acidified media (pH 6.8) for 7 days with no changes in media, **(c)** Fibroblasts incubated in acidified media (pH 6.5) for 7 days with no changes in media, **(d)** Fibroblasts cocultured with MDA-MB-231 breast cancer cells incubated in acidified media (pH 7.4) incubated for 7 days, **(e)** Fibroblasts cocultured with MDA-MB-231 breast cancer cells incubated in acidified media (pH 6.8) incubated for 7 days, **(f)** Fibroblasts cocultured with MDA-MB-231 breast cancer cells incubated in acidified media (pH 6.5) incubated for 7 days. Scale bar is 100 um. Red represents OCT-4^+ cells, and Green represents Vimentin$^+$ fibroblasts.

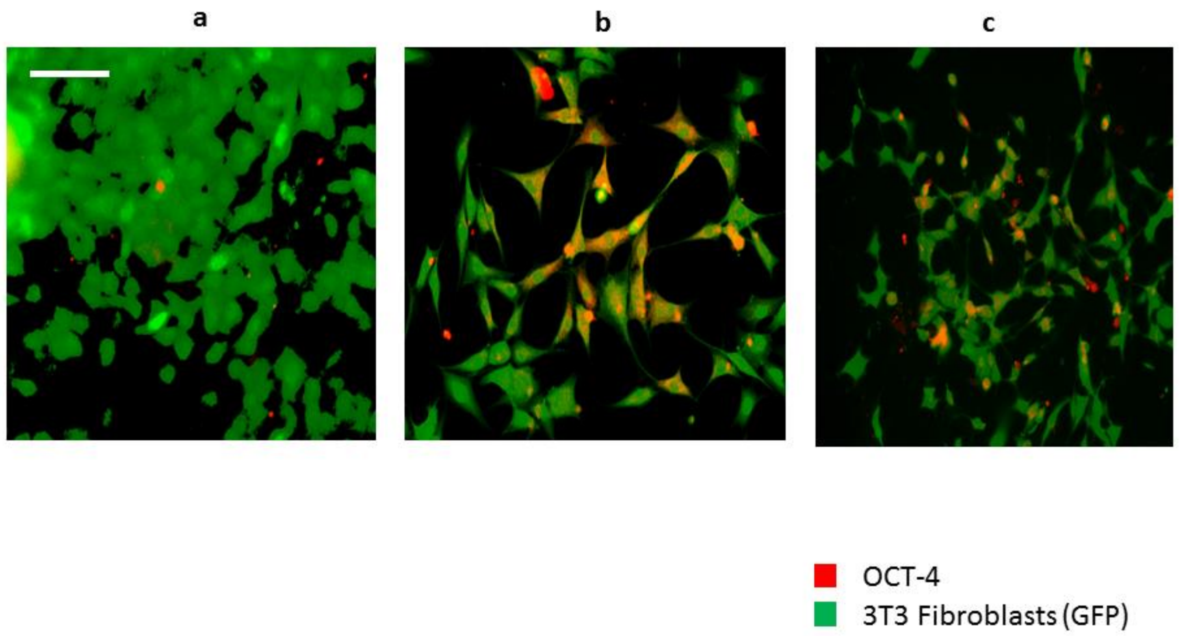

Figure 2.5: Murine monoclonal anti-OCT 4 staining in 3T3 fibroblast cells under different conditions. (a) OCT-4 staining of GFP$^+$ fibroblasts cultured in normal media for 7 days. **(b)** OCT-4 staining of GFP$^+$ fibroblasts cultured in acidified media (pH 6.5) for 7 days. **(c)** OCT-4 staining of GFP$^+$ fibroblasts co-cultured with MDA-MB-231 tumor cells in acidified media (pH 6.5) for 7 days. Red represents OCT-4$^+$ cells, and Green represents GFP+ fibroblasts. Scale bar represents 100 μm and is at 40x magnification. Note Supplementary figure 1b is a replicate of figure 2f and shown here again primarily for comparison.

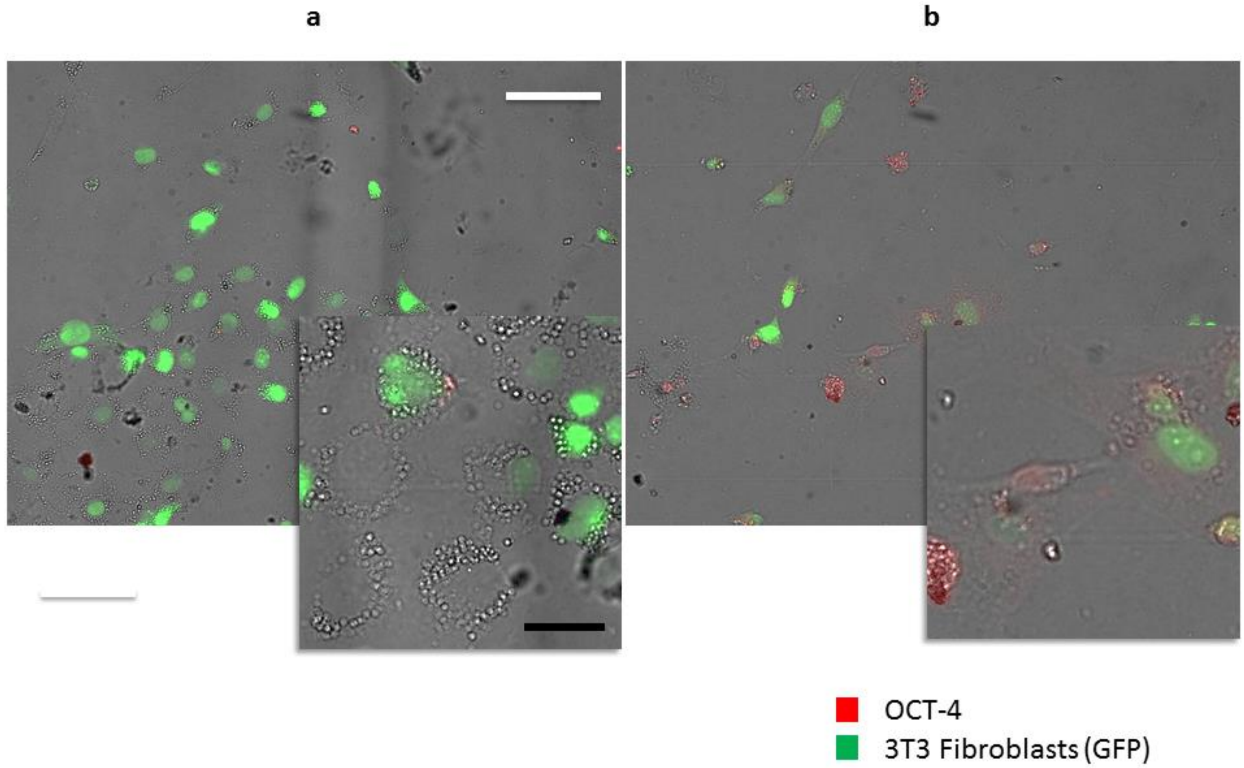

2.6: Co-Culture of Fibroblast-GFP cells with PMEC cells. (a) Co-culture of primary mammary epithelial cells with 3T3-GFP-fibroblasts for 7 days, and stained with OCT-4. **(b)** Co-culture of primary mammary epithelial cells with fibroblasts in acidified media for 7 days. Cells without GFP are primary mammary epithelial cells.

2.3.2 Ex vivo expression of OCT-4 in tumor tissue

We next investigated OCT-4 expression in xenografts from three tumor models: 4T1luc, EMT-6, and BxPC-3. Cardiac muscle was used as an *in vivo* negative control due to the low propensity of that tissue to stem cell activity. Expectedly, we did not detect OCT-4 expression in heart tissue (Figure 2.7). Tumors were 0.5 cm to 1.5 cm in size on excision. The average pH level in 4T1 tumor models was 6.8 +/- 0.1 pH units as measured by an invasive 5 mm probe. This is consistent with previous studies, which reported acidity in BxPC-3 and EMT-6 tumor models and the importance of the pH for chemotherapy resistance.[19] In contrast, OCT-4 expression was detected in all three tumor tissues (Figure 2.8) and was localized to certain cells in and around the tissue section. The entirety of the section was considered to be tumor. These results suggest that OCT-4 expression spans multiple human and murine tumor types. OCT-4 expression, however, seems to be sparse, with only a few tissue areas showing positive staining.

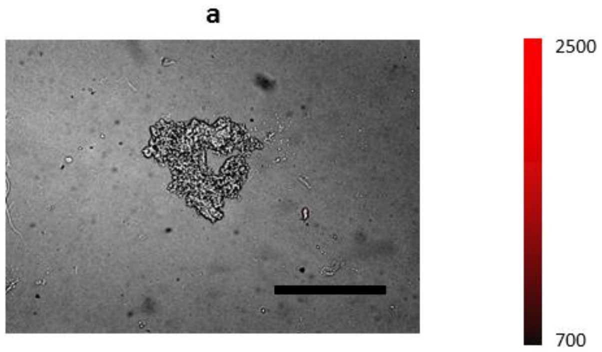

Figure 2.7 Negative control for anti-OCT-4: (a) Heart muscle stained for anti-OCT-4.

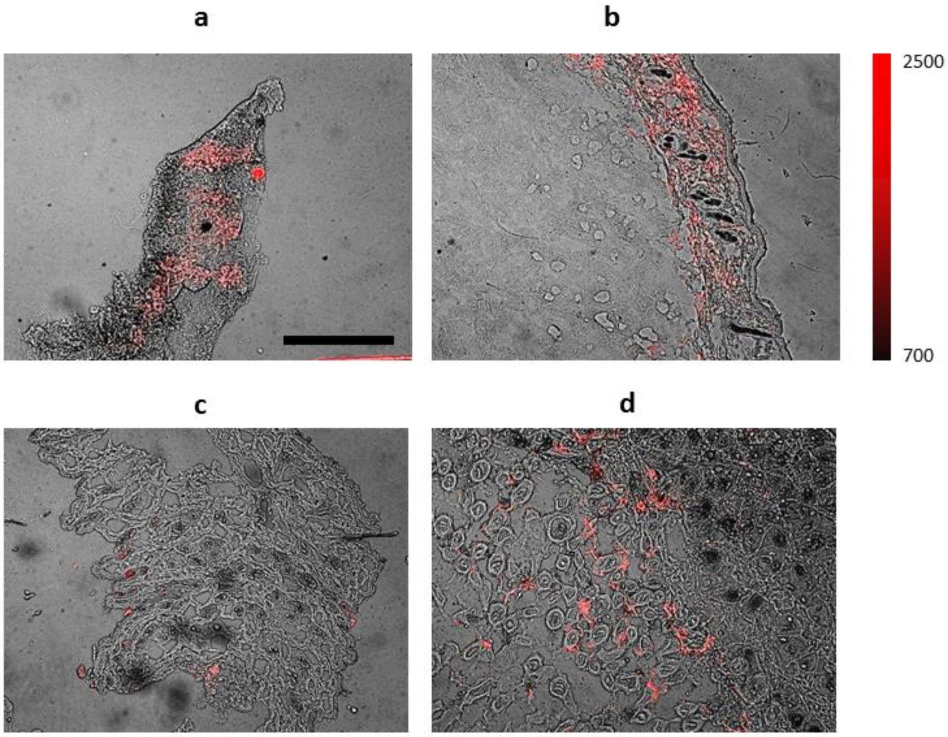

Figure 2.8: Murine Monoclonal anti-OCT-4 staining of tumor and stroma. Oct-4 expression (red) in **(a)** 4T1luc tumor; **(b)** EMT-6; **(c)** 4T1 luc tumor margin; **(d)** BxPC-3 tumor. Scale bar is 500 μm.

2.3.3 Identification of fibroblasts expressing OCT-4 in tumor tissue

Fibroblasts are an important and common cell type in cancer stromal tissue. To verify that the OCT-4 positive cells were fibroblasts, we co-stained tissues for the fibroblast marker vimentin and OCT-4 (Figure 2.9). Co-staining indicated that OCT-4 localized in the vicinity of vimentin positive cells, with several instances of co-localization (yellow, Figure 2.9), suggesting that these cells are indeed fibroblasts. Our data suggest the presence of three populations of cells: OCT-4$^+$, vimentin$^+$, and a subset of cells positive for both OCT-4 and vimentin. MDA-MB-231 is a human breast cell carcinoma cell line that has high intrinsic expression of OCT-4. We did not assess subcellular distribution of OCT-4 or vimentin in the tissue sections.

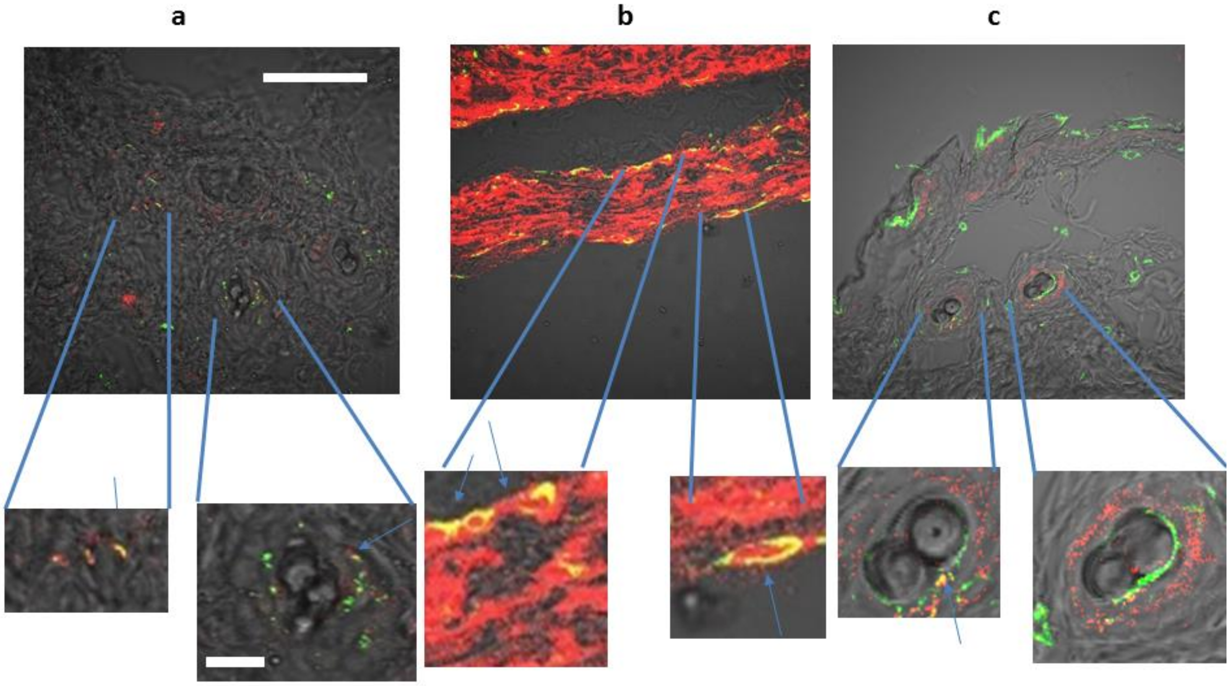

Figure 2.9: Co-staining for OCT-4 (red) & Vimentin (green) in tumor tissues. 10x bright field images with crop-outs being subsets of the original 10X images. **(a)** Co-staining of BxPC-3 tumor tissue **(b)** Staining of MDA-MB-231 tumor tissue **(c)** Staining of EMT-6 tumor Yellow indicates areas of co-localization. Scale bar represents 500 μm for the low magnification image, and 100 μm for magnified regions.

Literature values and independent pH measurements in our laboratory show that the pH in the tumor area ranges from 6.5-7.0. By chronically maintaining the extracellular pH below 7, cancer cells can stimulate non-tumor cells to reprogram via pH-related stress. This process could aid the recruitment of surrounding cells into the tumor matrix.[2,20]

2.4 Discussion

The extracellular pH of tumors has been implicated in the metastasis and behavior of tumor cells, and changes in this pH could modify the downstream behavior of cancer. [18] To our knowledge, this is the first report of the expression of OCT-4 in the vicinity of tumors, particularly in supporting stromal cells. Stress based *in vitro* OCT-4 expression has been reported previously for stem cells.[14,21] Our data suggests that chronic mild acidity, which is present in the tumor environment along with other stressors, is capable of inducing OCT-4 expression in murine fibroblasts and may be sufficient to induce OCT-4 expression *in vivo*. These observations suggest that tumor cells *in vivo* may be capable of reprogramming surrounding stromal cells using environmentally mediated factors.

There are a few caveats to the above platform. The tumors were all xenografts and it is not known if this phenomenon occurs in spontaneous tumor models. We focused primarily on murine fibroblasts to facilitate *in vivo* assessment of the phenomenon with the same cells. It is also unclear if the *in vivo* OCT 4 expression changes with tumor size in this study.

Ex vivo histology showed expression of OCT-4 in cells that are not fibroblasts. Other than MDA MB-231 tumors, which had high intrinsic expression of OCT-4, the positive cells did not make up the bulk of the tumor mass. We posit that these cells may be endothelial or other epithelial cells in the stromal region, or perhaps some small subset of cancer cells. This hypothesis is supported by *in vitro* expression of $OCT4^+$ in PMEC cells, a primary mammary epithelial cell line, under acidic conditions.

This report offers observational evidence that mild acidity does induce some degree of OCT-4 expression *in vivo*, therefore confirming previous findings about stress based OCT-4 expression. However, it is not clear how long these cells maintain the OCT-4 expression nor if the expression induces any other pluripotent stem cell phenotype. To rule out the possibility of artifact, we tested both a mouse monoclonal and a rabbit polyclonal anti-OCT-4 antibody. We observed similar results with both antibodies, although OCT-4 localization at times alternated between cytoplasmic (murine monoclonal) and nuclear (rabbit polyclonal), depending on the type of antibody used (Figure 2.2, Figure 2.5).

Fibroblasts are traditionally considered to be strong supporting actors in the tumor microenvironment. The concept that chronic physiological extracellular acidity can have significant effects on the expression of reprogramming markers, such as OCT-4 both *in vitro* and *in vivo*, suggests a possible mechanism for the phenotypic changes in cancer associated fibroblasts. One report indicates that acidity may actually transform fibroblasts into cancerous tissue.[22] Some preliminary data (Figure 2.10) demonstrate that implantation of these acid treated cells induces tumor growth in athymic nude mice. For this study, fibroblast cells were not co-cultured with tumor cells. Further, the concept that acid mediated stress can induce the presence of factors that cause reprogramming *in vivo* raises the question of what happens if intratumoral pH is changed *in vivo*. Indeed, pH changes *in vivo* can inhibit tumor growth.[23]

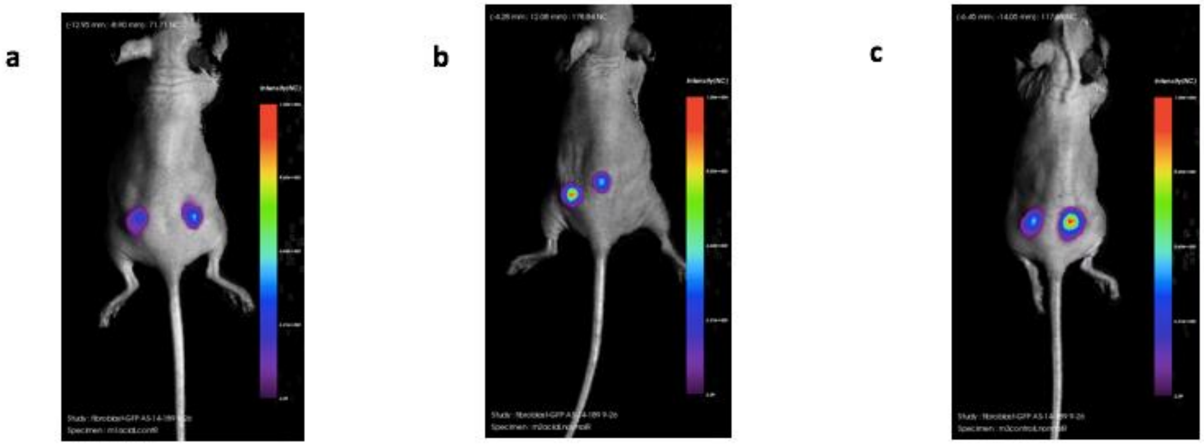

Figure 2.10: Dorsal GFP images of in vivo growth of acid treated fibroblasts. (a) GFP image of mouse 1: acid treated 3T3 cells on its left flank, and 7 day pH 7.4 treated 3T3 cells in its right flank. **(b)** GFP image of mouse 2: acid treated 3T3 cells on its left flank, and 1 day pH 7.4 treated 3T3 cells in its right flank. **(c)** GFP image of mouse 3: 7 day control 3T3 cells on its left flank, and 1 day pH 7.4 treated 3T3 cells in its right flank.

Overall, this study reveals that the stroma of tumors express OCT-4. Based on *in vitro* data, it is likely that chronic mild acidic stress could facilitate cell reprogramming. Given the ubiquity of extracellular acidic environments in some solid cancers, this process could be a common occurrence *in vivo*. We demonstrated that pH evidently has an important effect on both cancer cells and the supporting stroma. These results further support the relevance of the extracellular matrix and its environment to cancer behavior, prognosis, and therapy. In particular, the increasing evidence that tumors actively maintain an extracellular acidic environment implies a causative role for pH in tumor survival and proliferation. There is thus an intersection between the significant work involved in cancer metabolomics, the Warburg effect, and the tumor microenvironment. Future work will focus on replicating this observed phenomenon *in vivo* in human subjects, as well as developing a platform to modulate this acidic pH *in vivo.*

2.7 Copyright acknowledgment

All figures and work in this chapter was taken from the following manuscripts whose citation is below.

Avik Som, Sharon Bloch, Joseph E. Ippolito, Samuel Achilefu “Acidic extracellular pH of tumors induces octamer-binding transcription factor 4 expression in murine fibroblasts *in vitro* and *in vivo”* Scientific Reports 2016

2.8 References

1 Lee, C. *et al.* Role of the adjacent stroma cells in prostate cancer development and progression: synergy between TGF-beta and IGF signaling. *Biomed Res Int* **2014**, 502093, doi:10.1155/2014/502093 (2014).

2 Kalluri, R. & Zeisberg, M. Fibroblasts in cancer. *Nature reviews. Cancer* **6**, 392-401, doi:10.1038/nrc1877 (2006).

3 Goubran, H. A., Kotb, R. R., Stakiw, J., Emara, M. E. & Burnouf, T. Regulation of tumor growth and metastasis: the role of tumor microenvironment. *Cancer Growth Metastasis* **7**, 9-18, doi:10.4137/CGM.S11285 (2014).

4 Gatenby, R. A., Gawlinski, E. T., Gmitro, A. F., Kaylor, B. & Gillies, R. J. Acid-mediated tumor invasion: a multidisciplinary study. *Cancer Res* **66**, 5216-5223, doi:10.1158/0008-5472.CAN-05-4193 (2006).

5 Catalano, V. *et al.* Tumor and its microenvironment: a synergistic interplay. *Semin Cancer Biol* **23**, 522-532, doi:10.1016/j.semcancer.2013.08.007 (2013).

6 Pietras, K. & Ostman, A. Hallmarks of cancer: interactions with the tumor stroma. *Exp Cell Res* **316**, 1324-1331, doi:10.1016/j.yexcr.2010.02.045 (2010).

7 Bhowmick, N. A. & Moses, H. L. Tumor-stroma interactions. *Curr Opin Genet Dev* **15**, 97-101, doi:10.1016/j.gde.2004.12.003 (2005).

8 Mishra, P., Banerjee, D. & Ben-Baruch, A. Chemokines at the crossroads of tumor-fibroblast interactions that promote malignancy. *J Leukoc Biol* **89**, 31-39, doi:10.1189/jlb.0310182 (2011).

9 Chen, S. Y. *et al.* Dependence of fibroblast infiltration in tumor stroma on type IV collagen-initiated integrin signal through induction of platelet-derived growth factor. *Biochim Biophys Acta* **1853**, 929-939, doi:10.1016/j.bbamcr.2015.02.004 (2015).

10 Augsten, M. Cancer-associated fibroblasts as another polarized cell type of the tumor microenvironment. *Front Oncol* **4**, 62, doi:10.3389/fonc.2014.00062 (2014).

11 Borovski, T., De Sousa, E. M. F., Vermeulen, L. & Medema, J. P. Cancer stem cell niche: the place to be. *Cancer Res* **71**, 634-639, doi:10.1158/0008-5472.CAN-10-3220 (2011).

12 Sneddon, J. B. & Werb, Z. Location, location, location: the cancer stem cell niche. *Cell Stem Cell* **1**, 607-611, doi:10.1016/j.stem.2007.11.009 (2007).

13 Li, L. & Neaves, W. B. Normal stem cells and cancer stem cells: the niche matters. *Cancer Res* **66**, 4553-4557, doi:10.1158/0008-5472.CAN-05-3986 (2006).

14 Hjelmeland, A. B. *et al.* Acidic stress promotes a glioma stem cell phenotype. *Cell Death Differ* **18**, 829-840, doi:10.1038/cdd.2010.150 (2011).

15 Raymond L. Page *et al.* Induction of Stem Cell Gene Expression in Adult Human Fibroblasts without Transgenes. *Cloning and Stem Cells* **11**, 417-426, doi:10.1089/clo.2009.0015 (2009).

16 Agatha S. E. Ojugo *et al.* Measurement of extracellular pH of solid tumors in mice by MR Spectroscopy. Comparison of exogenous 19F and 31 P probes. *NMR in Biomedicine* **12**, 495-504 (1999).

17 Zhang, X., Lin, Y. & Gillies, R. J. Tumor pH and its measurement. *J Nucl Med* **51**, 1167-1170, doi:10.2967/jnumed.109.068981 (2010).

18 Estrella, V. *et al.* Acidity generated by the tumor microenvironment drives local invasion. *Cancer Res* **73**, 1524-1535, doi:10.1158/0008-5472.CAN-12-2796 (2013).

19 Fukamachi, T. *et al.* Tumor specific low pH environments enhance the cytotoxicity of lovastatin and cantharidin. *Cancer Letters* **297**, 182-189 (2010).

20 Ana-Maria Bamberger, I. T., and Heinrich M. Schulte. Differential regulation of the human 'leukemia inhibitory factor' (LIF) promoter in T47D and MDA-MB 231 breast cancer cells. *Breast Cancer Research and Treatment* **47**, 153-161 (1998).

21 Obokata, H. *et al.* Stimulus-triggered fate conversion of somatic cells into pluripotency. *Nature* **505**, 641-647, doi:10.1038/nature12968 (2014).

22 Tavakol, S. Acidic pH derived from cancer cells may induce failed reprogramming of normal differentiated cells adjacent tumor cells and turn them into cancer cells. *Med Hypotheses* **83**, 668-672, doi:10.1016/j.mehy.2014.09.014 (2014).

23 Robey, I. F. *et al.* Bicarbonate increases tumor pH and inhibits spontaneous metastases. *Cancer Res* **69**, 2260-2268, doi:10.1158/0008-5472.CAN-07-5575 (2009).

Chapter 3: Mathematical simulation of a pH modulating nanoparticle: Identification of Calcium Carbonate as an ideal candidate for increasing pH *in vivo*

Chapter Summary

Modeling the pH change *in vivo* from a nanomaterial can be used to identify the ideal material for increasing pH *in vivo*, as well as give insight on expected pH changes and pharmacokinetics. In this chapter, we demonstrate a unique physiological pH sensitivity by $CaCO_3$ due to the high stable calcium concentration *in vivo*. In particular, the results of this chapter predict that $CaCO_3$ nanoparticles will increase pH only in physiologically acidic regions without any resultant metabolic alkalosis. In the process, we develop a simulation for nanoparticle distribution and degradation.

3.1 Introduction:

Recently, tumor extracellular acidity has been revisited as a potential target for cancer therapy. Models on tumor extracellular pH (pHe) demonstrate a significant correlative relationship between tumor invasiveness and the increased production of acid in most tumors. [1,2] To maintain normal intracellular pH (pHi) and to promote growth by degradation of the extracellular matrix, tumor cells actively transport the excess protons generated during enhanced glycolysis, the Warburg effect, to the extratumoral environment. [3] This leads to a sustained acidic tumor environment, with an average extracellular pH of 6.8, as opposed to the buffered and highly regulated interstitial pH of about 7.4 in the vicinity of healthy tissue.[4] Cells are thought to actively use this 4 fold increase in hydrogen ion concentration to degrade the tumor matrix and thus sustain its growth. [2,3] This has led to a hypothesis that low pHe may be important for inducing tumor growth and metastasis.

Local extracellular acidity has been demonstrated to have active effects on a variety of tumor and stromal cells. For instance, *in vitro* and *in vivo* trials have demonstrated immunologic anergy in cytotoxic T cells suggestive of possible reasons for tumors avoiding immunosurveillance in spite of the high lymphocytic presence in many tumors. [5,6] Other trials have demonstrated the upregulation of a variety of proteins, including p53 and p21, when placed under acidic conditions *in vitro*. [7,8] In addition, modulating extracellular acidity appears to change chemotherapy sensitivity in tumors putatively due to changes in charge of drug molecules and intracellular signaling changes downstream. [8-10] Given that pH in cancer can follow a wide range (5.6 - 7.0)[4,8], depending on type and size, clinical variability seen under chemotherapy may be due to underlying pH differences.

Although ample evidence suggests that extracellular pH plays an important role in tumor growth and metastasis, most studies modulating extracellular pH *in vivo* have been impractical to implement clinically. We explore herein using a nanoparticle approach to modulate intratumoral pH. One candidate includes $CaCO_3$. $CaCO_3$ has a low solubility in water, allowing its presence in nanoparticle form within aqueous solutions[11-15] and relatively high pKa of 9, ensuring rapid pH increase under acidic conditions. In addition, $CaCO_3$ can deliver $9.03*10^6$ protons per 100 nm particle, a thousand fold increase over dendrimeric approaches in terms of capacity. Other groups have used $CaCO_3$ particles for acid sensitive drug delivery[11-13,15] suggesting it is a prime candidate for buffering only in tumor acidic regions. $CaCO_3$ also has the additional advantage of being composed of natural products found in the body, and because it follows basic chemistry for rate equations, the dissolution and solubility *in vivo* can be simulated easily. Nevertheless, mathematical models do not yet exist to predict what change of pH would occur *in vivo*.

Nanomaterials remain a largely empirical science. Much of the synthesis and production has been done by trial and error. Although modeling of polymer growth and kinetics are well known, atom by atom based modeling breaks down at the greater than ten nanometer size range to become non-practical due to data size and computing time constraints. As such relatively little though has been done to simulate and then predict what changes will occur *in vivo* post nanoparticle administration.

There are however a few principles that have been established to understand dynamics based on observations, including the importance of surface charge and functionalization to stability. Thus far modelling has been applied to networks of hydrogels[16] such as nanoparticle transport in coronary arteries [17], modeling of particle erosion and drug release [18-21], and kinetics of aggregation for gold nanoparticles [22]. Simulations thus far have largely focused on using chemical engineering techniques, diffusion laws, and mass transfer equations, or modeling based on existing data. These may allow for predictions of behavior, including elements such as pH response *in vivo* that can guide design and application.[23]

$CaCO_3$ nanoparticle diffusion in the tumor, and its potential subsequent effect on pH has not yet been simulated. Doing so would provide a mathematical model to explain its diffusion and change in pH under varying tumor circumstances, potentially gleaning an understanding of how to improve its efficacy in changing tumor pH *in vivo*.

3.2 Methods

3.2.1 Overall methodology of the simulation of $CaCO_3$ dissolution in vivo.

Simulations were run in MATLAB using a numerical iteration approximation. Equations (1-6) are derived from a tissue cylinder model of diffusion and diffusion of $CaCO_3$ from a nanoparticle under the conditions of constant infusion. Equations (5) and (6) were used to determine the initial $CaCO_3$ and pH distributions in the tissue cylinder model. Changes in $CaCO_3$ and pH were then numerically approximated using equations (3) and (4).

$$CaCO_3(s) \leftrightharpoons Ca^{2+} + CO_3^{2-} \qquad (K_{a1} = 4.45 * 10^{-7}) \tag{1a}$$

$$H_2O + HCO_3^{-} \leftrightharpoons H_3O^{+} + CO_3^{2-} \ (K_{a2} = 4.69 * 10^{-11}) \tag{1b}$$

$$H_2O + H_2CO_3 \leftrightharpoons H_3O^{+} + HCO_3^{-} \tag{1c}$$

$$\text{Solubility } (\mathbf{C_b}) = \sqrt{\frac{K_{sp}}{\frac{K_{a1} * K_{a2}}{((10^{-pH})^2 + K_{a1} 10^{-pH} + K_{a1} K_{a2})}}} \tag{2}$$

$$J = -D\frac{dC}{dx} \rightarrow \frac{\partial C}{\partial t} = \frac{A}{V} D \frac{(C_s - C_b)}{d} \rightarrow \frac{\partial m}{\partial t} = AD\frac{(C_s - C_b)}{d} \rightarrow \frac{\partial r}{\partial t} = \frac{D}{\rho}\frac{(C_s - C_b)}{d} \tag{3}$$

$$\frac{dpH}{dt} = -\frac{D}{B}\frac{(C_s - C_b)}{d} * \frac{1}{L} \tag{4}$$

$$[CaCO_3] = \frac{R_{cmax}}{4D_c}(r_c^2 - r^2) + \frac{R_{cmax} r_c^2}{2D_c} \ln\left|\frac{r}{r_c}\right| + k * C_d \tag{5}$$

$$[H^{+}] = \frac{R_{pmax}}{4D_p}(r^2 - r_c^2) + \frac{R_{pmax} r_c^2}{2D_p} \ln\left|\frac{r_c}{r}\right| + 10^{-7.4} \qquad (6)$$

The solubility of $CaCO_3$ (C_b), in equation (2) is a function of pH, the solubility product (K_{sp}), and equilibrium constants K_{a1} and K_{a2}, obtained from equations (1a, 1b). The rate of change in $CaCO_3$ concentration (C) and in particle radius (r), seen in equation (3), are derived from Fick's law, and is a function of the diffusion coefficient (D), the surface area of diffusion (A), the distance of diffusion (d) estimated at 0.1 mm, the solubility of $CaCO_3$ (C_b), the volume of the tissue cylinder (C), and the concentration of $CaCO_3$ *in vivo* (C_s). For equation (4), we simplified equation (3) by approximating A/V to 1/L, where L is the length of the tissue cylinder, estimated at 1 mm. The change in concentration of protons can then be converted to a change in a pH of a buffer by dividing by buffering constant, B= 28 mM/pH.[35]

For equation (5), R_{cmax} was empirically determined by starting at the maximum degradation rate in the tissue at pH of 6.65 and then multiplying by a correction factor until the distribution of $CaCO_3$ appeared optimal, in this case approximately 0.5 mm from the capillary. The resulting degradation correction factor was used throughout for simulating $CaCO_3$ degradation. The radius of the capillary (r_c) was set at 10 $\boldsymbol{\mu}$m. The partition coefficient (k) of the capillary is dependent on the capillary pore radius, estimated at 500 nm and particle radius, defined as 100 nm. The initial concentration of $CaCO_3$ (C_d) in the capillary was estimated as 5% of the infused concentration (set as 1 mg in a 20 g mouse).

R_{pmax} was empirically determined as the point at which the average pH in the tissue was 6.65, identified as 0.0225 M/s. The diffusion coefficient (D_p) was estimated as the diffusion of a particle with a molecular weight of 1 Da in an extracellular matrix. We used the following constants for the simulation based on literature values or model assumptions: r = 50 nm, $K_{a1} = 4.45*10^{-7}$, $K_{a2} = 4.69*10^{-11}$, $K_{sp} = 6*10^{-9}$, M = 100.0869 g/mol, ρ = 2.71 g/mL.

3.2.1.1 Modeling IV Injection

The derivation of the above equations are as follows. In general, we can assume that under ideal conditions the $CaCO_3$ particles are injected via intravenous infusion, allowing for a constant stable concentration within the blood. The particles can also be assumed to not enter cells due to the lack of any targeting motifs. We can assume that the liver, spleen, and kidney, remove approximately 95% of $CaCO_3$ dose, as suggested by radioactive Cu^{64} experiments. As such, we make the assumption that the dose of $CaCO_3$ at the tumor site is:

$$(7)\ C_b = 0.05 C_{infused}$$

As the particles enter the tumor, we can look at the tumor vasculature model as a parallel combination of tissue cylinders, each composed of a cylinder of length z, radius $r_c = \frac{1}{2} d_c$, and a pore size of r_p. The particles themselves should not have changed significantly, based on TEM images of serum incubation, and as such should retain their initial diameter a. Each capillary supplies a tissue area of radius r_t which marks the boundary of that tissue cylinder. Because the tumors are poorly perfused, we can also make the assumption that the tissue cylinder has negligible contributions to it from other capillaries. (Figure 3.1)

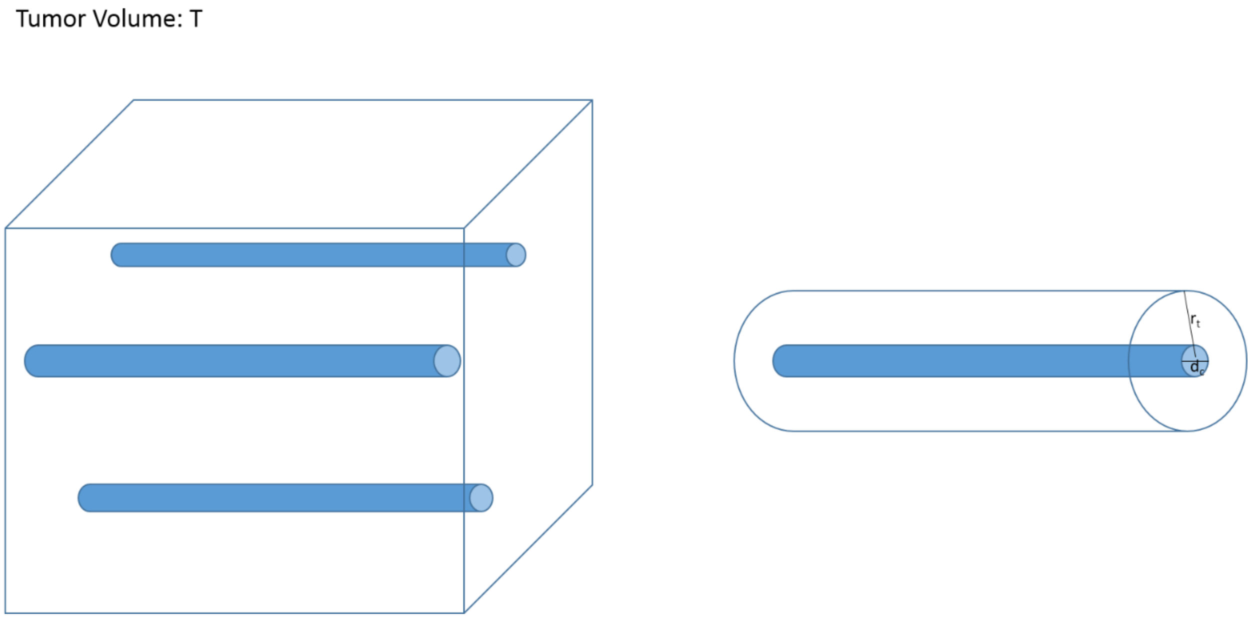

Figure 3.1: Visualization of the tumor tissue cylinder. Blue cylinder represents a blood vessel of diameter d, in a tissue cylinder of r_t. A tumor volume is simulated as a sum of these cylinders

3.2.1.2 Modeling Pre-Injection pH gradient

The pH at r= r_c is maintained at a pH of 7.4. However within the tumor tissue, there is some rate of proton production R_{pmax} that is a function of pH. We assume there is no convection of protons, no contribution from $\frac{d}{d\theta}$, and $\frac{d}{dz}$, and the system is at steady state. We can also make the assumption that the system is smooth, and as such, $@r = r_c \ \frac{d[H^+]}{dr} = 0$. As such, we can derive the distribution of protons in the tumor tissue from the equations.

$$(8) \quad 0 = -\frac{1}{r}\frac{d}{dr}\left(rD_p\frac{d[H^+]}{dr}\right) + R_{pmax}$$

$$(9) \quad [H^+] = \frac{R_{pmax}}{4D}(r^2 - r_c^2) + \frac{R_{pmax}r_c^2}{2D}ln|r_c/r| + 10^{-7.4}$$

$$(10) \quad D = 1.013 * 10^{-4} * 1^{-.46}$$

We assume: $R_{pmax} = constant = 0.0225$ empirically identified as the point that makes the average pH=~6.8

The resulting proton gradient in the tissue can be seen in Figure 3.2.

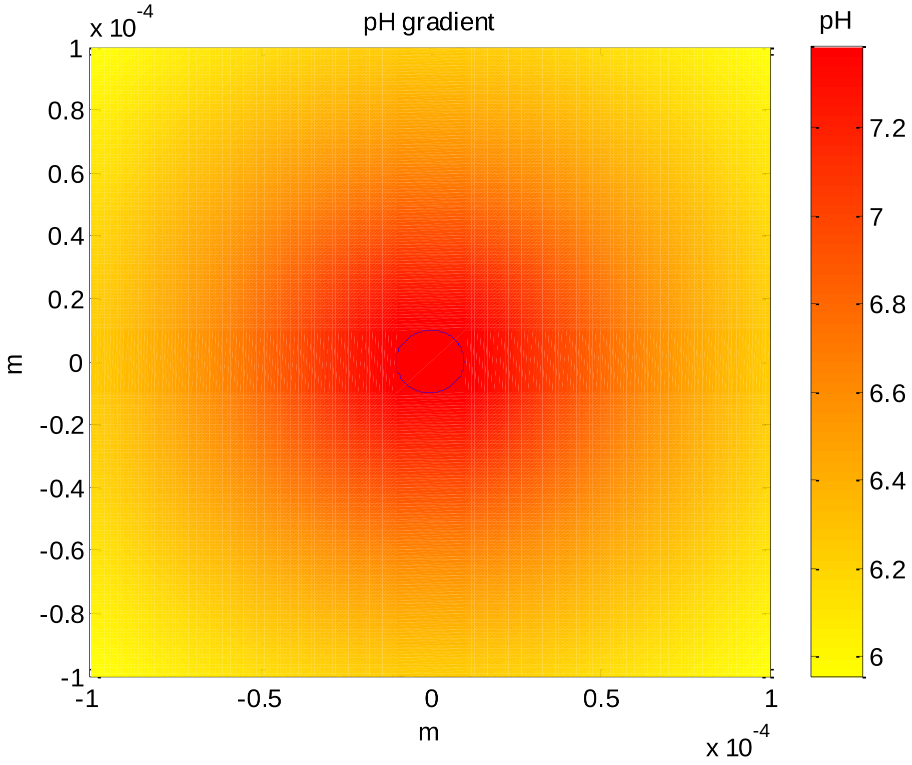

Figure 3.2: pH gradient in a tumor. The blue circle represents the capillary area. The tissue cylinder is approximated in the figure as being 100 μm large.

3.2.1.3 Modeling CaCO$_3$ Diffusion in the Tumor

The capillary also contains pores that range in size from 100 to 500 nm depending on tumor type. For the purpose of this simulation, we can assume the pore size is $r_p = 500$ nm. This results in a partition coefficient:

(11) $$k = \left(1 - \frac{a}{r}\right)^2$$

The concentration of CaCO$_3$ immediately outside of the capillary then can be calculated as:

(12) $$C_t = k * C_b = 0.05 * k * C_{infused}$$

The tumor tissue consumes this CaCO$_3$ at a rate R_{cmax}. We can assume, similar to the proton gradient that there is no convection of CaCO$_3$, no contribution from $\frac{d}{d\theta}$, and $\frac{d}{dz}$, and the system is at steady state. We can also make the assumption that the system is smooth, and as such, $@r = r_c \ \frac{d[CaCO_3]}{dr} = 0$. As such, we can derive the distribution of CaCO$_3$ in the tumor tissue from the formula:

(13) $$0 = -\frac{1}{r}\frac{d}{dr}\left(rD_p \frac{d[CaCO_3]}{dr}\right) - R_{cmax}$$

(14) $$[CaCO_3] = \frac{R_{cmax}}{4D}(r_c^2 - r^2) + \frac{R_{cmax} r_c^2}{2D} ln \left|\frac{r}{r_c}\right| + k * C_b$$

To calculate the diffusion coefficient through the interstitial fluid we can use the following equations. The diffusion of CaCO$_3$ in plasma :

(15) $$D_{plasma} = \frac{k_B T}{6\pi\mu R}; \ T= 37C, \ kB=, \ \mu, \ R = 50 * 10^{-9} \ m$$

(16) $$\frac{D_m}{D} = \left(1 - \frac{a}{r}\right)^2 \left[1 - 2.1\left(\frac{a}{r}\right) + 2.09\left(\frac{a}{r}\right)^3 - 0.95\left(\frac{a}{r}\right)^5\right]$$ *(Renkin's equation)*

Make the assumption that Dm =Dif (diffusion in the interstitium for the nanoparticle). Using Maxwell’s equation, we can solve for Dt- diffusion coefficient in tissue.

(17) $\frac{D_T}{D_{IF}} = \frac{2D_{IF}+D_{Cell}-2\phi(D_{IF}-D_{Cell})}{2D_{IF}+D_{CEll}+\phi(D_{IF}-D_{Cell})}$ *; For* $CaCO_3$ *Dcell = 0;*

(18) $\frac{D_T}{D_{IF}} = \frac{2D_{IF}-2\phi(D_{IF})}{2D_{IF}+\phi(D_{IF})}$ *; assume* $\phi = 0.7$, *cell fraction of volume*

(19) $D_T = \frac{2D_{IF}-2\phi(D_{IF})}{2D_{IF}+\phi(D_{IF})} D_{IF}$

3.2.1.4 Calculating degradation of $CaCO_3$ (Rcmax) as a function of pH

Rcmax, however is not constant, but is instead a function of pH, with increased degradation at lower pHs. CaCO3 dissolution can be determined as a function of pH using the following formulas.

(20) $CaCO_3$ *dissolution is mediated by the following three equations.*

$$CaCO_3(s) <-> Ca^{2+} + CO_3^{2-}$$

$$H_2O + HCO_3^- <-> H_3O^+ + CO_3^{2-}$$

$$H_2O + H_2CO_3 <-> H_3O^+ + HCO_3^-$$

Using standard reaction rate equations one can determine the solubility of $CaCO_3$ in a biological medium as a function of pH.

(21) $C_b = \sqrt{\frac{K_{sp}}{\frac{K_{a1}*K_{a2}}{((10^{-pH})^2+K_{a1}10^{-pH}+K_{a1}K_{a2})}}}$

The change in radius in each particle can be determined as:

(22) $$\frac{\partial r}{\partial t} = \frac{D_{CaCo_3}}{a\rho}(C_s - C_b)$$

The change in pH then at any point can be further determined as:

(23) $$\frac{\partial pH}{\partial t} = \frac{D}{a} * 4\pi(\frac{a}{2})^2 * (C_s - C_b) * \frac{N}{M} * \left(\frac{4}{3}\pi d^3 - \frac{4}{3}\pi(\frac{a}{2})^3\right) * \frac{1}{B}$$

The rate of degradation then Rcmax =

(24) $$R_{cmax} = -D * (C_s - C_b)$$

To simplify the simulation, assume that Rcmax is average across all of the space based on the average pH in the tumor volume. If so, we can calculate Rcmax under the conditions at t=0, to calculate the initial distribution of $CaCO_3$. We assume that $CaCO_3$ does not change size significantly in aggregate during diffusion through the matrix while being consumed.

3.2.1.5 Modeling change in pH over time

As the $CaCO_3$ is consumed in each space point, the $CaCO_3$ changes as does the pH. This can then be iteratively solved per point.

pH changes are equal to:

(25) $$\frac{\partial pH}{\partial t} = D * (C_s - C_b) * dV * \frac{1}{B} \text{ (1/s)}$$

(26) $$pH(x, y) = pH(x, y) + dpH * dt$$

(27) $$pH(x,y) = -\log(10^{-pH} + R_{pmax} * Area);$$

$CaCO_3$ changes are equal to:

(28) $$C_b = \sqrt{\frac{K_{sp}}{\frac{K_{a1} * K_{a2}}{\left((10^{-pH})^2 + K_{a1}10^{-pH} + K_{a1}K_{a2}\right)}}}$$

(29) $$\frac{\partial C}{\partial t} = R_{cmax} = -D * (C_s - C_b)$$

(30) $$C_{CaCO3} = C_{CaCO3} - R_{cmax} * dt * Area$$

i. *When* C_{CaCO3}*=0; iteration stops for that point*

In aggregate, when simulated, the pH appears as visualized in Figure 3.3.

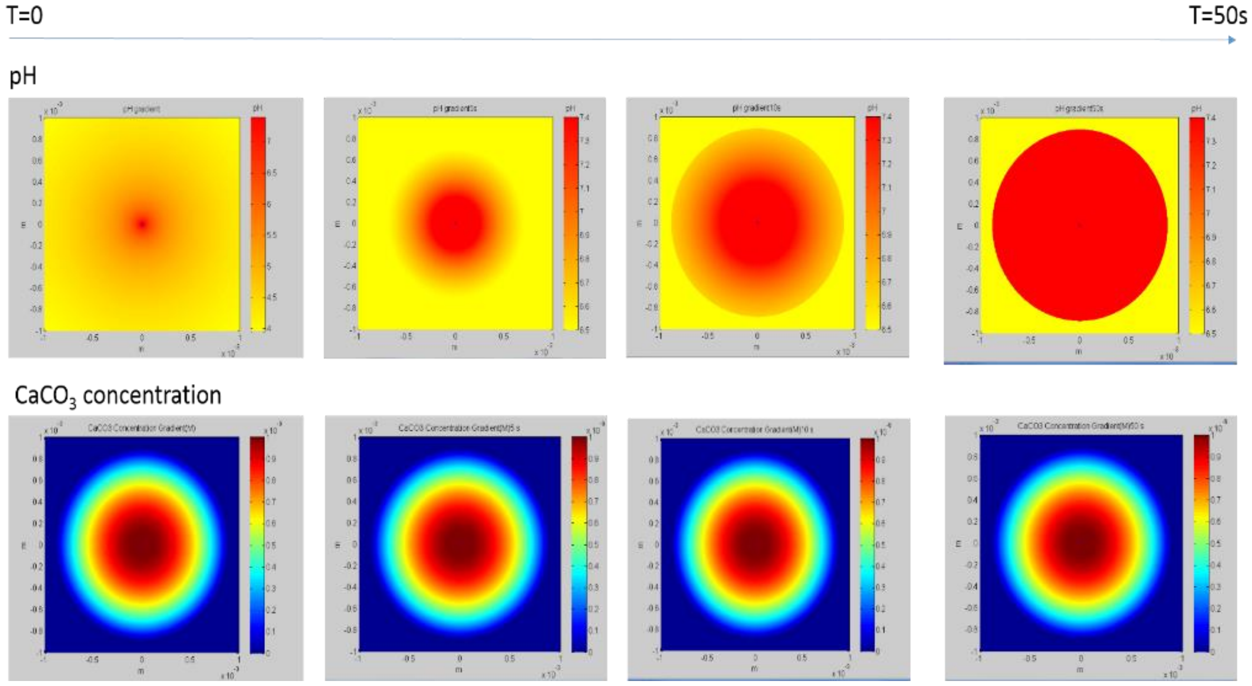

Figure 3.3: Simulated over time, this figure demonstrates the increase in pH around a capillary due to CaCO$_3$. To see the whole change, the tumor is approximately 1 mm x 1 mm. Scales are kept constant from 6.5 to 7.4 (pH), and 0 to 1 μM (CaCO$_3$ distribution)

3.3 Results

3.3.1 Simulation of $CaCO_3$ nanoparticle dissolution in vivo predicts asymptotic pH increase and buffering to pH 7.4

$CaCO_3$ is an important biomaterial that is widely available in different forms. Although $CaCO_3$ solutions can serve as buffering agents, a saturated aqueous solution of this salt has a predicted pK_a of about 9, suggesting the potential to induce metabolic alkalosis in vivo. In the solid state, $CaCO_3$ exists predominantly as calcite, aragonite, or vaterite polymorphs. Each of these polymorphs differ in their crystal lattice structure. Unlike calcite and aragonite, which are not soluble in aqueous medium, vaterite is more soluble because of its low thermodynamic stability compared to the other polymorphs found in nature. For our intended application, slow but consistent dissolution in mildly acidic solutions is an essential criterion for a regenerative pHe buffering agent. To prevent metabolic alkalosis in surrounding healthy tissue, the preferred material should only increase the pH to about 7.4 (normal body pH).

Because $CaCO_3$ dissolution is regulated by basic rate equations, a simulation of its dissolution and prediction of the expected pH changes *in vivo* and *in vitro* is possible (Figure 3.4). Dissolution of $CaCO_3$ under mildly acidic conditions follows several steps:

$$CaCO_3(s) \leftrightharpoons Ca^{2+} + CO_3^{2-} \qquad (K_{a1} = 4.45 * 10^{-7}) \qquad (31a)$$

$$H_2O + HCO_3^- \leftrightharpoons H_3O^+ + CO_3^{2-}\ (K_{a2} = 4.69 * 10^{-11}) \qquad (31b)$$

$$H_2O + H_2CO_3 \leftrightharpoons H_3O^+ + HCO_3^- \qquad (31c)$$

Generation of carbonate in equation (31) drives $CaCO_3$ dissolution under acidic pH conditions following L'Chatelier's principle. Previous studies have modeled the pH changes in response to $CaCO_3$ dissolution in aqueous medium.[24] Adapting this model to a tissue cylinder approach (Figure 3.4a), we derived the following equations:

$$\mathrm{C_b} = \sqrt{\frac{K_{sp}}{\frac{K_{a1}*K_{a2}}{((10^{-pH})^2+K_{a1}10^{-pH}+K_{a1}K_{a2})}}} \tag{32}$$

$$J = -D\frac{dC}{dx} \rightarrow \frac{\partial C}{\partial t} = \frac{A}{V}D\frac{(C_s-C_b)}{d} \rightarrow \frac{\partial m}{\partial t} = AD\frac{(C_s-C_b)}{d} \rightarrow \frac{\partial r_p}{\partial t} = \frac{D}{\rho}\frac{(C_s-C_b)}{d} \tag{33}$$

$$\frac{dpH}{dt} = -\frac{D}{B}\frac{(C_s-C_b)}{d} * \frac{1}{L} \tag{34}$$

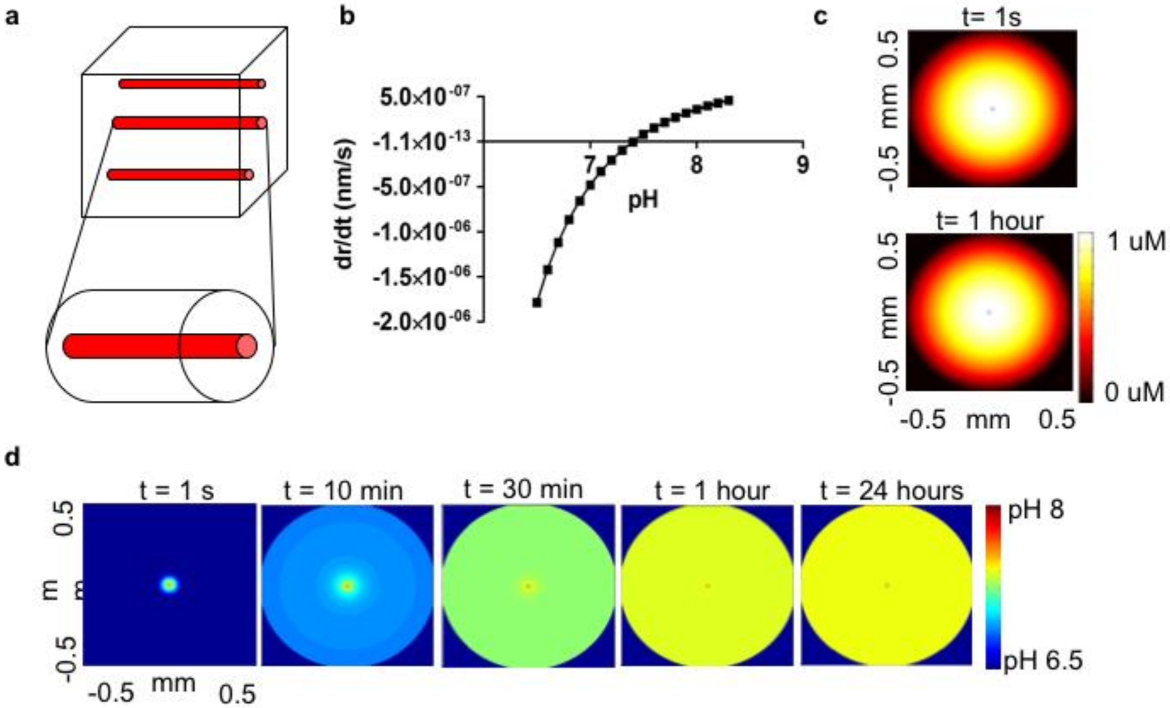

Fig. 3.4 Simulation of $CaCO_3$ dissolution *in vivo* predicts tumor pHe will increase only to 7.4. (a) Tissue can be simulated as a series of cylindrical capillaries each supplying a larger cylindrical volume of tissue. (b) Rate of change in size of $CaCO_3$ particle reaches an equilibrium at pH = 7.4 under in vivo conditions. (c) The distribution of 100 nm $CaCO_3$ nanoparticles in a circular cross section is simulated to reach ~0.5 mm away from the capillary with constant infusion and degrades minimally over 60 minutes. (d) Spatial pH distribution over time increases from 6.5 to 7.4 by 60 minutes, and remains at 7.4 for at least 24 h. Capillary source is represented by blue circle in both (c) and (d).

The solubility of $CaCO_3$ (C_b) is a function of the solubility product (K_{sp}), pH, and the equilibrium constants (K_{a1} and K_{a2}). Change in concentration of $CaCO_3$ is a function of the $CaCO_3$ concentration (C_s), the solubility (C_b), the surface area (A), the diffusion distance (d), and volume (V). The radius of the particle (r_p) is additionally dependent on the density of $CaCO_3$ (ρ). The change in pH is also dependent on the buffering constant, and approximates A/V as 1/L, where L is the length of the tissue cylinder. Using equations (32-34), an equilibration point occurs for dissolving $CaCO_3$ at a pH of 7.4 (Figure 1b). This suggests that $CaCO_3$ will only increase pH in acidic environments such as those found in the pHe of solid tumors and that this process is unlikely to induce metabolic alkalosis because the pH will not exceed 7.4.

To visualize this process in a 3D model, we modeled nano-$CaCO_3$ diffusion in a tissue matrix using a tissue cylinder model (Figure 1a), where a single capillary is assumed to feed a tissue cylinder. From this model, we derived the equation for the distribution of $CaCO_3$ in the tissue cylinder as a function of the radius (r), capillary radius (r_c), diffusion coefficient of $CaCO_3$ (D_c), the partition coefficient (k), degradation rate (R_{cmax}), and the influx dose (C_d) as follows:

$$[CaCO_3] = \frac{R_{cmax}}{4D_c}(r_c^2 - r^2) + \frac{R_{cmax} r_c^2}{2D_c} \ln\left|\frac{r}{r_c}\right| + k * C_d \qquad (35)$$

The diffusion coefficient (D_c) of the particle in tissue, which is dependent on particle size, was estimated using the Renkin equation.[25] We also derived the initial pH distribution from diffusion of protons from the capillary to be the following as a function of the rate of proton production (R_{pmax}), diffusion of the proton (D_p), radius (r), and capillary radius (r_c):

$$[H^+] = \frac{R_{pmax}}{4D_p}(r^2 - r_c^2) + \frac{R_{pmax} r_c^2}{2D_p} \ln\left|\frac{r_c}{r}\right| + 10^{-7.4} \qquad (36)$$

The change in proton concentration is thus determined by numerically solving equations (32), (34), and (36) by iteration. Similarly, $CaCO_3$ concentrations can be calculated by using a combination of equations (32), (33), and (35) over the associated tissue cylinder. We find that the $CaCO_3$ concentrations are relatively constant over time, predicting a particularly slow dissolution process (Figure 3.4c). In addition, the simulation predicts that the pH does not exceed its maximum of 7.4 by 24 h (Figure 1d). This profile predicts that *in vivo* $CaCO_3$ dissolution is acid selective and therefore is an ideal nanomaterial for modulating the acidic pHe of solid tumors.

3.4 Discussion

We find several interesting observations with regards to the simulation. One is that the simulation predicts a halt in pH increase at pH=7.4. This is ideal for the proposed acid sensitivity of $CaCO_3$ to tumors. However, it goes one step further than seen in the literature by suggesting that the mechanism of $CaCO_3$ equilibration is due to a reaction rate equilibrium. Simulations using the transport phenomena present two independent observations. 1) The $CaCO_3$ distribution area, based on the assumptions above, from one capillary is quite large, extending to almost 1 mm^3. This may be due to an over estimation of the interstitial pore size, or may be real. 2) Previous simulations had suggested a very rapid pH modulation, on a nanosecond time scale. With the distribution simulation, this appears to occur on the order of seconds to minutes, reflecting pH data that we have seen during *in vivo* experiments.

The primary limitation is the assumption of R_{cmax} and solubility of $CaCO_3$ in the area based on the average pH in the area as opposed to a value for every point. Future simulations may take into account these aspects. In doing so, a more accurate simulation may be able to found, particularly during the full degradation phase. The model also currently lacks the ability to take into account that the concentration in blood is not constant during IV injection, but generally a bolus. To account for this, one can use the formula:

(37) $C = C_o e^{-k_{eff}*t}$, *where* k_{eff} *is the clearance rate.*

However, for the $CaCO_3$, clearance rate is unknown, and as such poorly simulated. That may be able to be tackled with data from further studies.

We also assume that the $CaCO_3$ dissolution during the initial distribution phase has negligible impact on $CaCO_3$ radius. Based on the simulation parameters demonstrating that changes in $CaCO_3$ distribution take a significant amount of time, this concept may be true. However, simulating the initial distribution phase of the $CaCO_3$ may be useful.

In addition, for dosing purposes, the simulations suggest that a larger amount of $CaCO_3$ is necessary at the beginning during the pH increase phase than at the point of stability. This implies that a bolus dose followed by a continuous low does infusion would be the ideal dosing range to maintain a normal physiological pH. It also implies that failure to maintain the $CaCO_3$ dosage high enough would result in a return to acidity. Compliance thus will be of large importance.

Finally, the escape of $CaCO_3$ after $CaCO_3$ in the blood stream and/or lymphatics after its disappearance has not been explored. In this simulation, we assume that for time $t>0$, there are no major changes in the $CaCO_3$ distribution in the tumor. However, particles may continue to diffuse differently throughout the tissue as dissolution reduce their individual diameters. Alternatively, they may also return to the blood stream over time, particularly with concentration in the blood stream dropping to close to zero. Accounting for these kinetics would add greatly to the robust nature of the model.

Nevertheless, in conclusion, the current model allows for the testing and understanding of multiple aspects, including 1) the distribution of $CaCO_3$ in tissue as a function of particle size and pore sizes, and 2) the subsequent effects on pH over time. This model provides the ability to predict pH changes in the tumor that would otherwise not be possible.

3.5 Copyright acknowledgment

Portions of this chapter, including all figures were taken with permission from the following manuscripts, with full citations below:

Avik Som, Ramesh Raliya, Limei Tian, Walter Akers, Joseph E. Ippolito, Srikanth Singamaneni, Pratim Biswas, and Samuel Achilefu. "Monodispersed calcium carbonate nanoparticles modulate local pH and inhibit tumor growth in vivo" *Nanoscale* 2015

3.6 References

1 Robert A Gatenby, E. T. G. A Reaction-Diffusion Model of Cancer Invasion. *Cancer Res* **56**, 5745-5753. (1996).

2 Gatenby, R. A., Gawlinski, E. T., Gmitro, A. F., Kaylor, B. & Gillies, R. J. Acid-mediated tumor invasion: a multidisciplinary study. *Cancer Res* **66**, 5216-5223, doi:10.1158/0008-5472.CAN-05-4193 (2006).

3 Marion Stubbs, P. M. J. M., John R. Griffiths, and C. Lidsay Bashford Causes and Consequences of tumour acidity and implications for treatment. *Molecular Medicine Today* **6**, 15-19 (2000).

4 Agatha S. E. Ojugo *et al.* Measurement of extracellular pH of solid tumors in mice by MR Spectroscopy. Comparison of exogenous 19F and 31 P probes. *NMR in Biomedicine* **12**, 495-504 (1999).

5 Bellone, M. *et al.* The acidity of the tumor microenvironment is a mechanism of immune escape that can be overcome by proton pump inhibitors. *Oncoimmunology* **2**, doi:10.4161/onci.22058 (2013).

6 Calcinotto, A. *et al.* Modulation of microenvironment acidity reverses anergy in human and murine tumor-infiltrating T lymphocytes. *Cancer Res* **72**, 2746-2756, doi:10.1158/0008-5472.CAN-11-1272 (2012).

7 Moellering, R. E. *et al.* Acid treatment of melanoma cells selects for invasive phenotypes. *Clin Exp Metastasis* **25**, 411-425, doi:10.1007/s10585-008-9145-7 (2008).

8 Song, C. W., Griffin, R. & Park, H. J. in *Cancer Drug Discovery and Development: Cancer Drug Resistance* (ed B. Teicher) Ch. 2, 21-42 (Humana Press, 2006).

9 Luciani, F. *et al.* Effect of proton pump inhibitor pretreatment on resistance of solid tumors to cytotoxic drugs. *J Natl Cancer Inst* **96**, 1702-1713, doi:10.1093/jnci/djh305 (2004).

10 Thews, O., Gassner, B., Kelleher, D. K., Schwerdt, G. & Gekle, M. Impact of extracellular acidity on the activity of P-glycoprotein and the cytotoxicity of chemotherapeutic drugs. *Neoplasia* **8**, 143-152, doi:10.1593/neo.05697 (2006).

11 Ueno, Y., Futagawa, H., Takagi, Y., Ueno, A. & Mizushima, Y. Drug-incorporating calcium carbonate nanoparticles for a new delivery system. *Journal of controlled release : official journal of the Controlled Release Society* **103**, 93-98, doi:10.1016/j.jconrel.2004.11.015 (2005).

12 Jinhuan Wei *et al.* The inhibition of human bladder cancer growth by calcium carbonate/CalP6 nanocomposite parrticles delivering AIB1 siRNA. *Biomaterials* **34**, 1246-1354 (2013).

13 Svenskaya, Y. *et al.* Anticancer drug delivery system based on calcium carbonate particles loaded with a photosensitizer. *Biophys Chem*, doi:10.1016/j.bpc.2013.07.006 (2013).

14 Fukano, H., Takahashi, T., Aizawa, M. & Yoshimura, H. Synthesis of uniform and dispersive calcium carbonate nanoparticles in a protein cage through control of electrostatic potential. *Inorg Chem* **50**, 6526-6532, doi:10.1021/ic200117x (2011).

15 Kim, S. K., Foote, M. B. & Huang, L. Targeted delivery of EV peptide to tumor cell cytoplasm using lipid coated calcium carbonate nanoparticles. *Cancer Lett* **334**, 311-318, doi:10.1016/j.canlet.2012.07.011 (2013).

16 Lin, C. C. & Metters, A. T. Hydrogels in controlled release formulations: network design and mathematical modeling. *Advanced drug delivery reviews* **58**, 1379-1408, doi:10.1016/j.addr.2006.09.004 (2006).

17 Hossain, S. S., Hossainy, S. F. A., Bazilevs, Y., Calo, V. M. & Hughes, T. J. R. Mathematical modeling of coupled drug and drug-encapsulated nanoparticle transport in patient-specific coronary artery walls. *Computational Mechanics* **49**, 213-242, doi:10.1007/s00466-011-0633-2 (2011).

18 Cruz, L. *et al.* Diffusion and mathematical modeling of release profiles from nanocarriers. *International journal of pharmaceutics* **313**, 198-205, doi:10.1016/j.ijpharm.2006.01.035 (2006).

19 Arifin, D. Y., Lee, L. Y. & Wang, C. H. Mathematical modeling and simulation of drug release from microspheres: Implications to drug delivery systems. *Advanced drug delivery reviews* **58**, 1274-1325, doi:10.1016/j.addr.2006.09.007 (2006).

20 J. Siepmann , A. G. Mathematical modeling of bioerodible, polymeric drug delivery systems. *Advanced drug delivery reviews* **48**, 229-247 (2001).

21 Lucero-Acuna, A. & Guzman, R. Nanoparticle encapsulation and controlled release of a hydrophobic kinase inhibitor: Three stage mathematical modeling and parametric analysis. *International journal of pharmaceutics* **494**, 249-257, doi:10.1016/j.ijpharm.2015.07.049 (2015).

22 Kim, T., Lee, C. H., Joo, S. W. & Lee, K. Kinetics of gold nanoparticle aggregation: experiments and modeling. *Journal of colloid and interface science* **318**, 238-243, doi:10.1016/j.jcis.2007.10.029 (2008).

23 Som, A. *et al.* Monodispersed calcium carbonate nanoparticles modulate local extracellular pH and inhibit tumor growth in vivo *Nanoscale* (2015).

24 Bialkowski, S. *Use of Acid Distributions in Solubility Problems*, 2004).

25 Beck, R. E. & Schultz, J. S. Hindered Diffusion in Microporous Membranes with known pore geometry. *Science* **170**, 1302-1305 (1970).

Chapter 4.

Synthesis and Stabilization of pH Modulating Nanoparticles

Chapter Summary

Nano-$CaCO_3$ crystals show promise to demonstrate impact on tumor growth as both a therapy and as a vehicle, but are not widely adopted due to high batch to batch variability during traditional water based synthesis due to spontaneous crystal growth. $CaCO_3$ crystals have a stable size of approximately 1-2 microns post grinding. The knowledge on how to create and stabilize the formation of nano-scale $CaCO_3$ is lacking. In this study, we discover a novel reproducible vacuum assisted $CaCO_3$ nanocrystal synthesis that increase yield, reduce size, and reduce aggregation. We find that the mechanism of action of synthesis is dependent primarily on the aerosolization of ammonium bicarbonate, with the reproducible size constrained phenomenon primarily due to the nano-crystalline form of ammonium bicarbonate. In this chapter we identify the critical fundamental variables for making this particularly robust technique more widely used for nano-$CaCO_3$ synthesis. Further, we demonstrate the ability for this method to produce other metal carbonate nanocrystals of gold, iron, and zinc carbonate. Finally, we demonstrate the stabilization of nano-$CaCO_3$ using albumin to allow for *in vivo* injection.

4.1 Introduction

Nano-$CaCO_3$ has had a growing interest in a number of applications in tumor therapy as a platform for drug delivery, and its mechanism of synthesis has broader interest in a wide number of fields including geology and bone mineral biology. [1-8] Although a number of groups have attempted to produce $CaCO_3$ nanoparticles, the majority have been developed in water, and nano-$CaCO_3$ water based synthesis is generally not reproducible from batch to batch.[3,9-11] This is due to the rapid crystal growth of $CaCO_3$ when synthesized in water that can make it hard to control crystal type and size.[12,13]

Recently, a gas diffusion anhydrous ethanol assisted method, using $CaCl_2$ dihydrate, was utilized to produce 100 nm amorphous $CaCO_3$ to avoid the crystal growth from water during synthesis.[14] However, the amorphous particles changed crystallinity and grew when added to aqueous solutions, which is a potential problem during injection into *in vivo* systems.

In this chapter we describe the synthesis of nano $CaCO_3$ crystals of the vaterite form using two different techniques that build on the both water and ethanol based synthetic techniques. There is little known about the mechanism of these techniques, such as what variables control size, yield, and distribution. In order to make this method practical, we explore a step by step analysis of the method by investigating variables such as solvent type, concentration and mass of starting reagents, duration of synthesis, and combinations of volume and surface area.

For the gas diffusion method, counterintuitively, we find that the concentration, volume, and surface area of $CaCl_2$ have no effect on size. Instead, we discover that only the number of runs using the same batch of ammonium bicarbonate and the amount of ammonium bicarbonate controls size. TEM analysis of ammonium bicarbonate reveals nanocrystalline precursors whose size follows the above observations and explain the reproducibility. Time, volume, and amount of reagents can change yield. This also allows a wider range of solvents to be used than simply EtOH. We observed that this phenomenon can be found in other organic solvents such as MeOH and DMF, but breaks down in the presence of substantial amounts of water. We also demonstrate that this synthesis technique can be extended to gold, iron, or zinc carbonate crystals.

Based on these observations, we posit a model for the synthesis mechanism based on the aerosolization of ammonium bicarbonate nanocrystals, with larger nanocrystals being aerosolized and deposited first, and smaller ones being deposited later. As such, size, and yield can be controlled by the number of runs or amount of ammonium bicarbonate. This knowledge allows the possibility of scaling up production of Nano $CaCO_3$ with significant reproducibility. This is crucial for being able to use $CaCO_3$ as a platform nanotechnology similar to gold or silver nanoparticles. Controlling size is critical for these studies to maximize the enhanced permeation and retention effect necessary for the accumulation of nanoparticles in tumors.[15] For instance, in the case of $CaCO_3$, we and others have demonstrated that 100 nm $CaCO_3$ has can neutralize extracellular acidic pH.[1-3,16] Smaller $CaCO_3$ particles could even be used to enter the intracellular space.

Stabilizing $CaCO_3$ in aqueous solutions remains a challenge. To tackle this question we evaluate a number of different solvents and their effect on $CaCO_3$ crystallinity and size over time. We discover that albumin is capable of maintaining particle size in aqueous solution, allowing further stability and *in vivo* applications.

By systematically evaluating variables involved in vacuum assisted $CaCO_3$ nanoparticle synthesis we have identified a model to design and produce a reproducible set of $CaCO_3$ particles of various sizes and yields. In the process, we have characterized a uniquely robust method of nanoparticle synthesis that is based on the aerosolization of a reagent under vacuum, in this case ammonium bicarbonate. By identifying albumin as a stabilizing medium, we open up nano-$CaCO_3$ for *in vivo* applications.

4.2 Materials and Methods

4.2.1 Synthesis of 100 nm nano-$CaCO_3$

We synthesized 100 nm $CaCO_3$ nanoparticles using a gas diffusion method. $CaCl_2$*$6H_2O$ (220 mg) was dissolved by vortexing in anhydrous ethanol (50 mL). The resulting solution was transferred to a 100 mL beaker covered with parafilm. After puncturing small holes in the parafilm, the beaker was placed in a desiccator (with drierite) surrounded by four 20 mL vials containing excess dry ammonium bicarbonate (~9-10 g). The entire system was placed under vacuum for 25 h. The particles were centrifuged at 6800 g for 10 min, excess ethanol decanted, and the residue was left to dry in open air before use.

4.2.2 Synthesis of 20 and 300 nm $CaCO_3$.

A double decomposition reaction was used to prepare the $CaCO_3$ particles by mixing 0.1 M each of $CaCl_2$*$2H_2O$ and $NaHCO_3$ at room temperature. The premix solutions of $CaCl_2$*$2H_2O$ and $NaHCO_3$ were prepared in water and polyethylene glycol (1:5 v/v; average molecular weight 1450 Da) for ~20 nm, and water and ethylene glycol (1:5 v/v; molecular weight 62.07 g/mol) for ~300 nm particles. The synthesized $CaCO_3$ particles were collected by sequentially washing the product with ethanol, methanol and acetone, followed by drying at 60 °C for 1 h. (Figure 4.1)

4.2.3 Modified Synthesis of $CaCO_3$

$CaCl_2$ Hexahydrate (Sigma Aldrich) was dissolved in a volume of anhydrous ethanol as described above, and placed in a 400 mL beaker in a dessicator (with drierite), surrounded by 20 mL glass vials filled with ammonium bicarbonate of a controlled mass (typically 20 g per vial) and placed under vacuum for 1- 3 days. The specific days, volume, mass, or surface area are as described below. (Figure 4.1)

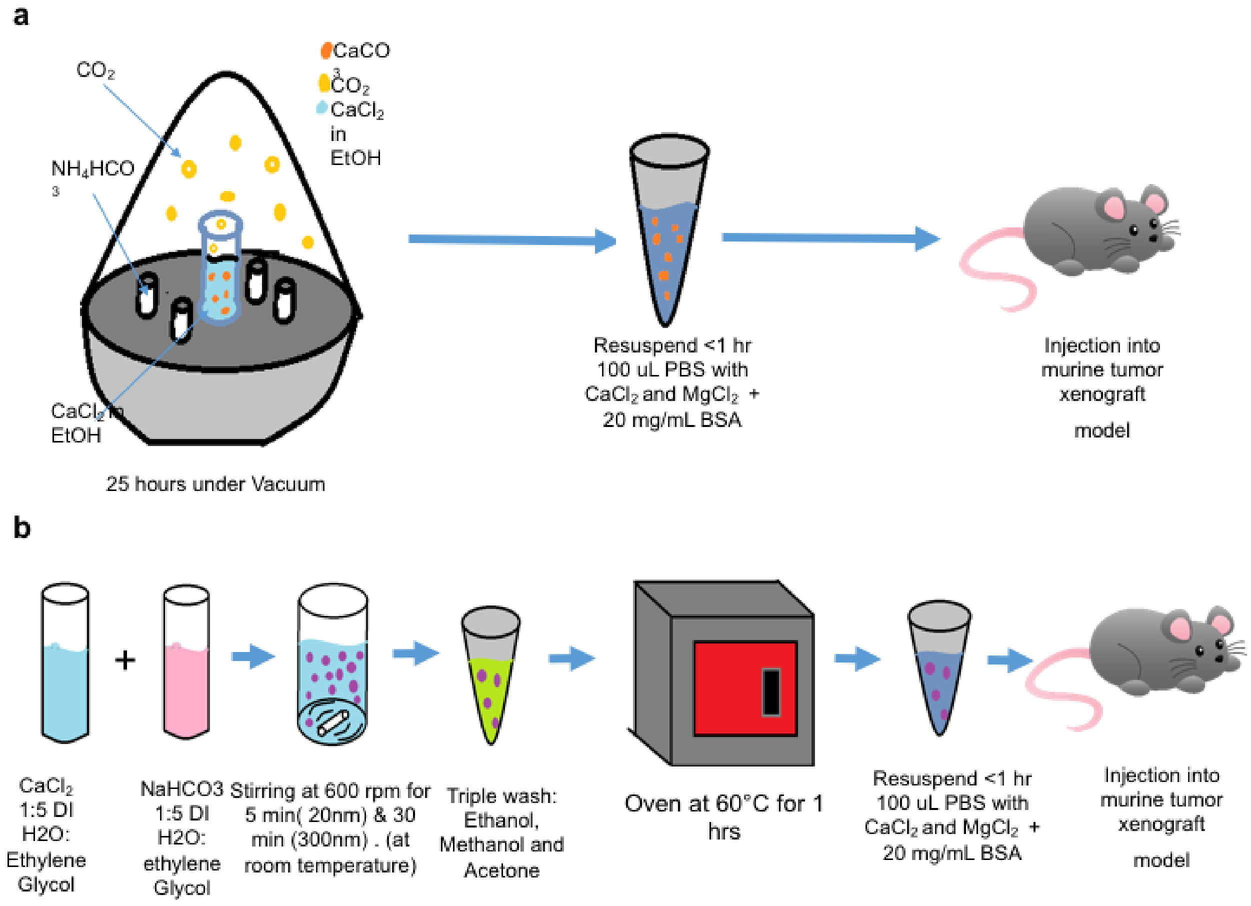

Figure 4.1. Synthesis and Experimental Schema for nano-$CaCO_3$ synthesis. (a) Synthesis schema for the gas diffusion method for nano-$CaCO_3$ synthesis. (b) Synthesis schema for synthesis of nano-$CaCO_3$ using sol-gel. Both methods can be used to make 20 nm, 100 nm, and 300 nm particles. Synthesis was followed by suspension in an aqueous solvent followed by in vivo experiments in murine models.

4.2.7 Synthesis of $AuCO_3$, $ZnCO_3$, $FeCO_3$

140-200 mg of $AuCl_3$, $FeCl_3$, and $ZnCl_2$ (Sigma Aldrich) was dissolved in 50 mL of anhydrous ethanol as described below, and placed in a 400 mL beaker in a desiccator (with drierite), surrounded by 20 mL glass vials filled with ammonium bicarbonate of a controlled mass (typically 20 g per vial) and placed under vacuum for 2 days.

4.2.8 Transmission Electron Microscope (TEM).

TEM micrographs were obtained using a FEI Spirit TEM (Hillsboro, USA) operated at 120 kV. A 400-mesh Formvar® carbon-coated copper grid was glow-discharged in a vacuum evaporator (Denton, Moorestown, New Jersey) for 30 s. The sample was prepared by placing 2 μL of sonicated $CaCO_3$ nanoparticles solution onto the grid and wicking off the excess sample with filter paper after 30 s. Alternatively, for EtOH or DMSO solvent based solutions, 3 $\boldsymbol{\mu}$L of particle solution were placed on the grid and left to dry out at room temperature or with the aid of a heat gun.

4.2.9 X-Ray Diffraction (XRD).

XRD patterns were obtained by using the Bruker d8 Advance X-ray Diffractometer (Bruker, USA) configured with a Cu X-Ray tube with 1.5418 Å for analysis of powder samples using LYNXEYE_XE detector. For the analysis, fine acetone ground $CaCO_3$ nanoparticles were kept on a Zero Diffraction Plate (MTI Corporation, USA). XRD data were scanned from 20-60 degrees, with a 0.04 degree step size, a 0.5 s per step count time, with sample rotation turned on (15 rotations per min), with a coupled two-theta/theta scan. The Bruker Diffrac.Eva program was used for the evaluation and processing of X-ray diffraction scan data. Search-match operations included search by DI list, by name, using chemistry filters, and creating an International Centre for Diffraction Data (ICCDD PDF) database filter.

4.2.10 Hydrodynamic diameter and electro-kinetic zeta potential.

To study agglomeration kinetics of $CaCO_3$ nanoparticles, hydrodynamic diameter (*Dh*) was measured using DLS (Malvern Instruments, Southborough, Massachusetts). Agglomeration kinetics were measured on the basis of data obtained from TR-DLS.

The zeta potential was measured using a Malvern Zetasizer Nano ZS instrument. An applied voltage of 100 V was used for the nanoparticles. A minimum of three measurements were made per sample.

4.2.11 Identification of stable aqueous medium for nano-$CaCO_3$.

Nano-$CaCO_3$ was resuspended in the following solvents: (1) dIH_2O; (2) Dulbecco's PBS, (3) PBS, 1 mM $CaCl_2$, and 1 mM $MgCl_2$; (4) PBS, $CaCl_2$, $MgCl_2$ and 2% bovine serum albumin; (5) fetal bovine serum (FBS); and (6) a solution consisting of 20% (PBS, $CaCl_2$, $MgCl_2$, and 2% bovine serum albumin) in 80% FBS. The results of particle stability were analyzed by TR-DLS for up to 7 h, TEM under aqueous conditions, TEM under serum, and XRD after 7 h.

4.2.12 Yield measurement

Yield was determined by centrifuging 10 mL of particle ethanol solution at 6800 x g for 10 minutes into Eppendorf tubes and air dried. Mass was measured before and after of the tube, giving the concentration per 10 mL which was multiplied by the volume of solution remaining.

4.3 Results

4.3.1 Independent facile synthetic methods produce pure vaterite nanoparticles with controlled size range from 20 – 300 nm

The malformation of blood and drainage vessels around solid tumors creates an environment for the selective retention of nanoparticles through the enhanced permeation and retention (EPR) effect.[15] Typically, materials with core diameters less than 500 nm are preferred to enhance intravascular dynamics and diffusion to tumor cells further from the blood vessels.[15,17]

Unfortunately, $CaCO_3$ nanoparticles that are stable in aqueous solutions have been difficult to synthesize at sub-micron sizes without the use of harsh conditions (custom high pressure systems), doping materials (lipid-based surfactants), other additives such as phosphate, polystyrene, and drugs, or a combination of calcium phosphate and calcium carbonate.[1,2,4,7,18] Attempts to prepare pure nano-$CaCO_3$ have generally resulted in the production of materials with core diameter > 500 nm[3,5,9] due to difficulty in controlling the particle's growth. Furthermore, $CaCO_3$ nanoparticles can rapidly grow to larger crystalline polymorphs (calcite, vaterite, or aragonite) when placed under aqueous conditions via a variety of mechanisms.[8,12-14,19]

Building on literature methods, we have identified two independent methods to produce pristine sub-micron vaterite nano-$CaCO_3$ with distinct size ranges at 20 nm, 100 nm, and 300 nm. Synthesis of the 100 nm nano-$CaCO_3$ was accomplished by using a gas diffusion method (Figure 4.1, Methods section).[14] The stepwise approach of exposing calcium chloride in anhydrous ethanol to controlled amounts of ammonium bicarbonate, followed by gradual air drying of the product, afforded a simple and highly reproducible method to prepare these nanoparticles. To provide flexibility in particle size, we used a double decomposition reaction method between hydrated calcium chloride and sodium bicarbonate at room temperature. Size control was achieved by mixing the reactants in a mixture of solvents consisting of 1:5 ratio of water/polyethylene glycol (20 nm) and water/ethylene glycol (300 nm). The ethylene glycol and polyethylene glycol were used to modulate the diffusion rate of calcium and carbonate ions, thereby controlling nucleation and growth by particle cluster formation.[20,21] This approach revealed that solvent viscosity can serve as a modular strategy to prepare pure vaterite nanoparticles.

The size and morphology of synthesized nano-$CaCO_3$ were determined by transmission electron microscopy (TEM) and dynamic light scattering (DLS) (Figure 4.2). Typical TEM micrographs revealed that nano-$CaCO_3$ were primarily spherical, as expected for vaterite. The geometric mean diameters of the nano-$CaCO_3$ were 20 ± 1.4 nm, 100 ± 8.3 nm and 300 ± 14.6 nm (Figure 4.2a-c). Expectedly, DLS revealed a slight increase in the hydrodynamic diameter (*Dh*) for all particle sizes because of the interaction of solvent molecules with the surface of particles, creating a thin layer of solvent molecules (Figure 2d).

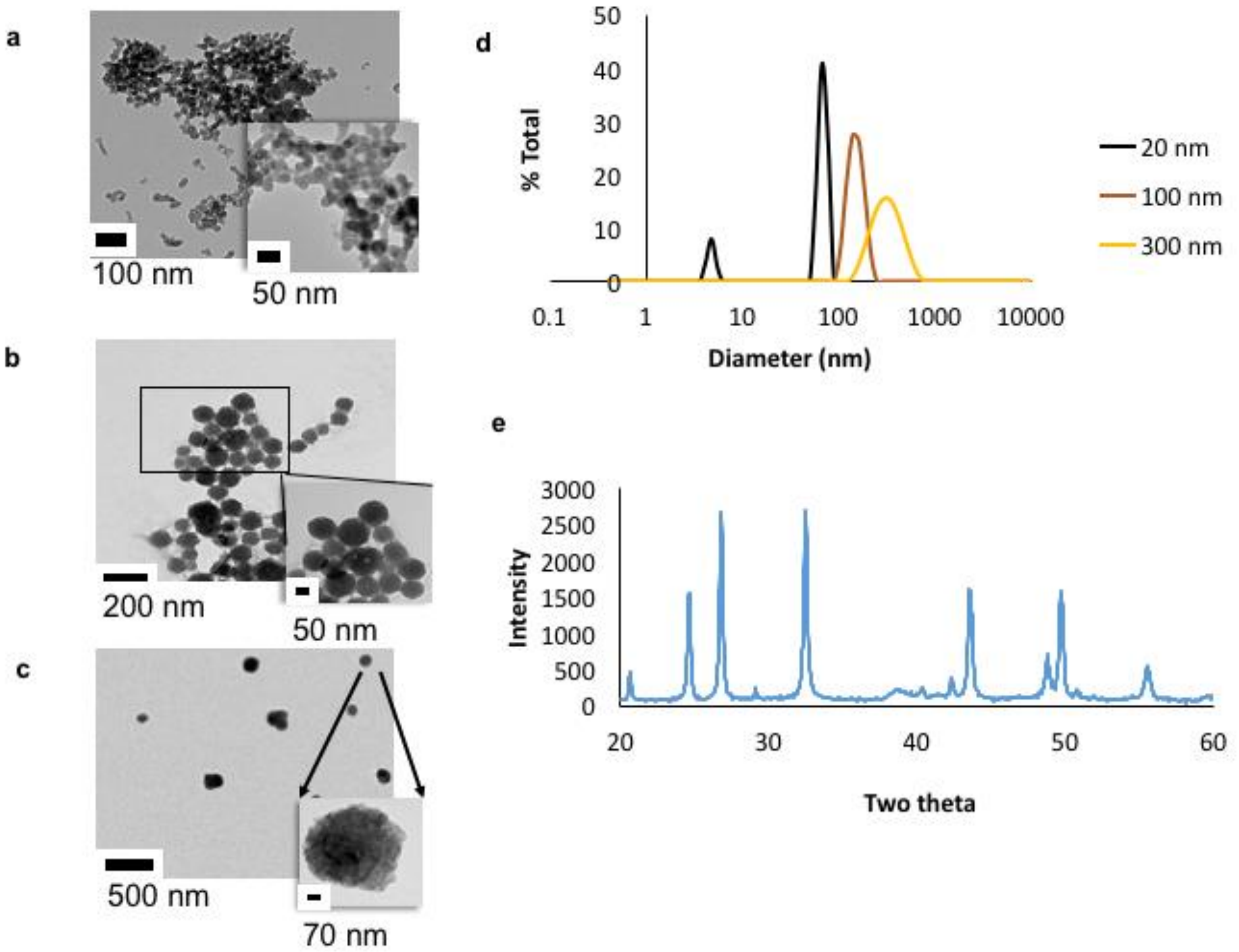

Fig. 4.2 Independent facile synthesis methods can produce nano-$CaCO_3$ at various sizes. (a) TEM of 20 nm vaterite demonstrates rod like particles with a tendency for aggregation. (b) TEM of 100 nm vaterite shows spherical particles. (c) TEM for 300 nm vaterite demonstrates larger spherical particles. (d) DLS results in ethanol for the 3 particle sizes replicates TEM findings. (e) XRD of 100 nm $CaCO_3$ demonstrates vaterite signature.

However, two peaks were observed in the DLS profile of the 20 nm nanoparticles, in which one peak exhibited smaller *Dh* than the physical diameter. These peaks could arise from the asymmetric shape of the particles, as shown in the 20 nm particles (Figure 4.2a).[22] Larger sizes were typically spherical, accounting for the lack of a second smaller peak. Irrespective of the synthesis method, all three sizes of the nano-$CaCO_3$ showed peaks at theta angles of 24.8, 27.1, 32.8 and 43.9, which are consistent with the characteristic hexagonal vaterite crystalline structure of $CaCO_3$ (Figure 4.2e & Figure 4.3). Because vaterite is more soluble in aqueous media than other $CaCO_3$ polymorphs, these materials are suitable for use in neutralizing the acidic pHe of tumors if they can remain stable in aqueous environments without rapidly converting to the less soluble calcite.

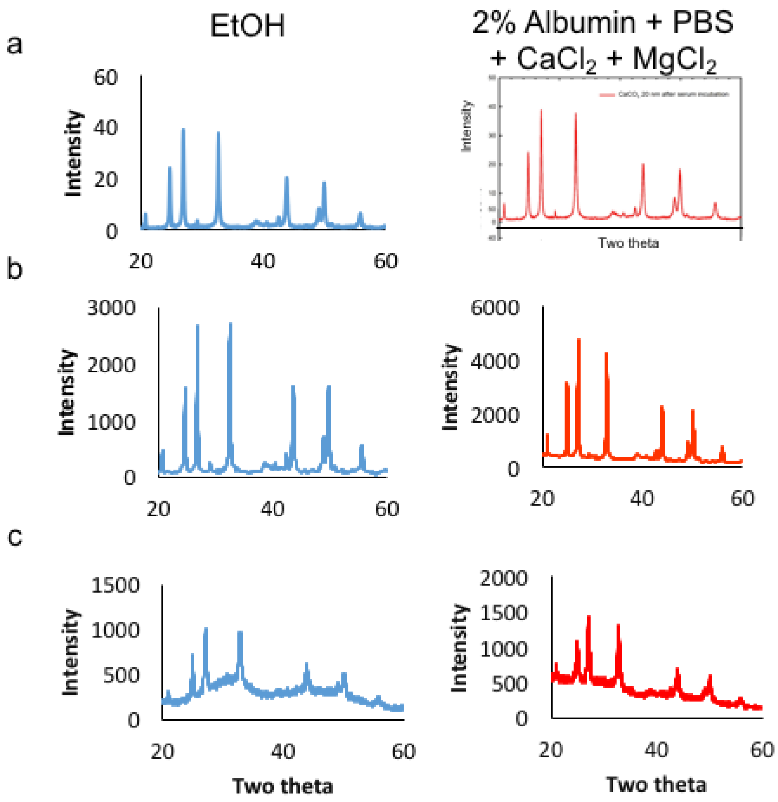

Figure 4.3. X-Ray diffraction post addition of albumin based solvent shows stability in all three sizes of particles. (a) XRD of 20 nm nano-$CaCO_3$ is identical in EtOH and in 2% albumin + PBS + $CaCl_2$ + $MgCl_2$ solution. (b) XRD of 100 nm nano-$CaCO_3$ is identical in EtOH and in 2% albumin + PBS + $CaCl_2$ + $MgCl_2$ solution. (c) XRD of 200 nm nano-$CaCO_3$ is identical in EtOH and in 2% albumin + PBS + $CaCl_2$ + $MgCl_2$ solution. All plots, when compared to literature, match the structure of vaterite.

4.3.2 Albumin prevents rapid conversion of vaterite nanoparticles to calcite or calcium phosphate in aqueous medium and serum

The solubility and stability of these vaterite nanoparticles are critical for successful biological applications in vivo. We explored a variety of biologically compatible media to identify the optimal storage conditions and vector for intravenous (I.V.) administration of the nano-$CaCO_3$ (Figure 4.4; Figure 4.5). DLS analysis shows a rapid increase of the 100 nm vaterite nanoparticles from 100 nm to over 500 nm within a few seconds in saline and in phosphate buffered saline (PBS; Figure 4.4a). The observed morphological change in PBS could be attributed to calcite or $CaPO_4$ formation. However, addition of 2% albumin to PBS remarkably stabilized the materials for extended periods, demonstrating the potential of formulating vaterite nanoparticles in this medium for I.V. administration (Figure 4.4a,b). A similar trend was observed with the 20 nm and 300 nm nano-$CaCO_3$ (Figure 4.6).

We further determined the long-term particle stability in different media for up to 7 h. Time-resolved DLS (TR-DLS) suggests that the particles in aqueous albumin containing solution exist in pairs of 2 or 3 (size 2-3 times larger than in ethanol), which dissociate into individual particles upon exposure to fetal serum (Figure 4.4a, Figure 4.6). TEM confirmed the high stability of the particles in albumin solution (Figure 4.4b, Figure 4.6). X-Ray Diffraction (XRD) analysis did not show any change in crystallinity in albumin-based aqueous media (Figure 4.4c). The nano-$CaCO_3$ exhibited stability in both morphology and size in fetal bovine serum (Figure 4,4d, Figure 4.6).

These results suggest that albumin, which has a high affinity for calcium,[23] serves as a calcium sink that prevents aggregation and calcium phosphate formation in PBS. The minimal change in TEM (structural) and X-ray diffraction (crystalline) analyses confirms that extensive double replacement to form $CaPO_4$ did not occur. In general, clusters of three nano-$CaCO_3$ form in albumin solutions, which separate into single particle serum is added to the mixture. The additional serum stability conferred on nano-$CaCO_3$ in aqueous albumin solution indicates that pre-formulation of the nanoparticles in this medium is ideal for in vivo application, where serum is abundant.

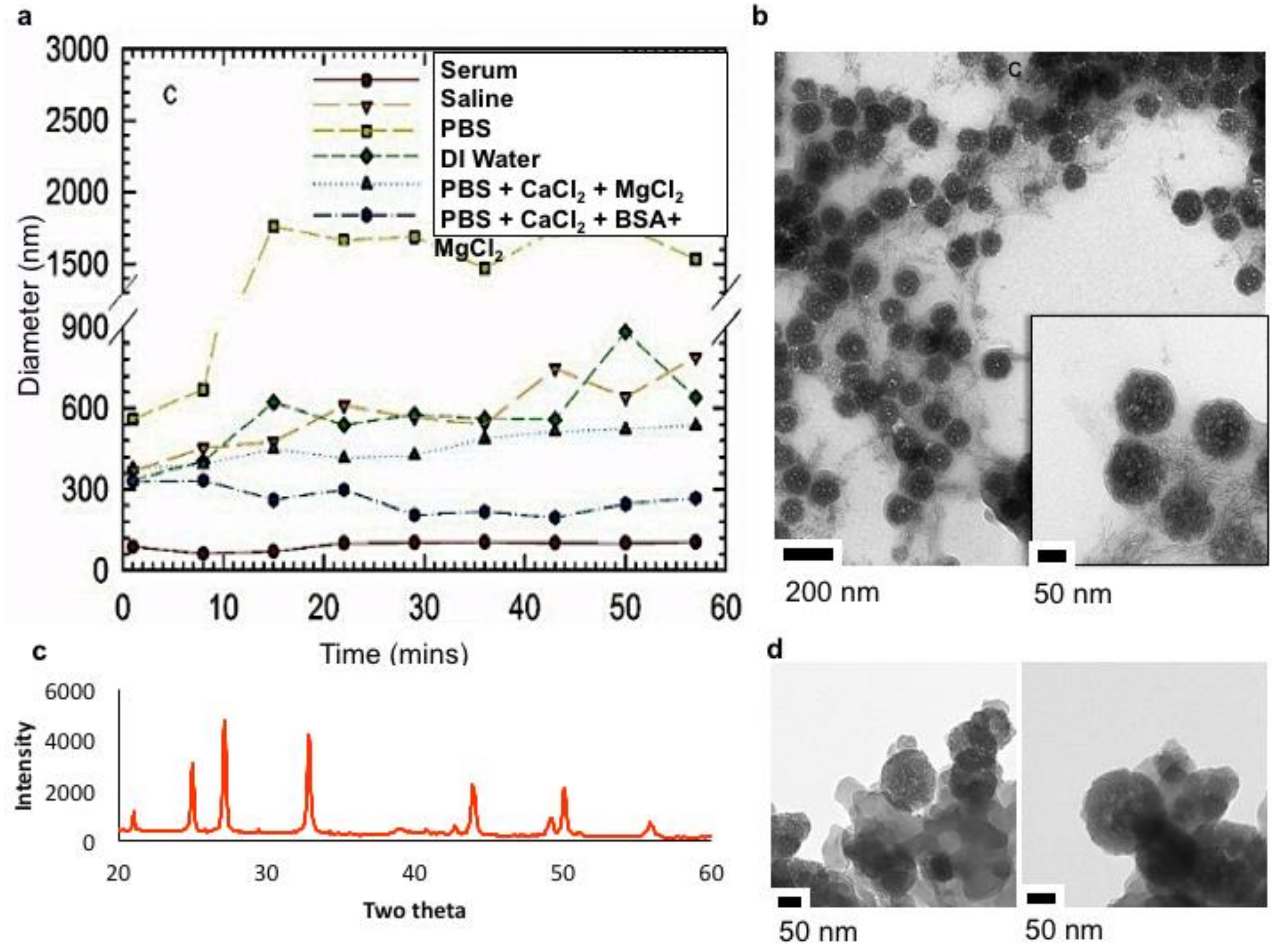

Fig. 4.4 Nano-$CaCO_3$ is stabilized in an albumin based solution. (a) DLS results of 100 nm particles show that stability in serum > PBS+BSA+$CaCl_2$ > PBS+$CaCl_2$ > Saline = DI Water > PBS. (b) TEM shows 100 nm particles in albumin solution have unchanged morphology surrounded by albumin. (c) XRD of 100 nm particles in albumin solution at 24 h shows no changes in crystalline structure. (d) TEM of particles post serum incubation demonstrate no change in structure, with particles embedded in serum protein.

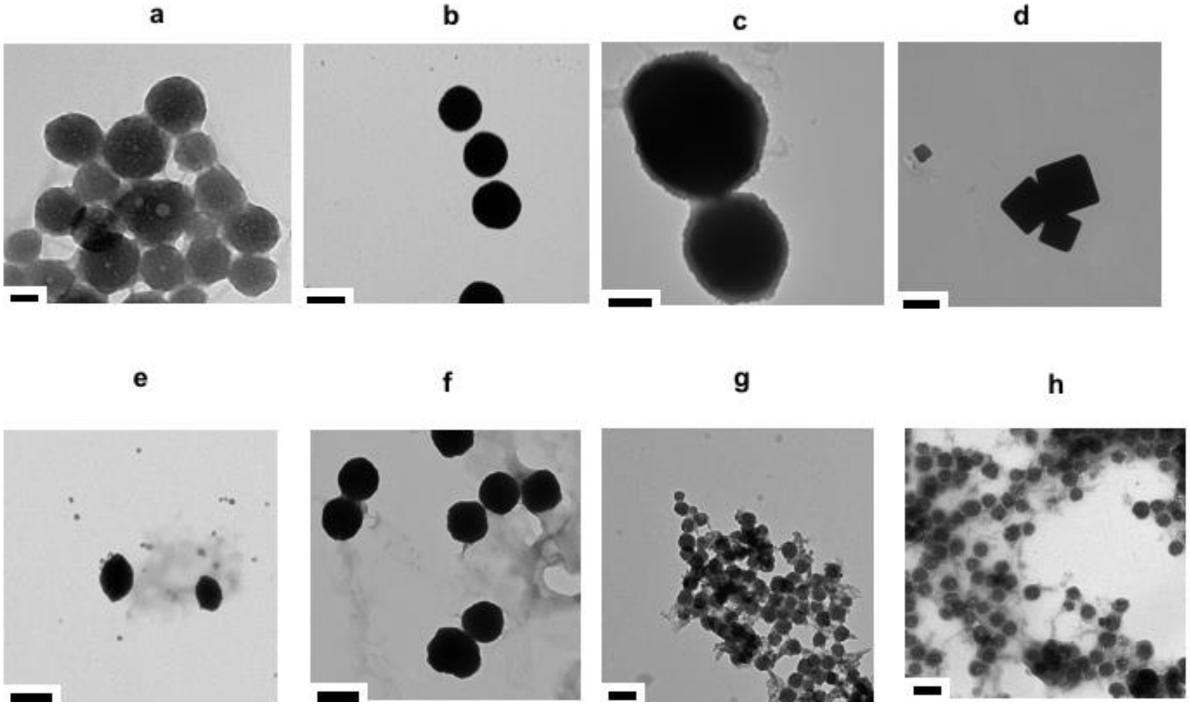

Figure 4.5 $CaCO_3$ grows in size in a variety of solvent incubations for 100 nm nano-$CaCO_3$ except albumin containing solutions. (a), At synthesis, particles are monodisperse and 100 nm in size. Scale bar represents 50 nm. (b), When placed into deionized H_2O, particles rapidly grow to be > 1 μm. Scale bar is 1 μm. (c), When 100 nm nano-$CaCO_3$ is placed into 15 mM saline, particles grow to greater the > 1 μm. Scale is 1 μm. (d), When placed into PBS, particles become cuboidal in shape and large. Scale bar is 1 μm. (e), Coating particles with a hydrophobic coating using Poly-Vinyl Pyrrolidone (PVP), slows reaction and makes growth slightly slow. Scale bar is 0.5 μm. (f), Coating particles with a hydrophobic coating using Poly-2-Vinyl Pyrrolidone (PVP), slows reaction and makes growth slightly slow. Scale bar is 0.5 μm. (g), Adding $CaCl_2$ and $MgCl_2$ to the PBS solution slows $CaCO_3$ growth, with some reaction appearing to occur. Scale is 200 nm. (h), Adding 2% albumin to a solvent of PBS + $CaCl_2$ + $MgCl_2$ preserves particle morphology.

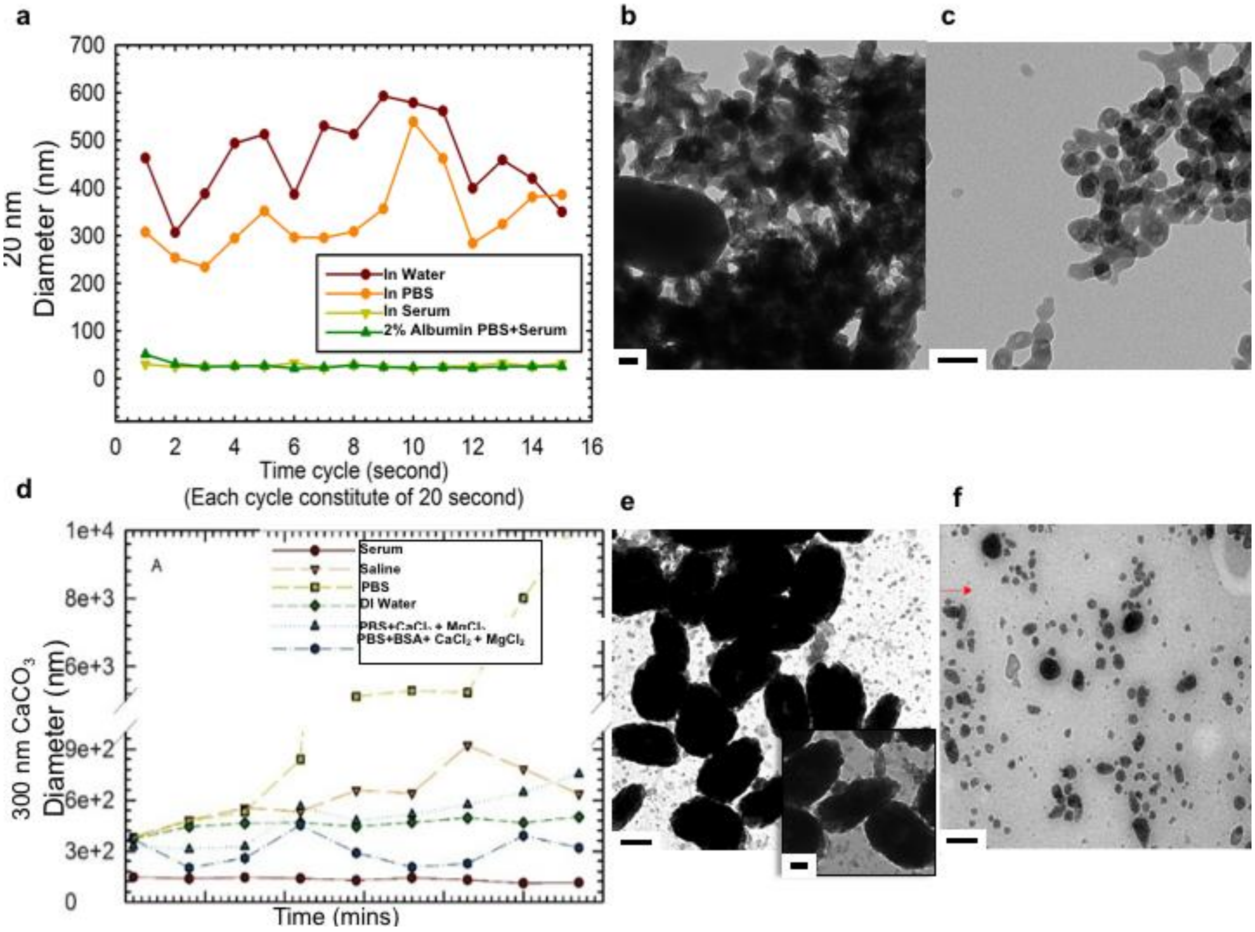

Figure 4.6. 20 nm and 300 nm particles show stability in albumin containing solution and in serum. (a) DLS results over time in a variety of aqueous solvents for 20 nm particles demonstrates that particles on addition to serum separate from an aggregate in 2% albumin. (b), TEM of 20 nm particles in PBS + $CaCl_2$ + $MgCl_2$ + 2% albumin shows separation . Scale bar is 200 nm. (c), TEM of 20 nm particles post serum incubation shows retention of morphology. (d), DLS results over time in a variety of aqueous solvents for 300 nm particles show the same trend as 20 nm and 100 nm particles in solvent stability. (e), 300 nm particles under 2% albumin + PBS show some slight increase in size. Scale bar for large image is 200 nm. Scale bar for magnified image is 100 nm. (f), 300 nm particles in serum show retention of shape and morphology. Scale bar is 200 nm.

Synthesis of $CaCO_3$ nanoparticles via the vacuum assisted method occurs in a solution of $CaCl_2$ hexahydrate in EtOH placed in a beaker covered by a parafilm with small holes punctured through (Figure 4.7). Ammonium bicarbonate is placed in small uncapped vials surrounding the beaker, usually 10 – 20 g of ammonium bicarbonate per vial (Figure 4.7). Both of these reagents are placed in a dessicator including drierite, and placed under continuous house vacuum for 24 to 48 hours (Figure 4.7).

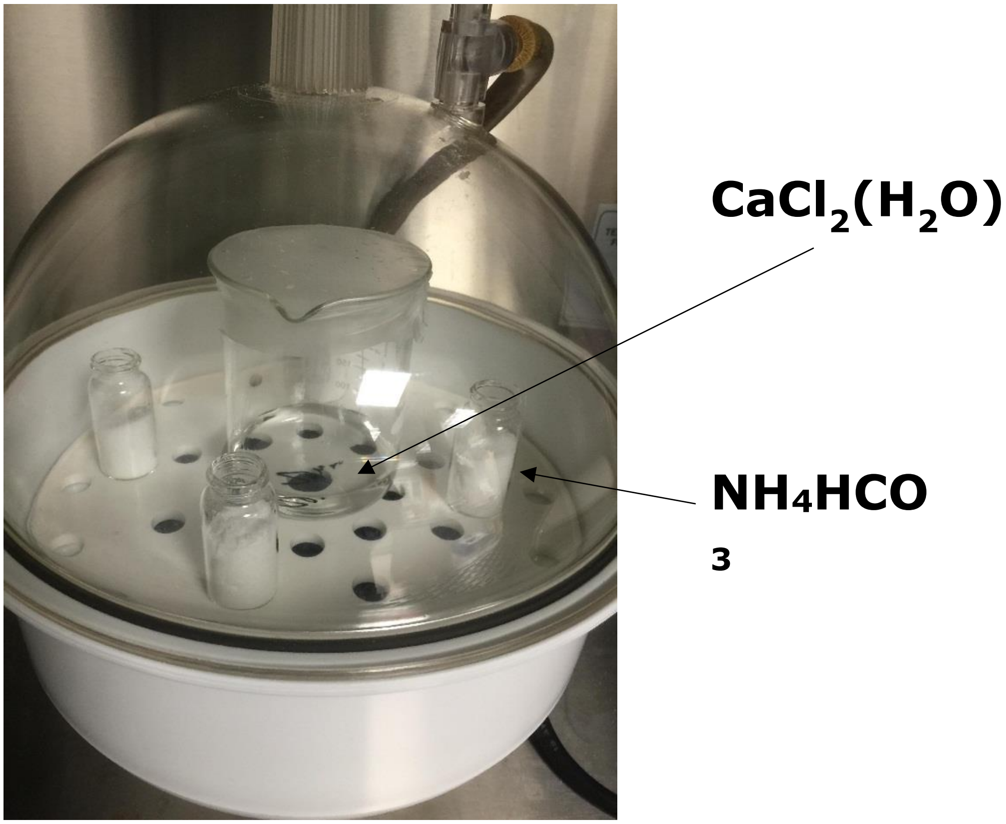

(a)

Figure 4.7. (a) Synthesis contraption. Solid ammonium bicarbonate is placed around $CaCl_2$ hexahydrate over varying periods of time in order to synthesize vaterite based $CaCO_3$ nanoparticles.

We then further determined how to make this synthesis process more efficient by exploring both the variables and the mechanism behind this method. We considered the following variables towards identifying efficient $CaCO_3$ synthesis, including time under vacuum, concentration of $CaCl_2$, volume of solution, exposed surface area of $CaCl_2$ solution, surface area of ammonium bicarbonate, amount of ammonium bicarbonate, number of runs, and amount of water in the EtOH solvent. Temperature was held at room temperature, the desiccator size was 11.5” in diameter, and vacuum pressure was kept at maximum house vacuum.

$CaCO_3$ has a thermodynamic equilibrium point at > 1 μm in aqueous solution. Because we consistently see 100 nm particles, we focused on kinetic or other constraints on size. In particular, we hypothesized three possibilities for the mechanism constraining size in particle formation: one, a nucleation event of $CaCO_3$ that then grows with repeated deposition; two, $CaCl_2$ hexahydrate forms size constrained small water droplets in the EtOH; or three, aerosolization of ammonium bicarbonate under vacuum creates size constrained particles.

4.3.3 $CaCO_3$ particles do not grow from repeated layer by layer deposition in ethanol assisted synthesis.

To test the first hypothesis, we investigated the change in the size of the nanoparticles over time under synthesis. We hypothesized that $CaCO_3$ deposition could occur by the initial aerosolizing ammonium bicarbonate to form a nucleating event that then grew with additional ammonium bicarbonate depositing over time, similar to processes seen in gold or silver nanoparticles and in more classical water based synthesis techniques for $CaCO_3$.[1,24] In this case, we expect that each $CaCO_3$ particle itself would grow in size with increasing time under the reaction. If not true, we would expect that the number of particles would change but not the size, i.e. changing yield independent of size. We approached this question by testing the yield and size distribution of $CaCO_3$ after different amounts of time under vacuum.

We find that nano-$CaCO_3$ synthesis occurs very quickly after starting vacuum flow. However, we found that it took approximately 24 hours to synthesize quantities useful for animal experiments, and as such we used this time point as an initial baseline. When comparing the yield at 24 hours versus 72 hours, we find a 10 fold increase in yield (Figure 4.8a). In comparison, increasing the volume of $CaCl_2$ solutions by four fold only increased the yield by 1.4x (Figure 4.8a). In addition, via TEM, we find that there are no changes in the size of the particles with the increase in time, suggesting a non-layering synthesis mechanism (comparing Figure 4.8b and 4.8c). The increase in yield does evidently have a tradeoff with aggregation, with a larger degree of clumping of individual particles with larger amounts of time, but no merging of the particles (Figure 4.8c). The lack of crystal fusion in the clumps adds further evidence against the possibility of a nucleation and growth mechanism.

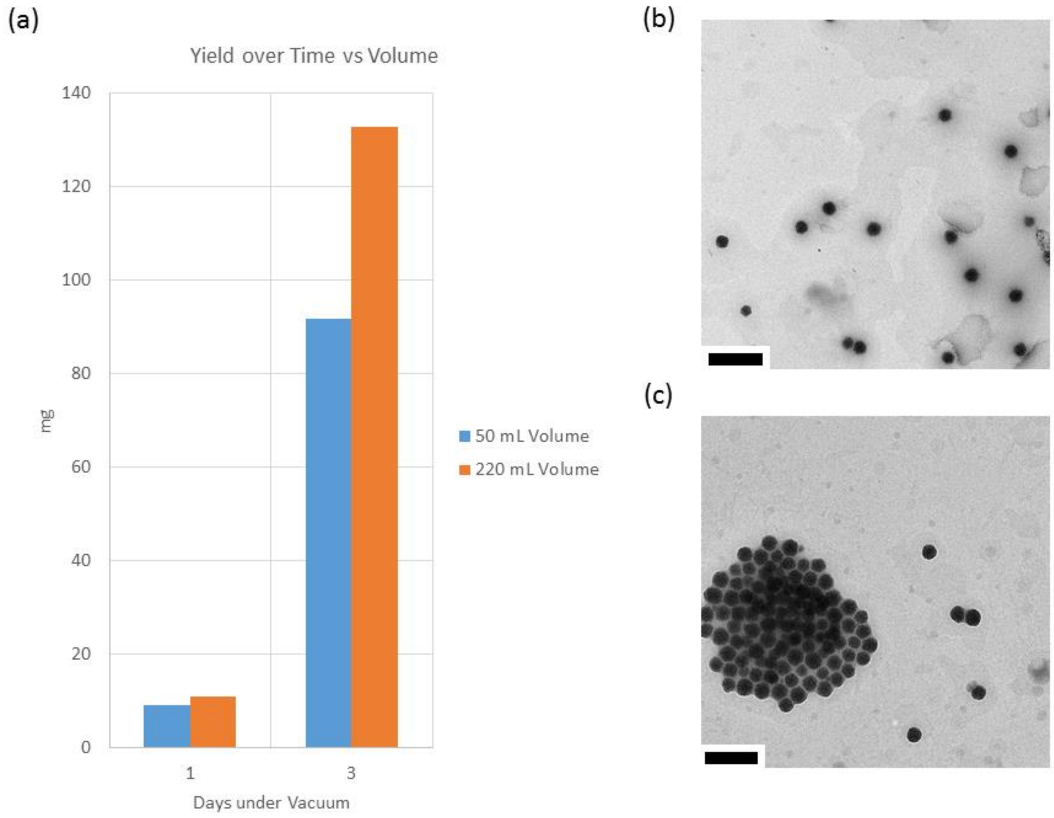

Figure 4.8. (a) Yield increases with number of days substantially, and volume by a minor part. (b) TEM of particles after 24 hours (50 mL volume, 4 mg/mL $CaCl_2(H_2O)_6$ concentration, 4 vials), scale bar 500 nm. (c) TEM of particles after 38 hours (50 mL volume, 4.4 mg/mL $CaCl_2(H_2O)_6$ concentration, 4 vials), scale bar 500 nm.

4.3.4 $CaCO_3$ size is not influenced by the amount or state of $CaCl_2(H_2O)_6$ in the EtOH solution

In our second theory, if $CaCl_2$ hexahydrate was to form micellar-like size constrained droplets in the EtOH solution, we would expect the particle size to be dependent on the concentration of $CaCl_2$ hexahydrate or other factors of the solution itself. Micelle size is typically controlled by the ratio of aqueous to non-aqueous solution and surfactant concentration. We investigated whether any micellar-like phenomenon was occurring here by varying the concentration of $CaCl_2$ in solution, the surface area of exposure, and the volume of solution, and assessing the resulting size of particles via TEM. If true, we would expect that the putative nano-droplets of $CaCl_2$ hexahydrate would be directly related to these factors.

As such, we tested $CaCO_3$ synthesis at different concentrations, volumes and surface areas of solutions. We find that the concentration of $CaCl_2$ hexahydrate in EtOH does not affect size of the resulting particles when controlling for surface area and volume (comparing Figure 4.9a and 4.9b). Going further, we tested changing surface area while controlling volume, and we find no change in average particle size (comparing Figure 4.9c and 4.9d). When we test changes in the absolute amount by changing volume we also find no change in size (comparing Figure 4.9e and 4.9f). These results conclude that the size of the particle is not restricted by amount or concentration of the $CaCl_2$ hexahydrate EtOH solution.

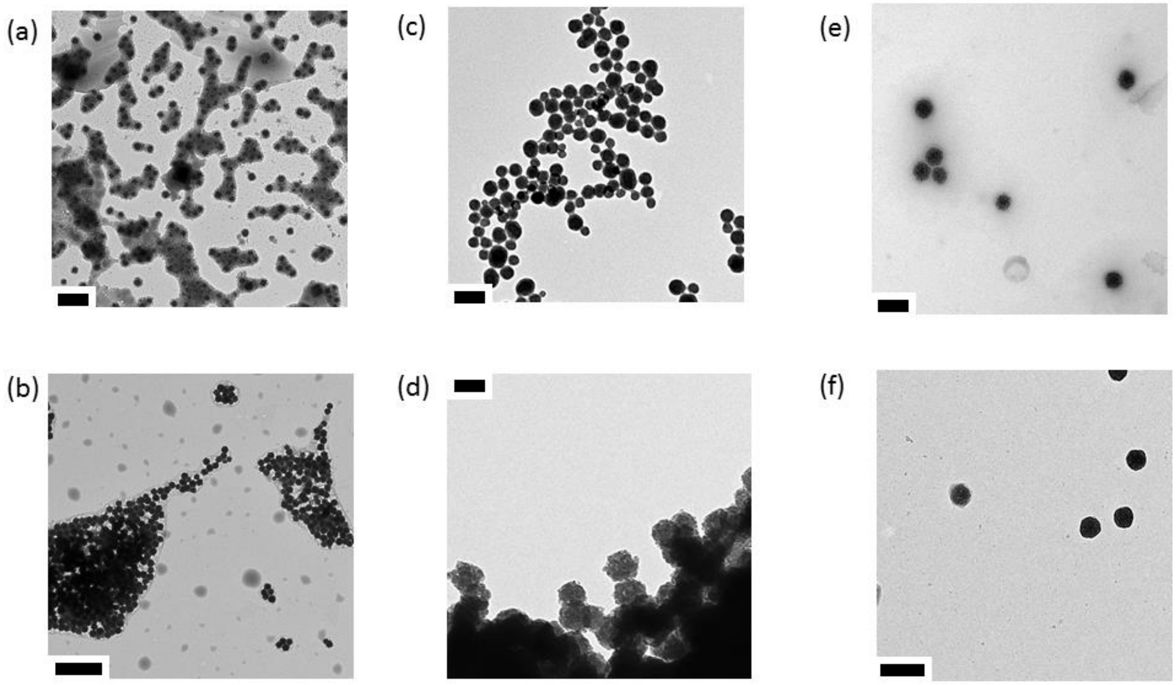

Figure 4.9. $CaCl_2(H_2O)_6$ solution has no effect on size. (a) TEM of particles made under **4.4 mg/mL $CaCl_2(H_2O)_6$,** with 4 vials ammonium bicarbonate, in 50 mL over 3 days in a 77 mm diameter beaker, scale bar is 500 nm. (b) TEM of particles made under **16 mg/mL $CaCl_2(H_2O)_6$** with 4 vials ammonium bicarbonate in 50 mL volume over 3 days in a 77 mm diameter, scale bar is 1 μm. (c) TEM of particles made in a 4.4 mg/ mL $CaCl_2(H_2O)_6$ concentration in 50 mL volume, in a **68 mm diameter flask** for 1 day, scale bar is 200 nm. (d) TEM of particles made in a 2.8 mg/mL $CaCl_2(H_2O)_6$ concentration in a 50 mL volume with **77 mm diameter** over 2 days, scale bar is 100 nm.(e) Particles made in a 4.4 mg/mL $CaCl_2(H_2O)_6$ concentration with 4 vials in 68 mm diameter, with **50 mL volume** over 1 day, scale bar is 200 nm. (f) 4.4 mg/mL $CaCl_2(H_2O)_6$ 4 vials 77 mm diameter in **223 mL volume** over 3 days, scale bar is 200 nm.

4.3.5 Synthesis is dependent on the aerosolization of ammonium bicarbonate for changes in size and yield

Given the above results, we tested the third hypothesis that synthesis is dependent on the aerosolization process of ammonium bicarbonate under vacuum. The original reports of the method did not report the amount of ammonium bicarbonate used, and generally kept the amount in large excess compared to the concentration of $CaCl_2$ hexahydrate. If it is dependent on ammonium bicarbonate then we would expect that the size would change based on changes in ammonium bicarbonate, such as amount, age, or number of runs.

Because of the nature of the synthesis reaction, during experimentation, it is possible to retain the approximately same mass of ammonium bicarbonate experiment after experiment due to its solid state. In all of the experiments seen in Figure 4.10, the number of vials of ammonium bicarbonate ~ 20 g per vial remained constant at 15 vials unless noted otherwise. Per experimental run, we find that size and yield decreases (compare Figure 4.10a to 4.10b and 4.10c, Figure 4.11). We postulate that this effect is due to decreasing amounts of ammonium bicarbonate aerosolizing and smaller crystals aerosalizing during each experimental run. Indeed, this effect aligns directly with the age of the ammonium bicarbonate reducing the yield and size of particles (Figure 4.11a, c, d). Combining an old series of vials with a new vial results in a mixed batch of particles, including both smaller and larger particles, suggesting particle is based purely on the ammonium bicarbonate at the solid to gas interface and not forming in transit to the gas-liquid interface (Figure 4.11b).

We were able to replicate this effect by reducing the absolute amount of ammonium bicarbonate below the point of excess. When testing synthesis with a 1:1 or 1:2 ratio of ammonium bicarbonate and $CaCl_2$ hexahydrate, we find a significantly smaller diameter particle adding credence to this hypothesis (compare Figure 4d to 4f). However, it is clear that the size appears to plateau at 100 nm quickly above the 1:1 point.

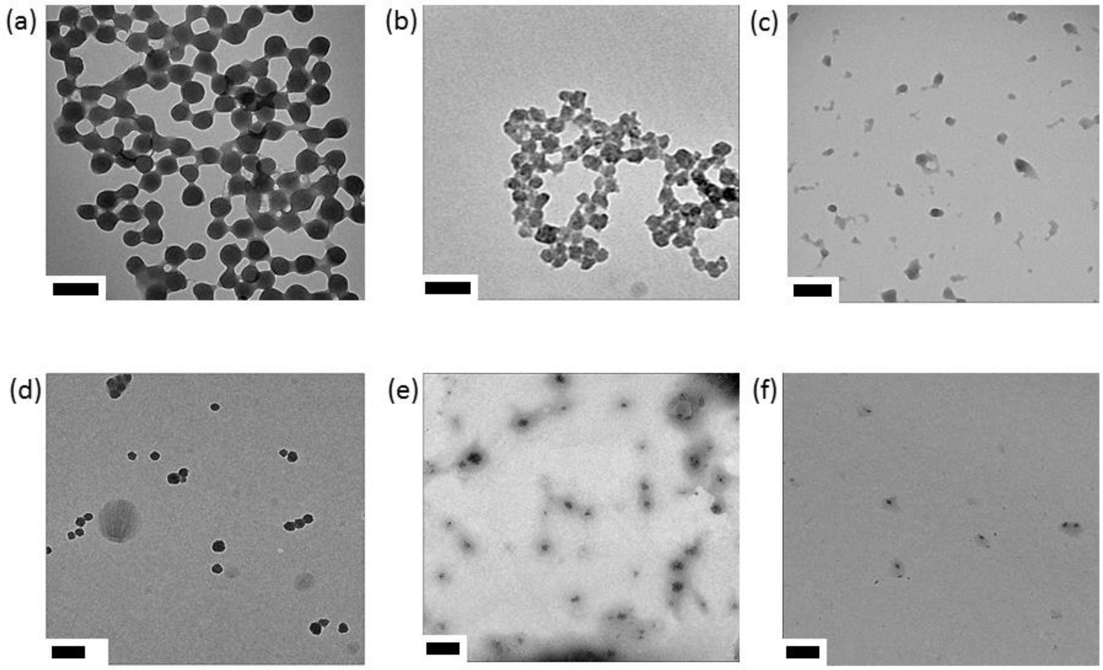

Figure 4.10. Ammonium bicarbonate has an effect on size (a) TEM images of particles on the **first run** of 300 g ammonium bicarbonate over two days, scale bar is 200 nm. (b) TEM images of particles on the approximately **third run,** at approximately the same mass of ammonium bicarbonate over two days, scale bar is 100 nm. (c) TEM images of particles on the approximately **fifth run**, at approximately the same mass of ammonium bicarbonate over two days, scale bar is 100 nm. (d) TEM images of particles on the first run using **127 mg of**

ammonium bicarbonate, over two days, scale bar is 200 nm. (e) TEM images of particles on the first run using **57 mg of ammonium bicarbonate**, over two days, scale bar is 200 nm. (f) TEM images of particles on the first run using **7.9 mg ammonium bicarbonate**, over two days, scale bar is 200 nm.

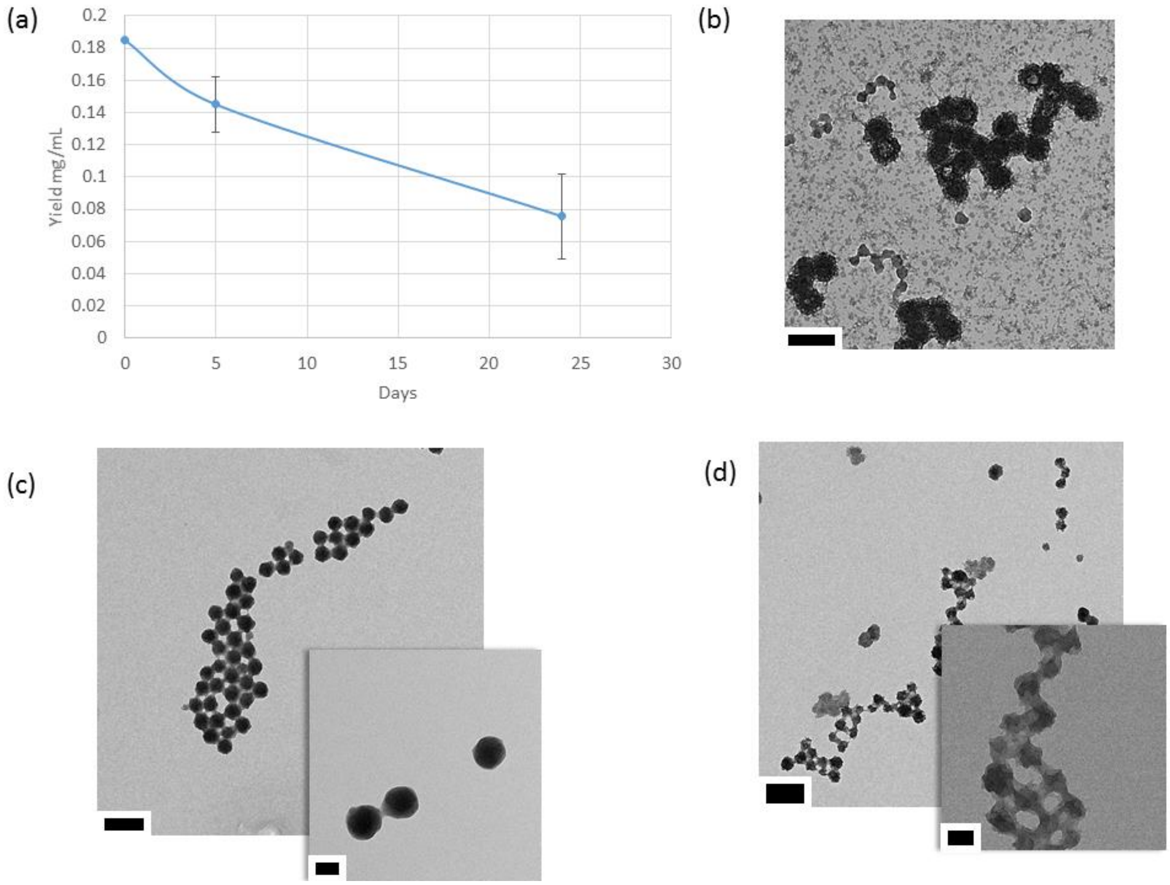

Figure 4.11. Particle size and yield is dependent on the age of ammonium bicarbonate. a) Yield over time via aging of ammonium bicarbonate over runs b) TEM of synthesis using a mix of new and old NH_4CO_3, scale bar is 200 nm c) TEM of synthesis using 2 months old NH_4CO_3, scale bar is 200 nm, subset, scale bar is 50 nm d) TEM of synthesis using over 6 month old ammonium bicarbonate, scale bar is 200 nm, subset, scale bar is 50 nm.

The surface area of ammonium bicarbonate, in general, did not change the size (compare Figure 4.12a vs 4.12b). However when placing a large amount of ammonium bicarbonate in a 400 mL beaker, a relatively low surface area to mass, we find large fused aggregates / microparticle formation (Figure 4.12c). Reducing the amount of ammonium bicarbonate or increasing the surface area was able to correct for the aggregation effect (Figure 4.12b, 4.12d).

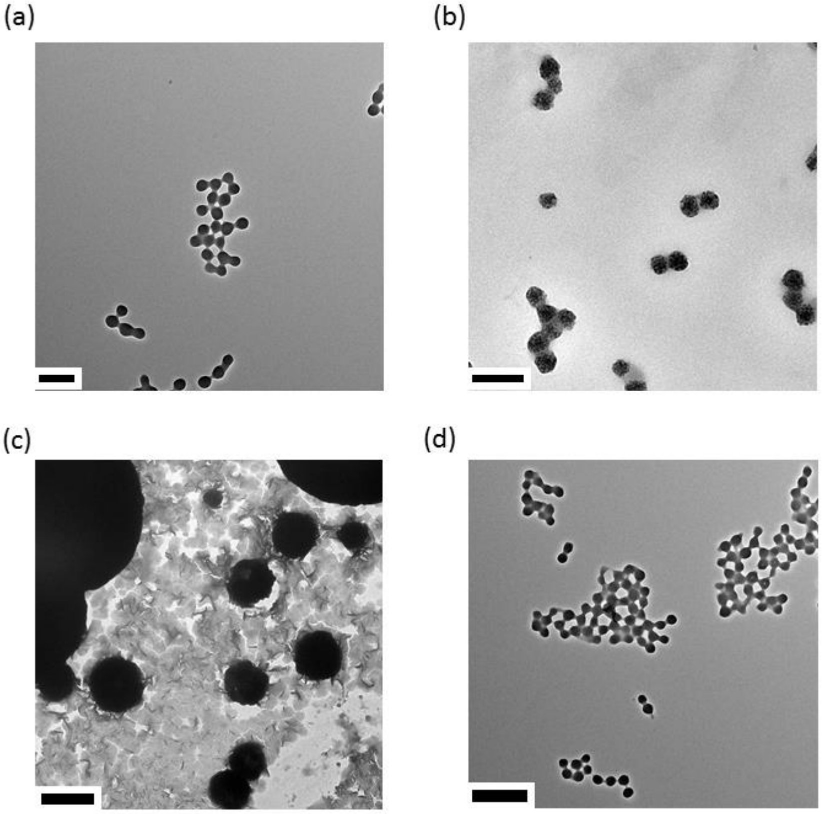

Figure 4.12. Particle size is not dependent on surface area of ammonium bicarbonate. a) TEM of particle synthesis using 30 grams of NH_4CO_3 in a 100 mL beaker, scale bar 200 nm b) TEM of particle synthesis using 30 grams of NH_4CO_3 in a 400 mL beaker, with some particle clumping noted, scale bar 200 nm c) TEM of particle synthesis using 157 g of NH_4CO_3 in a 400

mL beaker, scale bar 1 μm d) TEM of particle synthesis using approximately 157 g of NH_4CO_3 spread across 15 vials, scale bar 500 nm.

Given the dependence on NH_4CO_3 we took TEM of the ammonium bicarbonate samples. TEM of the ammonium bicarbonate samples fresh and after several runs revealed nanocrystals that aligned with the above observations. (Figure 4.13a, 4.13b). In particular, in the fresh ammonium bicarbonate the nanocrystals are closer to the larger 100 nm. (Figure 4.13a) In the ammonium bicarbonate after several runs we find the nanocrystals are closer to 20 nm suggesting that the larger ammonium bicarbonate disappeared with runs, and explaining the lowering size.

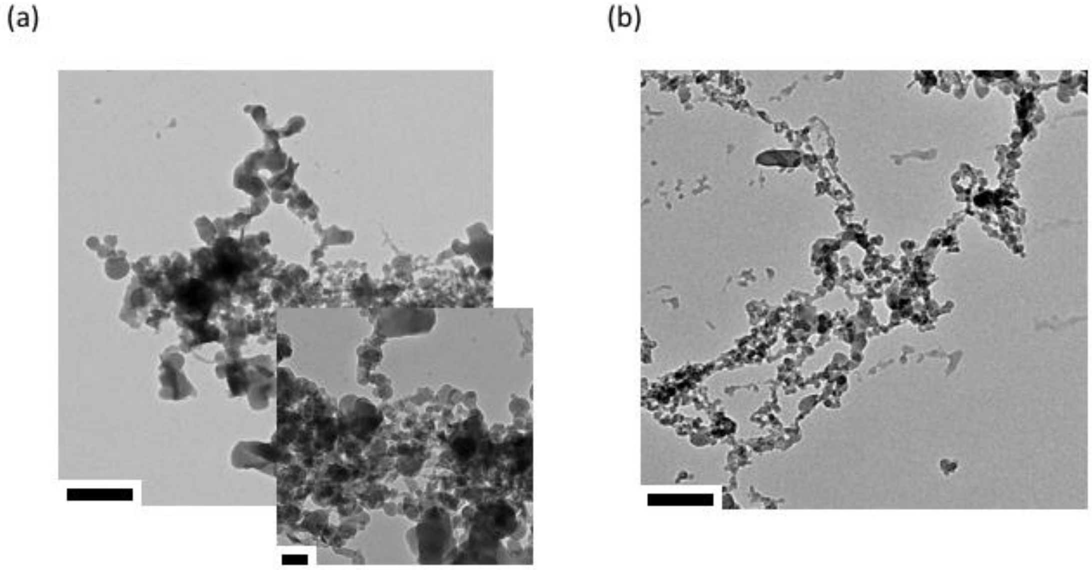

Figure 4.13 TEM of Ammonium bicarbonate a) TEM of fresh ammonium bicarbonate pre reaction, scale bar 500 nm, subset 100 nm b) TEM of ammonium bicarbonate after reaction x3, scale bar 200 nm

4.3.6 Ammonium bicarbonate constrained synthesis of $CaCO_3$ can use a variety of organic solvents

Given the constrained size by ammonium bicarbonate we hypothesized that a similar synthesis of $CaCO_3$ would occur in other organic solvents. (Figure 4.14). We find that MeOH has identical particle formation, with a high yield. Synthesis in DMF is curious in that we see a mix of small and large particles. The synthesis technique does break down in water with large aggregates forming. We found that small amounts of water (0.4%, 200 μL) can be tolerated (Figure 4.14a). In particular hypothesize that the formation of vaterite instead of amorphous $CaCO_3$, as described previously[14], is due to the increased water concentration from the hexahydrate. Larger amounts of water (20%, 10 mL), on the other hand caused a disruption of the spherical structure and created large aggregates (Figure 4.14b). This may be related to the capacity of the dessicator to dry out the EtOH + H_2O solution.

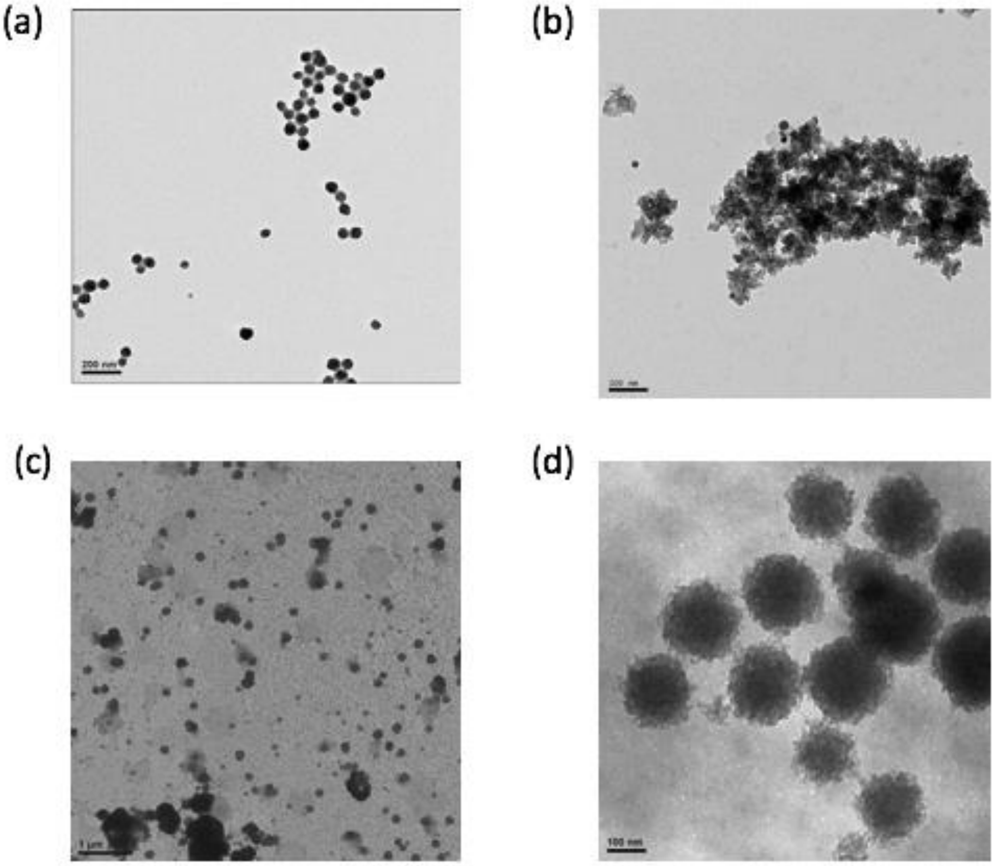

Figure 4.14 Ammonium bicarbonate constrained CaCO3 synthesis in other solvents: a) With 200μL water in 50 mL EtOH b) with 20% water/EtOH c) in DMF d) in MeOH

4.3.7 Ammonium Bicarbonate Constrained Vacuum Assisted Synthesis can be used to create other carbonate nanoparticles.

We find that applying the same exact synthesis technique albeit with 140 mg to 200 mg of $AuCl_2$, $FeCl_2$, or $ZnCl_2$ induces the similar formation of the respective carbonate nanoparticles, constrained to approximately 100 nm in size. This validates the hypothesis that the size constraint comes from the ammonium bicarbonate crystals and not the salt-EtOH solution. (Figure 4.15).

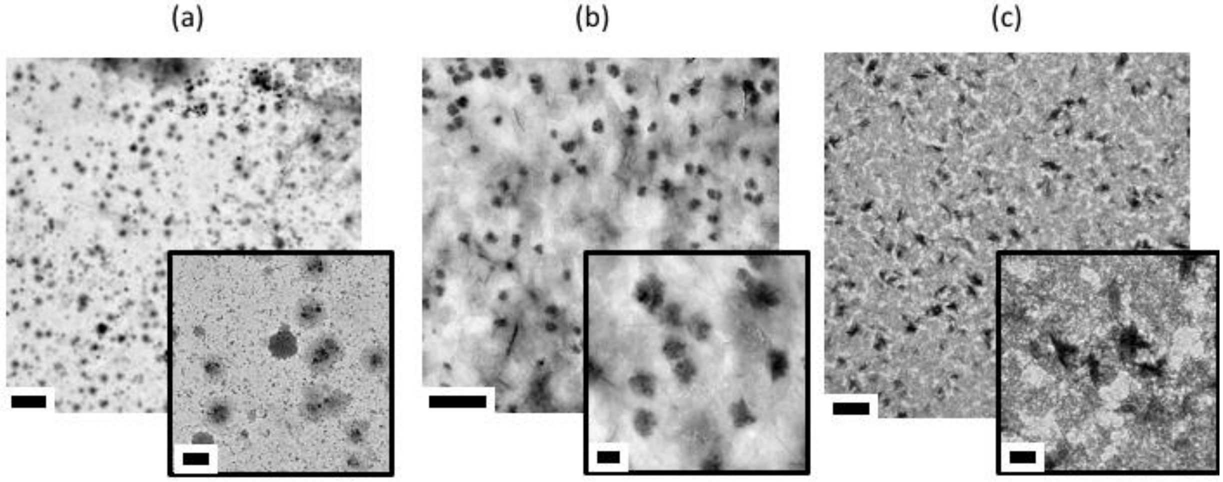

Figure 4.15 Ammonium bicarbonate constrained metal carbonate synthesis in EtOH. Scale bar 0.5 µm, subset 100 nm a) $AuCO_3$ b) $ZnCO_3$ c)FeCO

4.4. Discussion

$CaCO_3$ suffers from poor replicability and ill-understood synthesis steps. To better understand $CaCO_3$ nanoparticle formation, we undertook a detailed study on the factors involved in size determination and yield in a highly reproducible synthesis procedure based on ammonium bicarbonate aerosolization (Table 4.1).

Table 4.1: Summary of factors and effect on size and yield.

Factor	**Size**	**Yield**
Concentration of $CaCl_2$	No Effect	Increase
Volume of $CaCl_2$ solution	No Effect	Increase
Surface area of $CaCl_2$ solution	No Effect	No Effect
Time under vacuum	No Effect	Increase
# of runs	Decreases	Decreases
Amount of ammonium bicarbonate	Increases size to 100 nm	Increases
Surface Area of ammonium bicarbonate	No effect (to a point)	No Effect

Aerosolization based nanoparticle synthesis is rare, especially resulting in monodisperse nano-crystals. Indeed, previous studies have shown that controlling aerosolization is difficult. [25]

As a result, more classical synthesis techniques control size by time-based deposition or restriction from a micellar nano-bubble form. However, for this synthesis technique we find a counterintuitive phenomenon, with neither of those effects occurring. Note that the solution is not being homogenized as there is no stirring involved, and yet the particles are remarkably monodisperse. This phenomenon adds credence to the dependence of the nanoparticle size on ammonium bicarbonate nanocrystals.

Thus, vacuum assisted synthesis of $CaCO_3$ reveals a rare method of synthesis of nanoparticles via aerosolization of a solid reagent, in this case nano-crystal ammonium bicarbonate. Future work will look at exploring nanoparticle generation in this class of synthesis, particularly expanding on the ability to produce carbonate nanocrystals of other metals, including gold, iron and zinc.. The reliance on a relatively small number of variables of only one reagent makes this synthesis technique particularly robust, explaining its high reproducibility.

Overall, $CaCO_3$ as a nanomaterial has multiple uses *in vivo* as a drug delivery carrier and therapeutic. To be used widely, we describe the mechanism behind vacuum assisted $CaCO_3$ synthesis. In this study we demonstrated the only underlying involved in determining the size of $CaCO_3$ particles was the ammonium bicarbonate nanocrystals. Moreover, because the nanoparticle size is dependent only on a very limited number of variables during synthesis, we find that the synthesis method is particularly robust and allows the synthesis for a wide range of nanocrystals. Controlling the crystal growth of a nanoparticle has continued to be difficult. The identification of albumin enables the use of $CaCO_3$ *in vivo* for exploring the therapeutic implications of $CaCO_3$The extension of the method to other carbonate crystals, as described here for gold, zinc, and iron, opens a new field for carbonate crystal engineering.

4.5 Copyright Acknowledgment

All figures and work here are taken with permission from manuscripts whose citations are below.

Avik Som and Samuel Achilefu, "Ammonium bicarbonate nanocrystals enable constrained synthesis of $CaCO_3$ nanoparticles" *Materials, to be submitted*

Reproduced from Avik Som, Ramesh Raliya, Limei Tian, Walter Akers, Joseph E. Ippolito, Srikanth Singamaneni, Pratim Biswas, and Samuel Achilefu. "Monodispersed calcium carbonate nanoparticles modulate local pH and inhibit tumor growth in vivo" *Nanoscale* 2015 with permission from The Royal Society of Chemistry

4.6 References

1 Ueno, Y., Futagawa, H., Takagi, Y., Ueno, A. & Mizushima, Y. Drug-incorporating calcium carbonate nanoparticles for a new delivery system. *Journal of controlled release : official journal of the Controlled Release Society* **103**, 93-98, doi:10.1016/j.jconrel.2004.11.015 (2005).

2 Jinhuan Wei *et al.* The inhibition of human bladder cancer growth by calcium carbonate/CalP6 nanocomposite parrticles delivering AIB1 siRNA. *Biomaterials* **34**, 1246-1354 (2013).

3 Haibao Peng, K. L., Ting Wang, Jin Wang, Jiao Wang, Rongrong Zhu, Dongmei Sun, Shilong Wang. Preparation of hierarchical mesoporous CaCO3 by a facile binary solvent approach as anticancer drug carrier for etoposide. *Nano Express*, 321 (2013).

4 Svenskaya, Y. *et al.* Anticancer drug delivery system based on calcium carbonate particles loaded with a photosensitizer. *Biophys Chem*, doi:10.1016/j.bpc.2013.07.006 (2013).

5 Sukhorukov, G. B. *et al.* Porous calcium carbonate microparticles as templates for encapsulation of bioactive compounds. *Journal of Materials Chemistry* **14**, 2073, doi:10.1039/b402617a (2004).

6 Fukano, H., Takahashi, T., Aizawa, M. & Yoshimura, H. Synthesis of uniform and dispersive calcium carbonate nanoparticles in a protein cage through control of electrostatic potential. *Inorg Chem* **50**, 6526-6532, doi:10.1021/ic200117x (2011).

7 Kim, S. K., Foote, M. B. & Huang, L. Targeted delivery of EV peptide to tumor cell cytoplasm using lipid coated calcium carbonate nanoparticles. *Cancer Lett* **334**, 311-318, doi:10.1016/j.canlet.2012.07.011 (2013).

8 Michael H. Nielsen, S. A., James J. De Yoreo. In situ TEM imaging of CaCO3 nucleation reveals coexistence of direct and indirect pathways. *Science* **345**, 1158-1162 (2014).

9 Zhongping Zhang, D. G., Hui Zhao, Chenggen Xie, Guijian Guan, & Dapeng Wang, S.-H. Y. Biomimetic Assembly of Polypeptide-Stabilized CaCO3 Nanoparticles. *J. Phys Chem* **110**, 8613-8618 (2006).

10 Wang, C. *et al.* Synthesis of hydrophobic CaCO3 nanoparticles. *Materials Letters* **60**, 854-857, doi:10.1016/j.matlet.2005.10.035 (2006).

11 Shivkumara, C., Singh, P., Gupta, A. & Hegde, M. S. Synthesis of vaterite CaCO3 by direct precipitation using glycine and l-alanine as directing agents. *Materials Research Bulletin* **41**, 1455-1460, doi:10.1016/j.materresbull.2006.01.026 (2006).

12 Shao-Feng Chen, S.-H. Y., Jun Jiang, Fanqing Li, and Yankuan Liu. Polymorph Discrimination of CaCO3 Mineral in an Ethanol/Water Solution: Formation of Complex Vaterite Superstructures and Aragonite Rods. *Chem. Mater* **18**, 115-122 (2006).

13 Kralj, D. & Brecevic, L. Vaterite growth and dissolution in aqueous solution: Kinetics of crystal growth. *Journal of Crystal Growth* **104**, 793-800 (1990).

14 Chen, S. F., Colfen, H., Antonietti, M. & Yu, S. H. Ethanol assisted synthesis of pure and stable amorphous calcium carbonate nanoparticles. *Chemical communications* **49**, 9564-9566, doi:10.1039/c3cc45427d (2013).

15 Greish, K. in *Cancer Nanotechnology Methods and Protocols* Ch. 2, 25-37 (2010).

16 Som, A. *et al.* Monodispersed calcium carbonate nanoparticles modulate local extracellular pH and inhibit tumor growth in vivo *Nanoscale* (2015).

17 Schroeder, A. *et al.* Treating metastatic cancer with nanotechnology. *Nature reviews. Cancer* **12**, 39-50, doi:10.1038/nrc3180 (2012).

18 Cai, A. *et al.* Direct Synthesis of Hollow Vaterite Nanospheres from Amorphous Calcium Carbonate Nanoparticles via Phase Transformation. *Journal of Physical Chemistry C* **112**, 11324-11330, doi:10.1021/jp801408k (2008).

19 Smeets, P. J., Cho, K. R., Kempen, R. G., Sommerdijk, N. A. & De Yoreo, J. J. Calcium carbonate nucleation driven by ion binding in a biomimetic matrix revealed by in situ electron microscopy. *Nature materials* **14**, 394-399, doi:10.1038/nmat4193 (2015).

20 Gebauer, D., Völkel, A. & Cölfen, H. Stable prenucleation calcium carbonate clusters. *Science* **322**, 1819-1822 (2008).

21 Demichelis, R., Raiteri, P., Gale, J. D., Quigley, D. & Gebauer, D. Stable prenucleation mineral clusters are liquid-like ionic polymers. *Nat Commun* **2**, 590, doi:http://www.nature.com/ncomms/journal/v2/n12/suppinfo/ncomms1604_S1.html (2011).

22 Jennings, B. & Parslow, K. Particle size measurement: the equivalent spherical diameter. *Proceedings of the Royal Society of London. A. Mathematical and Physical Sciences* **419**, 137-149 (1988).

23 Sam Katz, I. M. K. Interactions of Calcium with Serum Albumin. *Archives of Biochemistry and Biophysics* **44**, 351-361 (1953).

24 Xia, Y. S. a. Y. Shape-Controlled Synthesis of Gold and Silver Nanoparticles. *Science* **298**, 2176-2178 (2002).

25 Knut Deppert, K. N., Martin H. Magnusson, F. Einar Kruis, & Fissan, a. H. Feasibiility study of nanoparticle synthesis from powders of compounds with incongruent sublimation behavior by the evaporation/condensation method. *NanoStructured Materials* **10**, pp. 565-573 (1998).

Chapter 5: Biodistribution and Toxicity Screening of $CaCO_3$ *in vivo*

5.1 Introduction

Cancer therapy remains a difficult problem, with significant side effects and off target effects of common methods. Nano-$CaCO_3$ may potentially be a useful platform for tumor therapy via two mechanisms, pH sensitive drug delivery and direct modulation of the local pH. [1-4]

Nano-$CaCO_3$ has significantly useful properties over other nanoparticle platforms. The degradation products of Nano-$CaCO_3$ are only calcium, which is regulated by the kidney and deposited into the bone and CO_2 which is rapidly excreted via the lungs. As a result long term foreign deposition issues are hypothesized to not a problem. In addition, $CaCO_3$, is tightly controlled in the body to a certain pH, in this case 7.4.[4] This is particularly ideal, as the extracellular acidity induced by Warburg metabolism results in an extracellular pH between 6.4 to 7.2.[5,6] As a result, $CaCO_3$ dissolves selectively in these acidic regions resulting in both the delivery of any cargo, and the neutralization of the pH towards more physiological range. These pH changes alone have been shown to inhibit cancer growth, putatively due to changes in enzyme kinetics, and are promising for synergy with other therapies, including chemotherapy, radiation therapy, and immunotherapy. [7-18]

For synergy to be possible, understanding the biodistribution and toxicity of $CaCO_3$ nanoparticles is critical. However, unlike more standard gold and silver nanoparticles, nano-$CaCO_3$ does not have significantly different intrinsic contrast to normal tissue due to the high prevalence of calcium and carbonate in the body. As a result, nano-$CaCO_3$ has not been imaged *in vivo*. Imaging and/ or quantification of amount is critical to understand both timing and extent of distribution of the particle for $CaCO_3$ to be a useful platform.

There are several challenges towards imaging nano-$CaCO_3$ in vivo. TEM imaging of $CaCO_3$ are hard to visualize due to equivalent electron density surrounding globules. Calcium and carbonate measurements themselves are difficult to differentiate from the background concentrations of calcium and carbonate. Because the particles dissolve *in vivo*, surface modification with fluorescent or other contrast agents is not reliable.

Among imaging systems then, MR has the widest clinical translation possibility as MR allows full depth penetration and time course imaging. MR has been used in the past to follow magnetite nanoparticle distributions.[19,20] In order to image nano-$CaCO_3$ we undertook the synthesis of a magnetite impregnated $CaCO_3$ nanocrystal of similar properties to nano-$CaCO_3$. MR imaging of vaterite-magnetite allows for biodistribution testing of nano-$CaCO_3$ both in animal models, and in the future, in humans. The results of this study allow for the use of nano-$CaCO_3$ as an organic biodegradable alternative to metal and polymeric nanoparticles for nanotechnology in cancer therapy.

5.2 Materials and Methods

5.2.1 Transmission Electron Microscope (TEM).

TEM micrographs were obtained using a FEI Spirit TEM (Hillsboro, USA) operated at 120 kV. A 400-mesh Formvar® carbon-coated copper grid was glow-discharged in a vacuum evaporator (Denton, Moorestown, New Jersey) for 30 s. The sample was prepared by placing 2 μL of sonicated $CaCO_3$ nanoparticles solution onto the grid and wicking off the excess sample with filter paper after 30 s. Alternatively, for EtOH or DMSO solvent based solutions, 3 ***μ***L of particle solution were placed on the grid and left to dry out at room temperature or with the aid of a heat gun.

5.2.2 X-Ray Diffraction (XRD).

XRD patterns were obtained by using the Bruker d8 Advance X-ray Diffractometer (Bruker, USA) configured with a Cu X-Ray tube with 1.5418 Å for analysis of powder samples using LYNXEYE_XE detector. For the analysis, fine acetone ground $CaCO_3$ nanoparticles were kept on a Zero Diffraction Plate (MTI Corporation, USA). XRD data were scanned from 20-60 degrees, with a 0.04 degree step size, a 0.5 s per step count time, with sample rotation turned on (15 rotations per min), with a coupled two-theta/theta scan. The Bruker Diffrac.Eva program was used for the evaluation and processing of X-ray diffraction scan data. Search-match operations included search by DI list, by name, using chemistry filters, and creating an International Centre for Diffraction Data (ICCDD PDF) database filter.

5.2.3 Hydrodynamic diameter and electro-kinetic zeta potential.

To study agglomeration kinetics of $CaCO_3$ nanoparticles, hydrodynamic diameter (*Dh*) was measured using DLS (Malvern Instruments, Southborough, Massachusetts). Agglomeration kinetics were measured on the basis of data obtained from TR-DLS.

The zeta potential was measured using a Malvern Zetasizer Nano ZS instrument. An applied voltage of 100 V was used for the nanoparticles. A minimum of three measurements were made per sample.

5.2.4 Determination of toxicity in rats

3 month old Sprig Dawley rats (n=3) were injected with an allometrically dosed 25.4 mg/Kg (to match the dose originally given to mice) of 30 mg/mL 100 nm $CaCO_3$ particles in 2% rat serum albumin PBS supplemented with $CaCl_2$ and $MgCl_2$. For control, 3 month old Sprig Dawley rats (n=3) were injected with a vector of 2% rat serum albumin PBS supplemented with $CaCl_2$ and $MgCl_2$ at an equivalent volume dosage as in the treated group.

5.2.5 Determination of toxicity in cells

HT1080 cells were grown to near confluency in a 96 well plate and incubated with $CaCO_3$ at a decreasing concentration for 24 hours both under original IMDM media, and IMDM media that was acidified to pH of 6.45 by titration with 1M HCl. Toxicity was assessed via the sulfarhodamine B assay.

5.2.6 Imaging Test of Vaterite-magnetite nanocomposite

81 mg of Vaterite-magnetite was suspended in 1 mL of 2% BSA in PBS with $MgCl_2$ and $CaCl_2$ and then diluted five times, each time by a factor of 10. The resulting 1 mL solutions (81 mg/mL, 8 mg/mL, 0.8 mg/mL , 0.08 mg/mL, and 0.008 mg/mL) were placed in eppendorf tubes and the

transverse relaxation rate constant (R^2) for each dilution was measured using a Car-Purcell-Meiboom-Gill-type spin-echo sequence employing 12 echo times ranging from 13 to 300 ms and a TR of 2 sec. The transverse relaxivity of the particle (r2) was calculated based on the linear relation (assuming low concentrations of particles) between R2 and particle/iron concentration;

$$R^2\text{,obs} = R2\text{,}0 + r^2\,[NP],$$

where R2,obs is a measured transverse relaxation rate constant, R^2,0 is the calculated transverse relaxation rate constant in the absence of the nanoparticle (often referred to as the "background" R2), r^2 is the transverse relaxivity of the particle, and [NP] is the nanoparticle concentration.

5.2.7 *in vivo* imaging

Three nude mice were injected with HT1080 tumors in the dorsal flank and grown to approximately 1.5 cm x 1.5 cm. 1 mg of vaterite-magnetite was injected via tail vein and measured using a Car-Purcell-Meiboom-Gill-type spin-echo sequence employing 12 echo times ranging from 13 to 300 ms and a TR of 2 sec at T= post injection, ~1-3 hours, 4-6 hours, and 24 hours post injection.

5.3 Results

5.3.1 Synthesis and characterization of vaterite-magnetite

The process of synthesizing the nano-composites is similar to the vaterite nanoparticle synthesis process. Magnetite particles with a mean size of 15 nm (± 2.30 nm) were obtained from Nano Research Facility of Washington University in St. Louis, USA and used for the synthesis process. These magnetite particles were suspended in DI water and added to a solution of hydrated calcium chloride. The remainder of the steps matched those we have reported before for the vaterite particle synthesis. During the synthesis process the addition of ethylene glycol to the solution was done to increase the viscosity of the solution and thereby reduce the molecular diffusion[21] giving particle sizes of 100 ± 8.5 nm. Thus, it is seen that the viscosity of the solution plays a major role in the formation of the metastable vaterite nanoparticles. Removal of water through washing is essential as the presence of water encourages the particles to nucleate further and change phase from vaterite to calcite. Fig. 5.1, presents the TEM images of the particles dispersed in methanol and it can be seen that the vaterite particles have a characteristic spherical shape and size range of 100 ± 8.5 nm. Also, the images of the vaterite-magnetite nano-composites show dark spots matching the size of the added magnetite nanoparticles within the bulk vaterite particle.

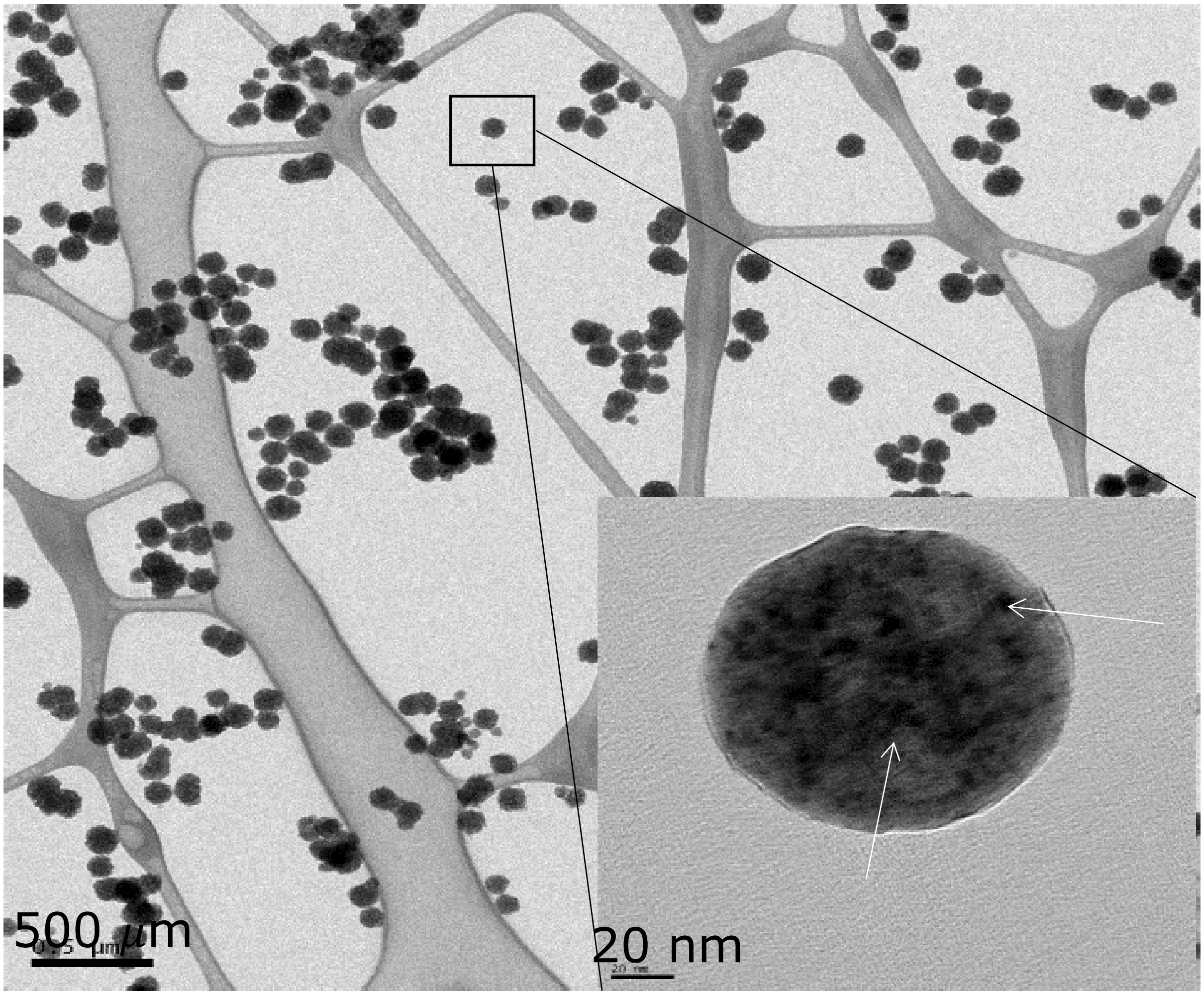

Fig. 5.1 TEM images of Vaterite-Magnetite particles when dispersed in methanol. (A) Agglomerates of the vaterite-magnetite nano-composites. Inset in A: Scaled up image of the vaterite-magnetite particles (scale bar of 20nm). The black dots indicated by arrows within the bulk of the $CaCO_3$ particle are the magnetite nanoparticles

5.3.2 $CaCO_3$ with magnetite incorporated remains vaterite.

To confirm the crystal phase of the $CaCO_3$ or magnetite-$CaCO_3$ nanoparticle, XRD patterns were obtained by using the Bruker d8 Advance X-ray Diffractometer (Bruker, USA) configured with a 1.5418 Å Cu X-Ray tube for analysis of powder samples using LYNXEYE_XE detector. The diffraction pattern has clear represenation of vaterite phase of $CaCO_3$ as shown in Fig. 3. However, there was a very small intensity peak of aragonite phase was also observed. Diffraction pattern of magnetite-$CaCO_3$ shows the consistancy in phase purity. (Figure 5.2)

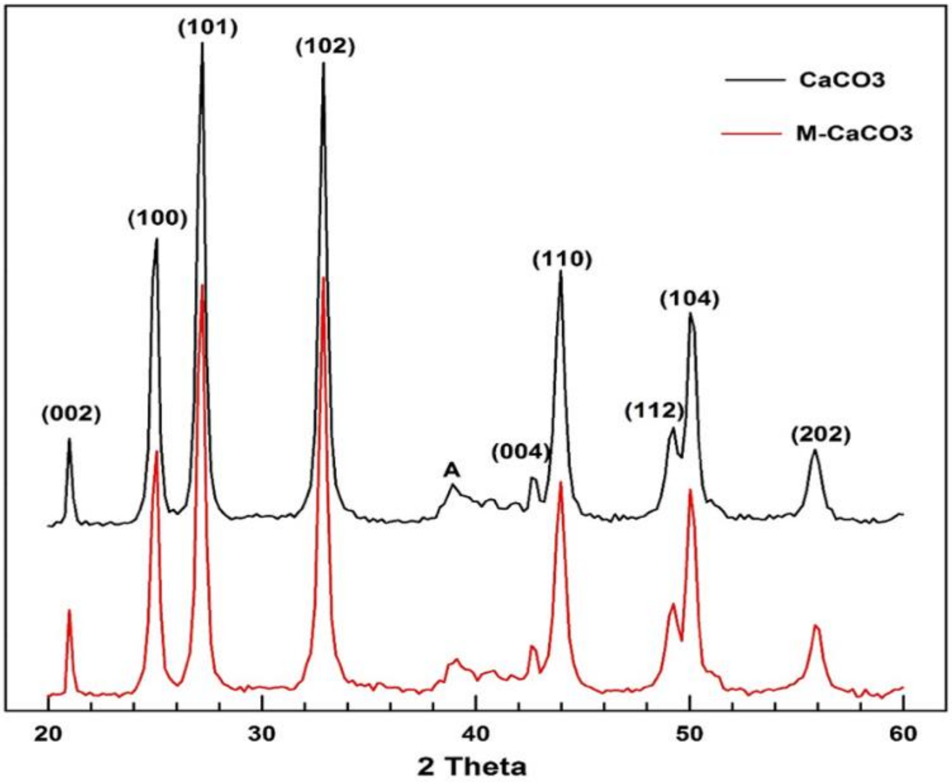

Fig. 5.2 XRD Characterization of $CaCO_3$ and magnetite-$CaCO_3$ (m-$CaCO_3$) composite

5.3.3 Stability of $CaCO_3$ in aqueous medium

A chemical compound used for biomedical application needs colloidal stability, help in storage, transport and delivery of the compund into patient body. The synthesized particles may have huge utility as pH neutralizers in cells[22-24] due to their small size and high pH neutralization capacities. To check their feasibility for pH neutralization in vivo, the size and stability of these particles in different solvents is checked using Time-resolved dynamic light scattering technique (TR-DLS) for duration of 30 minutes. The stability of both, the vaterite nanoparticles and the nano-composites in a variety of solvents such as water, saline, Bovine serum albumin, Dulbecco's Modified Eagle Medium (DMEM), ethanol, methanol and Phosphate Buffer Saline (PBS). The Fig. 5.3 shows the stability tests imply that albumin has a high affinity for the calcium carbonate and resists two particles from coming together, thus stabilizing the particles in a solution. The PBS solution encourages precipitation of the particles by increasing their supersaturation.[25] This leads to rapid precipitation encouraged by the addition of divalent ions (Mg^{+2} or Ca^{+2}) into the solution. The particles are also quite stable in DMEM which indicates their possible applications in growing cell cultures requiring alkaline pH environments. The results thus indicate that both the synthesized particles would be useful for industrial applications in solvents such as ethanol and would be good for biomedical applications by dissolving the same in a solution of albumin.

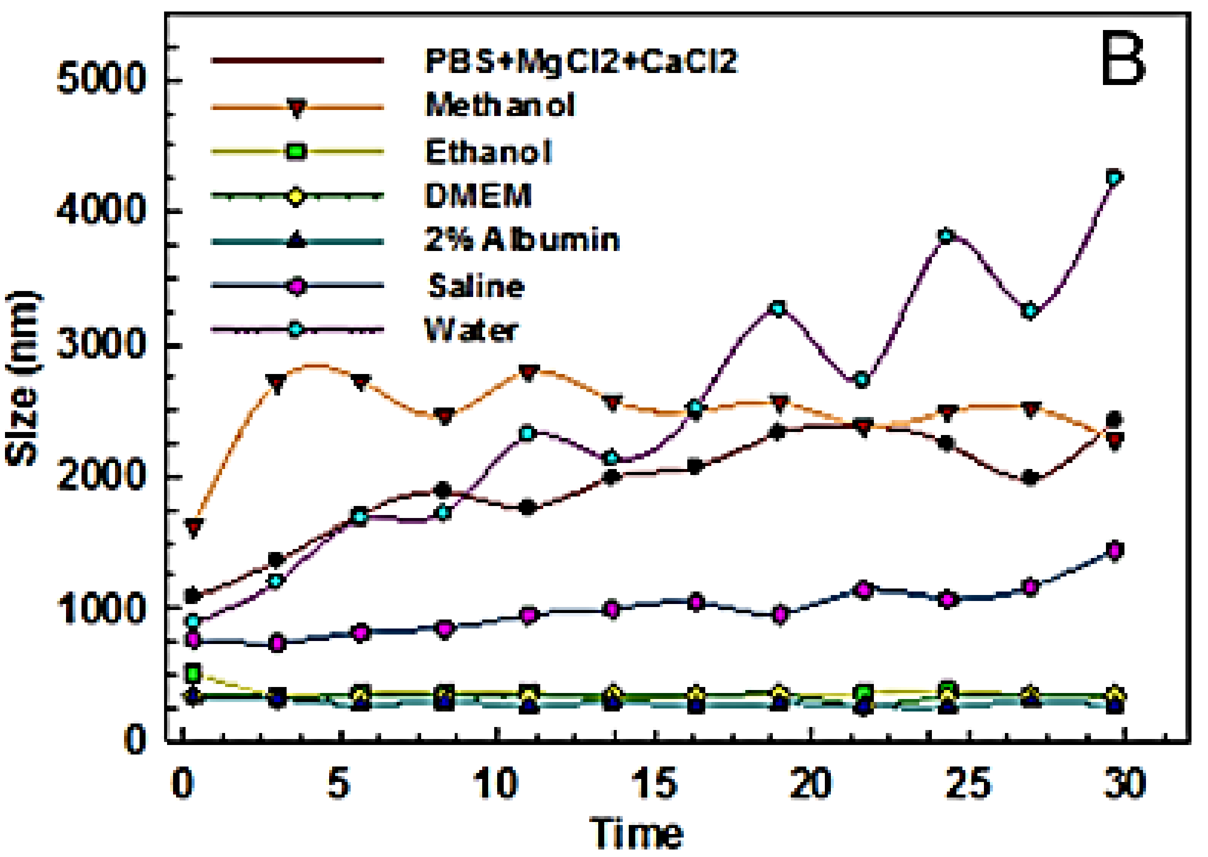

Fig. 5.3 Stability test of vaterite nanoparticles in various solvents measured by TR-DLS. (A) Vaterite-Magnetite nano-composites, the order of stability as 2% Albumin>Ethanol = DMEM>Saline>PBS+$MgCl_2$>Methanol>Water.

5.3.4 Imaging of nano-$CaCO_3$ *ex vivo* and *in vivo*

Phantom tests demonstrate a sensitivity up to 0.1 mg/mL , a 100 fold dilution from normal injection doses of 1 mg in 100 μL. Injection *in vivo* demonstrates a T2 drop (and a 1/T2 rise, first in the kidney, then liver, and finally tumor. This can be visualized in the T2 map as T2 drops post injection. We find that the particles cause a drop relatively rapidly, with a trough at around 6 hours with almost complete return of signal by 24 hours. The significant reduction of T2 in the bladder suggests a large renal clearance. (Figure 5.4)

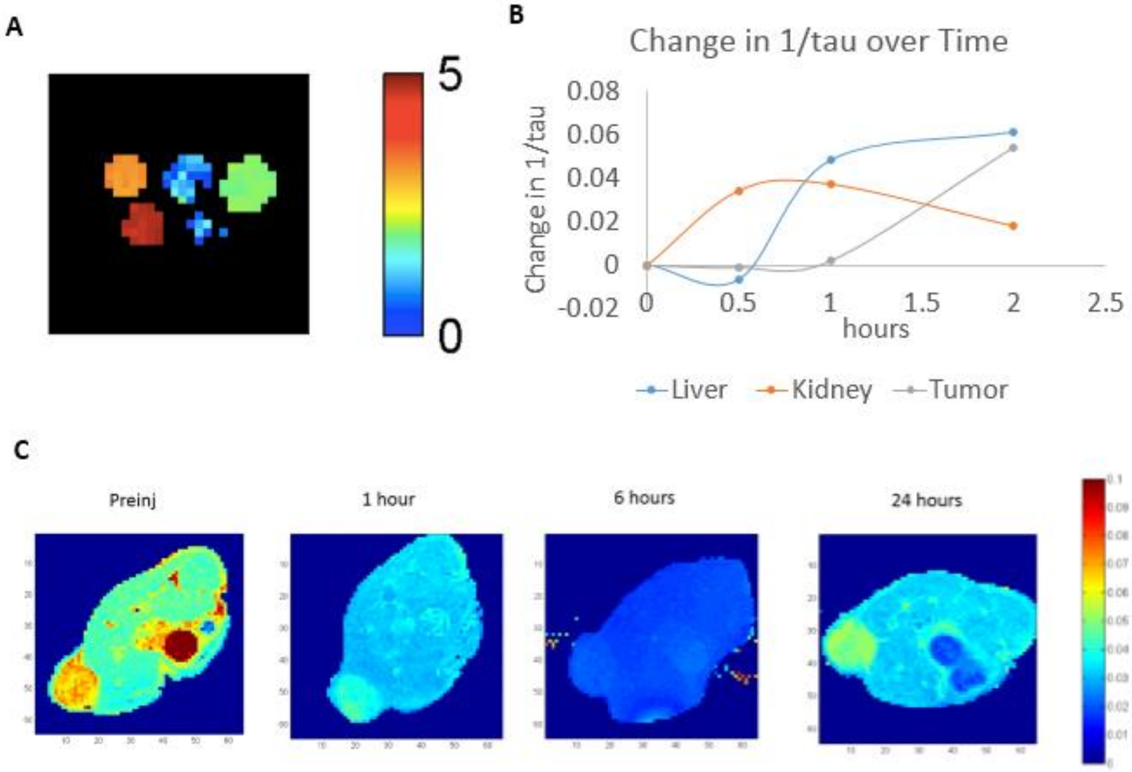

Figure 5.4. MR Imaging of $CaCO_3$. (a) Ex vivo phantom imaging of vaterite-magnetite at different concentrations. (b) Change in $1/\tau$ over time in liver, kidney, and HT1080 tumor. (c) Visualization of T2 changes with vaterite magnetite injection.

5.3.5 Toxicity Studies

For $CaCO_3$ nanoparticles synthesized by this method to be a standard platform particle for use in situations similar to more classical gold or metal based nanoparticles, a biologically inert phenotype is necessary. Indeed, in cell studies we find that there is no specific toxicity on HT1080 cells up to 1.20 mg/mL. *In vivo*, we tested this hypothesis using a rat animal model for translational toxicity studies. Indeed, we find little to no significant changes in organ weights, blood chemistries, and blood counts 24 hours after 25 mg/Kg

$CaCO_3$ injection compared to control (Figure 5.5). There was a significant albeit slight rise in blood urea nitrogen, but because there was no concurrent creatinine or liver enzyme rise, the rise was suggested to be nonspecific and may resolve with larger numbers of replicates (Figure 5). There was nonspecific pathology across both control and treated groups that was attributed to age. Given these results, we conclude that nano-$CaCO_3$ is not inducing widespread toxicity, and infer that this is most likely due to the pH not increasing beyond 7.4 in normal organs as reported before.

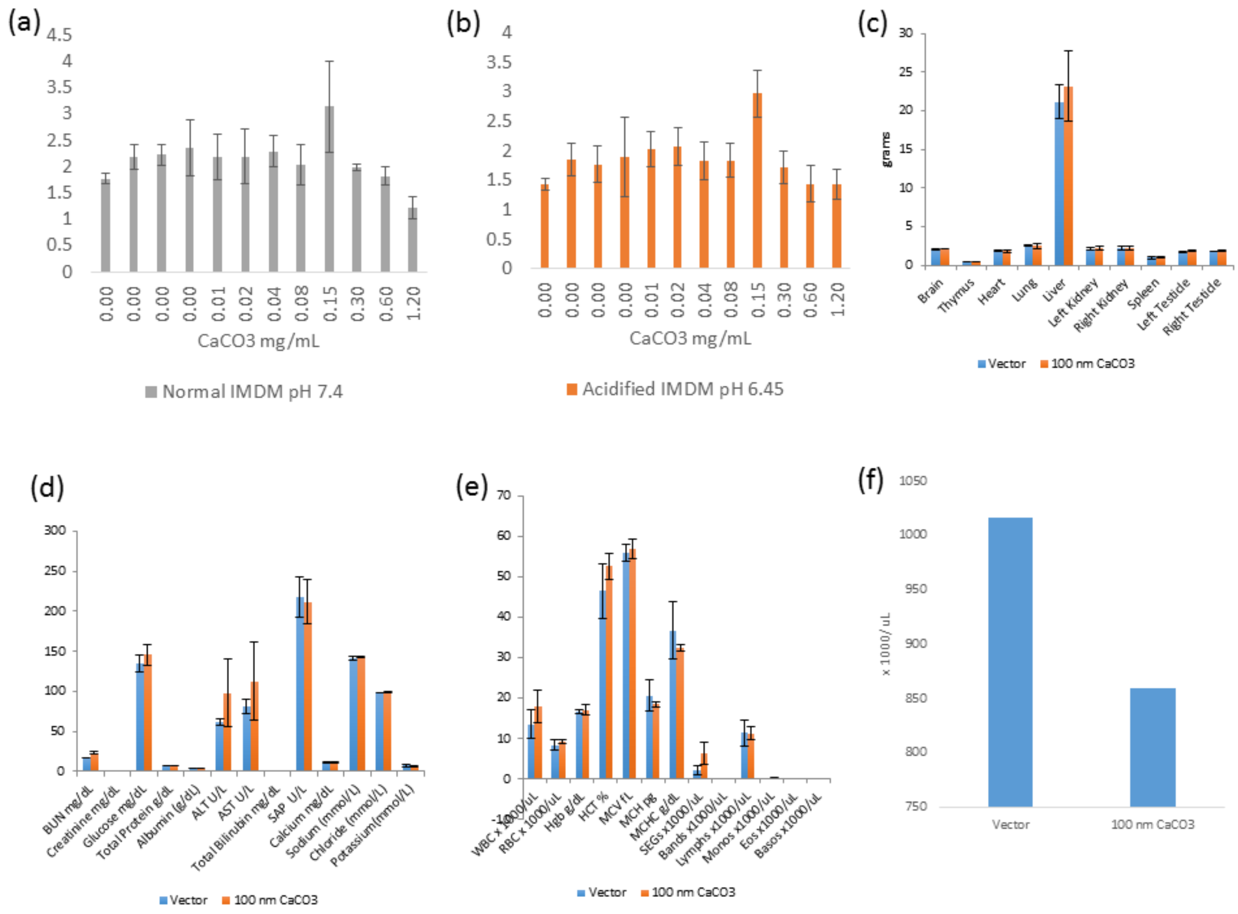

Figure 5.5. $CaCO_3$ is non-toxic (a) Toxicity of 100 nm $CaCO_3$ particles in standard pH 7.4 IMDM media. (b) Toxicity of 100 nm $CaCO_3$ particles in pH 6.45 IMDM media. (c) Organ weights with vector versus 100 nm $CaCO_3$. (d) Serum biomarker values (e) Complete blood count. (f) Platelet count.

5.4 Discussion

The ability to visualize $CaCO_3$ *in vivo* allows for practical design of dosing and pharmacokinetics. The ability to impregnate magnetite nanoparticles into the existing nanoparticle formation is a significant improvement to answer this question. The magnetite in particular is uniformly distributed across the particle, allowing for a better approximation of the location of the entire particle.

However there are limitations with this model. Although magnetite allows for MR based noninvasive imaging, it also has poor resolution and low sensitivity. As such, it is unclear exactly when $CaCO_3$ finishes clearing. It is also unclear whether the reduction in signal is due to dissolution or washout of the particles.

Toxicity studies of the $CaCO_3$ nanoparticles are important validation points for the practical usage of $CaCO_{3.}$ Calcium and Carbonate are on their own easily degradable and biocompatible. However, as a nanoparticle, the existence of liver and kidney toxicity remains a concern. The results from the rat studies suggest minimal acute toxicity. Further studies on chronic toxicity will be ideal.

Future studies on the material will look at other methods to validate biodistribution. Other possibilities include Raman Microscopy and C^{13} mass spectrometry as methods to visualize the intrinsic properties of the material, rather than using a co-carrier such as magnetite.

5.5 Copyright Acknowledgment

All figures and writing is taken in whole or in part from the following manuscripts

Avik Som*, Ramesh Raliya*, Nathan Reed, Scott Beeman, Joel Garbow, Joe Ippolito, Matthew Brandenburg, Samuel Achilefu, "Biodistribution and toxicity screening of nano-$CaCO_3$ *in vivo"* To be submitted.

5.5 References

1 Ueno, Y., Futagawa, H., Takagi, Y., Ueno, A. & Mizushima, Y. Drug-incorporating calcium carbonate nanoparticles for a new delivery system. *Journal of controlled release : official journal of the Controlled Release Society* **103**, 93-98, doi:10.1016/j.jconrel.2004.11.015 (2005).

2 Jinhuan Wei *et al.* The inhibition of human bladder cancer growth by calcium carbonate/CalP6 nanocomposite parrticles delivering AIB1 siRNA. *Biomaterials* **34**, 1246-1354 (2013).

3 Haibao Peng, K. L., Ting Wang, Jin Wang, Jiao Wang, Rongrong Zhu, Dongmei Sun, Shilong Wang. Preparation of hierarchical mesoporous CaCO3 by a facile binary solvent approach as anticancer drug carrier for etoposide. *Nano Express*, 321 (2013).

4 Som, A. *et al.* Monodispersed calcium carbonate nanoparticles modulate local extracellular pH and inhibit tumor growth in vivo *Nanoscale* (2015).

5 Marion Stubbs, P. M. J. M., John R. Griffiths, and C. Lidsay Bashford Causes and Consequences of tumour acidity and implications for treatment. *Molecular Medicine Today* **6**, 15-19 (2000).

6 Agatha S. E. Ojugo *et al.* Measurement of extracellular pH of solid tumors in mice by MR Spectroscopy. Comparison of exogenous 19F and 31 P probes. *NMR in Biomedicine* **12**, 495-504 (1999).

7 Thews, O., Gassner, B., Kelleher, D. K., Schwerdt, G. & Gekle, M. Impact of extracellular acidity on the activity of P-glycoprotein and the cytotoxicity of chemotherapeutic drugs. *Neoplasia* **8**, 143-152, doi:10.1593/neo.05697 (2006).

8 Lee, E. S., Gao, Z. & Bae, Y. H. Recent progress in tumor pH targeting nanotechnology. *Journal of controlled release : official journal of the Controlled Release Society* **132**, 164-170, doi:10.1016/j.jconrel.2008.05.003 (2008).

9 Reshetnyak, Y. K., Andreev, O. A., Segala, M., Markin, V. S. & Engelman, D. M. Energetics of peptide (pHLIP) binding to and folding across a lipid bilayer membrane. *Proceedings of the National Academy of Sciences of the United States of America* **105**, 15340-15345, doi:10.1073/pnas.0804746105 (2008).

10 Robey, I. F. *et al.* Bicarbonate increases tumor pH and inhibits spontaneous metastases. *Cancer Res* **69**, 2260-2268, doi:10.1158/0008-5472.CAN-07-5575 (2009).

11 Hsieh, M. J., Chen, K. S., Chiou, H. L. & Hsieh, Y. S. Carbonic anhydrase XII promotes invasion and migration ability of MDA-MB-231 breast cancer cells through the p38 MAPK signaling pathway. *Eur J Cell Biol* **89**, 598-606, doi:10.1016/j.ejcb.2010.03.004 (2010).

12 Robey, I. F. & Martin, N. K. Bicarbonate and dichloroacetate: evaluating pH altering therapies in a mouse model for metastatic breast cancer. *BMC Cancer* **11**, 235, doi:10.1186/1471-2407-11-235 (2011).

13 McIntyre, A. *et al.* Carbonic anhydrase IX promotes tumor growth and necrosis in vivo and inhibition enhances anti-VEGF therapy. *Clin Cancer Res* **18**, 3100-3111, doi:10.1158/1078-0432.CCR-11-1877 (2012).

14 Martin, N. K. *et al.* Predicting the safety and efficacy of buffer therapy to raise tumour pHe: an integrative modelling study. *Br J Cancer* **106**, 1280-1287, doi:10.1038/bjc.2012.58 (2012).

15 Calcinotto, A. *et al.* Modulation of microenvironment acidity reverses anergy in human and murine tumor-infiltrating T lymphocytes. *Cancer Res* **72**, 2746-2756, doi:10.1158/0008-5472.CAN-11-1272 (2012).

16 Du, J. Z., Mao, C. Q., Yuan, Y. Y., Yang, X. Z. & Wang, J. Tumor extracellular acidity-activated nanoparticles as drug delivery systems for enhanced cancer therapy. *Biotechnol Adv*, doi:10.1016/j.biotechadv.2013.08.002 (2013).

17 Robey, I. F. & Nesbit, L. A. Investigating mechanisms of alkalinization for reducing primary breast tumor invasion. *Biomed Res Int* **2013**, 485196, doi:10.1155/2013/485196 (2013).

18 Bellone, M. *et al.* The acidity of the tumor microenvironment is a mechanism of immune escape that can be overcome by proton pump inhibitors. *Oncoimmunology* **2**, doi:10.4161/onci.22058 (2013).

19 Rosenblum, L. T., Kosaka, N., Mitsunaga, M., Choyke, P. L. & Kobayashi, H. In vivo molecular imaging using nanomaterials: general in vivo characteristics of nano-sized reagents and applications for cancer diagnosis. *Molecular membrane biology* **27**, 274-285, doi:10.3109/09687688.2010.481640 (2010).

20 Shin, T. H., Choi, Y., Kim, S. & Cheon, J. Recent advances in magnetic nanoparticle-based multi-modal imaging. *Chemical Society reviews* **44**, 4501-4516, doi:10.1039/c4cs00345d (2015).

21 Parakhonskiy, B. V., Haase, A. & Antolini, R. Sub-Micrometer Vaterite Containers: Synthesis, Substance Loading, and Release. *Angewandte Chemie Int. Edn.* **51**, 1195-1197 (2012).

22 Pellegrini, P. *et al.* Acidic extracellular pH neutralizes the autophagy-inhibiting activity of chloroquine: Implications for cancer therapies. *Autophagy* **10**, 562-571 (2014).

23 Robey, I. F. *et al.* Bicarbonate increases tumor pH and inhibits spontaneous metastases. *Cancer Res.* **69**, 2260-2268 (2009).

24 Schüler, T. & Tremel, W. Versatile wet-chemical synthesis of non-agglomerated CaCO3 vaterite nanoparticles. *Chem. Comm.* **47**, 5208-5210 (2011).

25 Smeets, P. J., Cho, K. R., Kempen, R. G., Sommerdijk, N. A. & De Yoreo, J. J. Calcium carbonate nucleation driven by ion binding in a biomimetic matrix revealed by in situ electron microscopy. *Nat. Mat.* **14**, 394-399 (2015).

Chapter 6: Systemic Administration of Nano-$CaCO_3$ Inhibits Tumor Growth and Metastasis via Local pH Increase

6.1 Introduction

The current understanding of cancer development has evolved from a simple view of uncontrolled growth stemming from gene mutation within a single cell to that of complex interactions between different cell types and their local chemical environment. In particular, the 4-5 fold increase in the extracellular hydrogen ion concentration around tumor cells, previously considered a byproduct of upregulated glycolysis, appears to support elevated tumor growth, immune evasion, and metastasis.[1-5] To combat these effects, various cancer therapies focusing on modulating extracellular pH (pHe) of tumors have been investigated.[6] For instance, intracellular modulators of intrinsic proton transport and production such as proton pump and carbonic anhydrase IX inhibitors have inhibited tumor growth by increasing pH in vivo.[1,6,7] However, the intracellular targets of these drugs are expressed in non-cancerous cells and therefore can have off-target toxic effects.[7] In addition, redundancy of intracellular pathways can lead to drug resistance and loss of therapeutic efficacy over time.[8,9]

To avoid intracellular resistance pathways, dietary alterations including sodium bicarbonate can raise the systemic extracellular pH.[2] Although a positive response has been observed in some tumors, this approach requires the administration of large amounts of the salt, does not target the tumors directly, has a transient effect on tumor pHe because of the rapid clearance from circulation, and is expected to induce metabolic alkalosis, and consequent morbidity.[10]

An alternative approach to directly modulate the acidic pHe of tumors is to develop nanoparticle delivery vehicles with sustainable buffering capacity. This approach could minimize the drug resistance potential seen in intracellular therapies, but also add the selectivity seen with nanotechnology.[11] Cationic secondary amine dendrimers have been used to respond to acidic pH, particularly to escape the lysosome, for intracellular drug delivery.[12] However, dendrimers are capable of neutralizing only a small number of protons (10^{-20} mole) per nanoparticle, thereby limiting their buffering capacity. Unless a non-desirable continuous infusion of the polyamine nanoparticles is used, their buffering capacity is not regenerative and the products of amine protonation could induce off-target toxicity. Inorganic nanoparticles, such as doped $CaCO_3$, have been used for acid sensitive drug release.[13,14] However, rarely has any biocompatible inorganic nanoparticle been intentionally designed and used to modulate tumor pHe.

In this work, we developed methods to prepare monodisperse nano-$CaCO_3$ with size ranges from 20 – 300 nm. We also identified a method to stabilize the materials in aqueous media. Simulations and in vitro testing show that regenerative buffering capacity is obtained because the products of this interaction, water and bicarbonate, dissociate from the bulk nanoparticle core, creating a new surface to neutralize additional protons produced by the cells. In addition, we demonstrate that nano-$CaCO_3$ with distinct sizes can selectively localize in the extracellular region of tumors and selectively modulate the pHe of tumors in rodents, with the net effect of preventing or reducing tumor growth and metastasis (Figure 6.1).

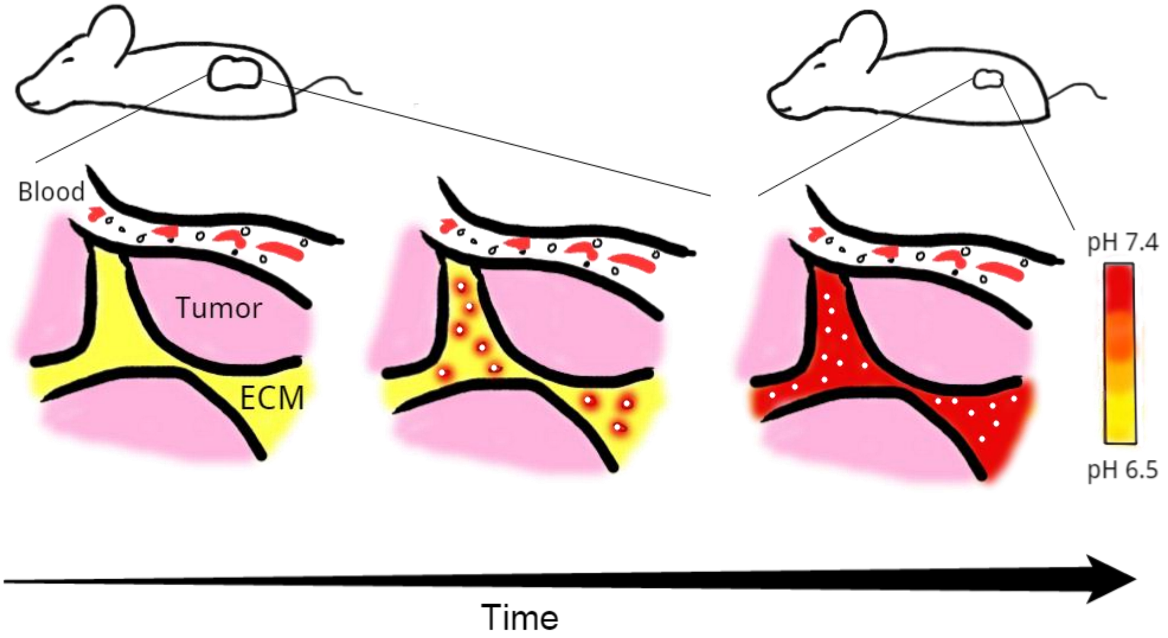

Figure 6.1. Schema of nano-$CaCO_3$. (a) High dose $CaCO_3$ enters via EPR and increases pH to 7.4. Over time this continuous dose allows chronic maintenance of pH 7.4

6.2 Materials and Methods

6.2.1 Determination of pH change in acidic media versus normal media.

We determined $CaCO_3$ dissolution over time by measuring pH changes in conditioned acidic media and fetal bovine serum. Conditioned media was from a 7-day incubation of media with HT1080 cells and an initial pH ~ 6.2. Final concentrations of $CaCO_3$ in the cell free solutions were controlled at 0.67 mg/mL. $CaCO_3$ was added to conditioned media or serum in ~10 μL of aqueous vector (PBS + $CaCl_2$ + $MgCl_2$ + 2% bovine serum albumin) under hypoxic 5% CO_2 conditions. The pH was then measured after 1 hr.

6.2.2 Determination of nano-$CaCO_3$ dose-dependent pH changes in HT1080 cell culture medium.

HT1080 cells were plated at 10^5 cells/well in a 24 well plate overnight under hypoxic conditions (0.3% O_2 and 5% CO_2), and then incubated with increasing amounts of 20 nm, 100 nm and 300 nm particles for 24 and 96 h. The particles were directly added and resuspended in media via vortexing under hypoxic conditions (0.3% O_2 and 5% CO_2). The pH was measured after 24 and 96 h incubation. n = 3 for each sample.

6.2.3 Animal studies.

All animal studies were conducted in accordance with protocols approved by the Washington University Animal Studies Committee. Mice were purchased from Charles River Laboratory.

6.2.4 Determination of pHe changes *in vivo* post bolus particle intravenous injection.

HT1080 tumors were grown subcutaneously in dorsal flanks of athymic nude mice, in dorsal bilateral flanks. Tumors generally grew in one flank. When the tumors growth reaches approximately 50 mm^3 or greater, the extracellular pH was measured using an external pH electrode. Prior to these experiments, the mice had daily I.V. $CaCO_3$ (1 mg) treatments for 3 weeks. Treatments were discontinued for at least 5 days before performing the *in vivo* pH measurements. The average initial pH was 6.94 +/- 0.147.

The pH was measured using an extracellular pH electrode implanted into the tumor following a 15 min equilibration period after electrode entry. The pH electrode was calibrated within the week. About 1 mg of each size of particles (20 nm, 100 nm, 300 nm) in a 100 μL solution consisting of PBS, $CaCl_2$, $MgCl_2$ and 2% bovine serum albumin was injected intravenously in individual mice. Approximately 100 μL of aqueous vector (PBS,

$CaCl_2$, $MgCl_2$, and 2% bovine serum albumin), 100 μL of 0.84% sodium bicarbonate in deionized (dI) water, and 100 μL of 7.5% sodium bicarbonate in dI water were each serially injected intravenously into the same mouse with 1 h gaps for measurement. Tumor sizes at time of injection for this experiment were 12 mm x 9 mm (20 nm particles), 13.7 mm x 12.5 mm (100 nm), 13.5 mm x 15.5 mm (300 nm), 12.5 x 16.5 mm (.84% bicarbonate), 12.5 x 16.5 mm (7.5% bicarbonate), and 12.5 x 16.5 mm (vector). In general, the pH was then followed each minute for a minimum of 1 h, or up to 3 h if any changes were seen. Animals could tolerate this pH measurement procedure for approximately 4 h and exhibits complete recovery after treatment. Bleeding, if any, was also noted.

6.2.5 Measurement of pH increases post multiple injections.

HT1080 tumors were grown subcutaneously in the dorsal bilateral flanks of athymic nude mice. Typically, tumors grew in one flank. When grown to approximately 8.5 mm × 8.5 mm, extracellular pH was measured using an external pH electrode. The pH was measured initially following a 15 min equilibration period post probe entry. About 100 μL of 1 mg particles (100 nm) in a solution of PBS, $CaCl_2$, $MgCl_2$, and 2% albumin was injected I.V. every hour for 3 h. The pH was measured continuously throughout.

6.2.6 Determination of tumor growth after $CaCO_3$ administration.

HT1080 tumors were grown subcutaneously in the dorsal flanks of six athymic nude mice (age ~ 8-10 weeks). After tumor growth reached about 100 mm^3, I.V. treatment with nano-$CaCO_3$ was initiated for three mice. About 1 mg of particles (100 nm) in 100 μL of a solution consisting of PBS, $CaCl_2$, $MgCl_2$, and 20 mg/mL of albumin was injected I.V. every 24 h for 5 days in three mice. The tumor size was measured for each day concurrently between treated and control for 12 days. The pH in the tumor region was then measured for each mouse as described above. During analysis, tumors that were considered too small to measure but deemed palpable, were assigned the largest size measured on Day 1 (50 mm^3) as a conservative estimate.

6.2.7 Determination of the effect of continuous infusion of $CaCO_3$ on tumor growth and metastasis.

4T1luc-GFP tumors were implanted into the mammary fat pads of Balb/c mice (syngeneic) at 400,000 cells per mouse for 3 mice. On day 1 of implantation bioluminescence was used to measure tumor size. 3 mg of nano $CaCO_3$ was suspended into 200 μL of EtOH along with 100 μM Cypate from a DMSO stock and placed in a Lynch coil connected to an Alzet Osmotic Pump (Model 2004, DURECT Corporation, Cupertino, CA 95014) with a 28 day infusion time (0.15 μL/hr), and implanted on day 2. These pumps were implanted and connected via jugular venous catheter into the animal. Animals were rested for 2-3 days. On day 6, 1 mg of $CaCO_3$ in 2%BSA+PBS+$CaCl_2$ was injected IV, and the animals imaged on day 6 post implantation, and then imaged approximately every 4 days by bioluminescence. To detect lung metastasis, the primary tumor was obstructed by a black covering and a long exposure taken on the chest region. 3 control mice were similarly implanted with orthotopic mammary fat pad tumors and followed by bioluminescence similarly for metastasis and the primary on day 1, 6, and every 4 days for up to 28 days. These mice did not get an osmotic pump.

6.2.8 Determination of the effect of continuous infusion of $CaCO_3$ on tumor extravasation (metastasis mimicking model).

Pre IV injection of tumors 3 mg of nano $CaCO_3$ was suspended into 200 μL of EtOH along with 100 μM Cypate from a DMSO stock and placed in a Lynch coil connected to an Alzet

Osmotic Pump (Model 2004, DURECT Corporation, Cupertino, CA 95014) with a 28 day infusion time (0.15 μL/hr), and implanted 3 days prior to tumor implant via jugular venous catheter into the animals. These were implanted On the day of injection, 1 mg of $CaCO_3$ in 2% BSA was injected via tail vein into each balb/c mouse. 3-5 minutes after 1 million 4T1luc GFP cells were injected by tail vein into the 3 balb/c mice. The mice were imaged 2 hours post implantation by bioluminescence, 2 days after, 6 days after, 10 days after and 16 days after before being sacrifice.

6.3 Results

6.3.1 Efficacy of modulating the acidic pHe of tumors in vivo depends on $CaCO_3$ nanoparticle size

Predicated on the simulation studies, we assessed the buffering capacity of the nanoparticles in cell-free media under 5% CO_2 and hypoxic (0.3% O_2) conditions (Figure 6.2a). In non-acidified conditioned media (pH 7.4), the solution pH was largely unchanged in the presence of different sizes and concentrations of vaterite nano-$CaCO_3$, as predicted by simulations above. However, treatment of acidic conditioned media (pH 6.2) with any of the particles (0.67 mg/mL) showed a rapid increase in pH, which did not exceed 7.2. Similarly, the pH remained at about pH 7.2 after 24 h incubation of human fibrosarcoma (HT1080) cells in normal cell culture conditions, irrespective of the nanoparticle doses used (Figure 6.2b). At 96 h post HT1080 cellular induced acidification, nanoparticle size-dependent pH changes were observed, with the 20 nm materials having the highest increase in pH. This could be attributable to the higher diffusion rate and the larger surface area of the 20 nm nano-$CaCO_3$.

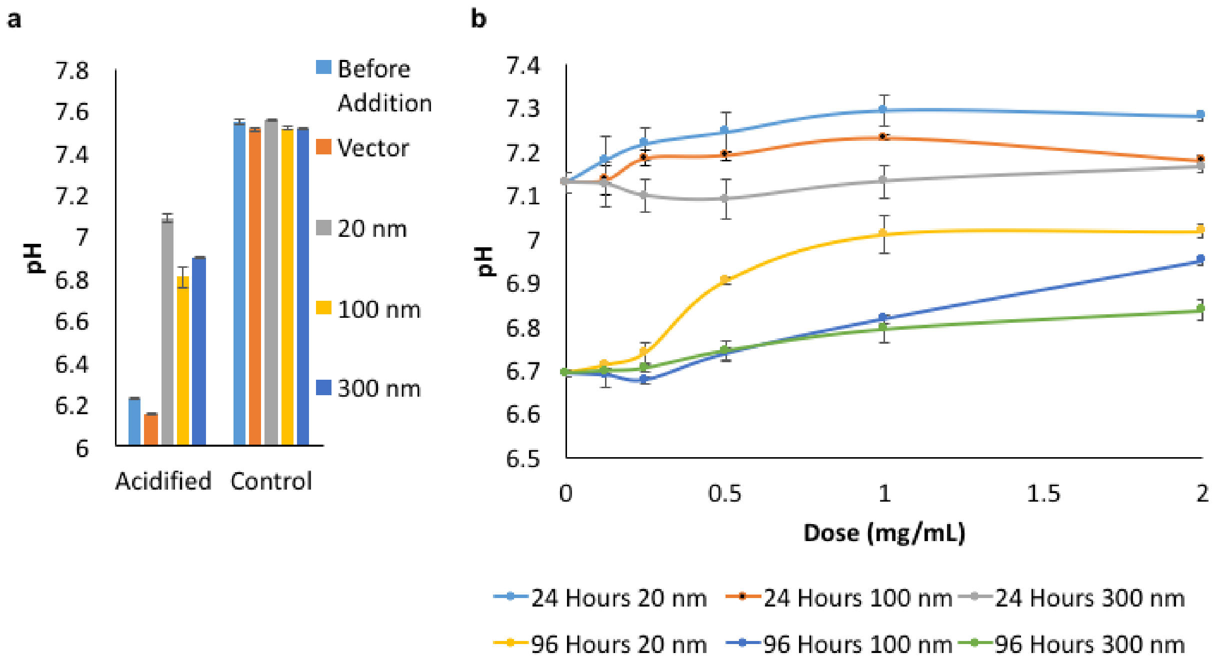

Fig. 6.2 Nano-$CaCO_3$ increases pH up to 7.4 *in vitro*. (a), pH change in media at 5% CO_2 shows a significant increase in pH when using particles as compared to vector alone. All solutions were added in 10 μL solvent (2% albumin + PBS with $CaCl_2$ and $MgCl_2$). (b), pH change versus dose when incubated with HT1080 (human fibrosarcoma) cells using different particle sizes shows an increase in pH with one dose of $CaCO_3$, as well as a differential effect on pH at later time points of growth depending on size. Error bars refer to the standard error across n = 3 biologic replicates.

Despite recent advances in noninvasive methods to measure pH, they still suffer from poor sensitivity to pHe and poor temporal resolution needed to measure the dynamic changes in pH.[15,16] To improve these parameters, we used an invasive pH electrode probe for determining the in vivo pH (Figure 6.3a). I.V. administration of 1 mg bolus injections of each of the 3 types of nano-$CaCO_3$ in HT1080 tumor-bearing mice neutralized the pH for over 3 h. The 100 nm nano-$CaCO_3$ showed the highest ΔpH and longest effect (Figure 6.3b). The 20 nm particles appeared to diffuse into and out of the tumor area more rapidly than the 100 nm particles.

Intuitively, larger particles are expected to exert higher response because of their favorable EPR effect. However, the 300 nm nano-$CaCO_3$ do not appear to appreciably increase the pHe of tumors. The poor diffusion of these particles dictates that they can only exert an effect in a small section of a three dimensional tumor environment. Our data also show that flooding the mouse with a high concentration (0.3 - 0.4 g/Kg) of sodium bicarbonate (~10x the nanoparticle I.V. dosage) did not induce a measurable pH change in the tumor region (Figure 6.3b).

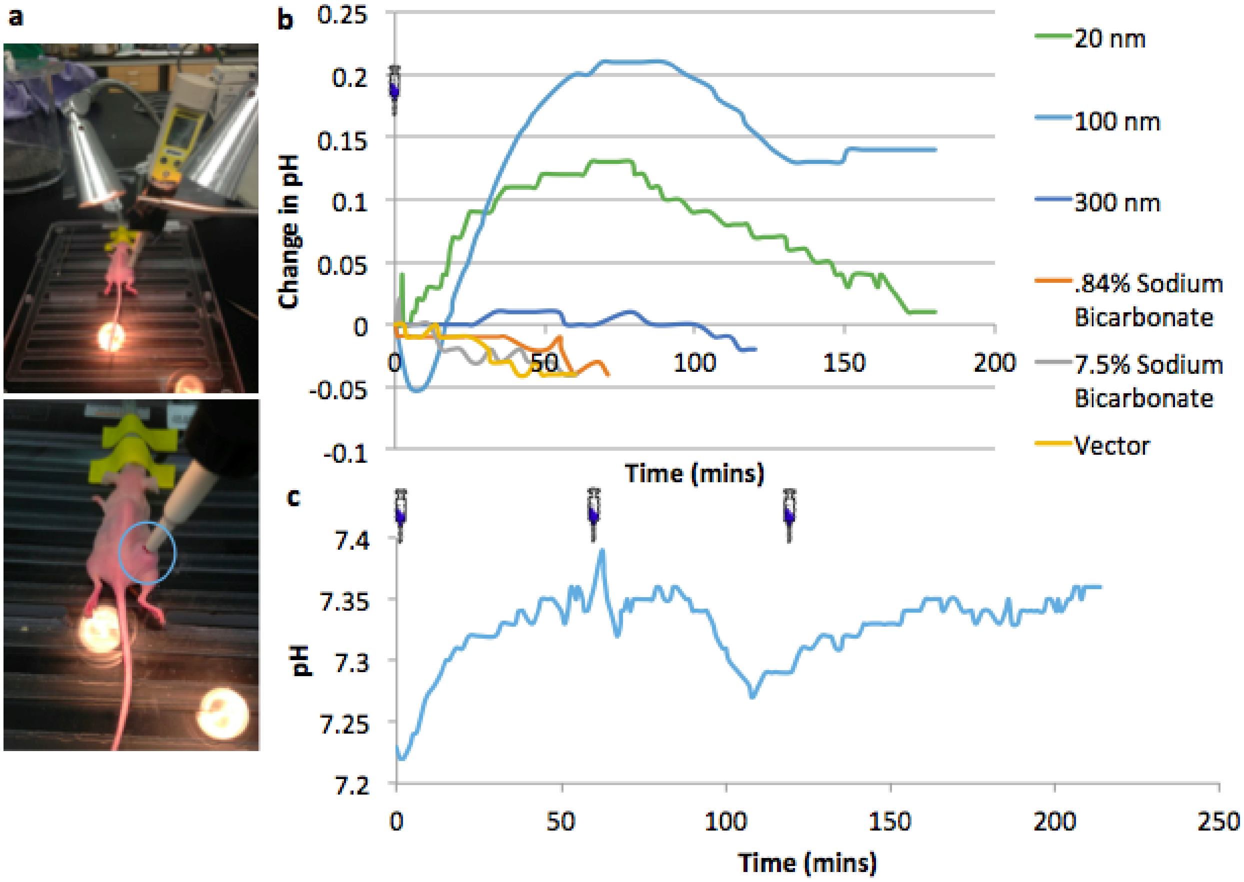

Fig. 6.3 I.V. injections of nano-$CaCO_3$ increase tumor pHe *in vivo* up to 7.4. (a) Image of pH measurement setup. Probe is ~ 5 mm deep into the tumor, and ~5 mm wide, suggesting that any pH value measured is most likely extracellular. (b) pH change *in vivo* with 1 mg bolus intravenous injections (time point of injection symbolized on the graph as an injection needle) of $CaCO_3$ particles, bicarbonate, or vector. (c) pH change with multiple injections of 100 nm particles in HT1080 tumor models demonstrate asymptotic changes near pH of 7.4.

6.3.2 Transient neutralization of the acidic pHe can inhibit tumor growth

The effect of persistent neutralization of the acidic pHe of solid tumors is not known at this time. Dynamic pH measurements in mice bearing HT1080 tumors indicate that 100 nm sized nanoparticles administered at a bolus dose of 1 mg (0.04-0.05 g/kg body weight) almost linearly increases the pH during the first 30 minutes, followed by a decrease at about 100 minutes. Repeated dosing at selected time points can maintain the pH close to 7.4 (Figure 6.3c), which matches the expectations of our simulation (Chapter 3).

Consistent with our hypothesis, we found that repeated daily administration of nano-$CaCO_3$ significantly inhibited tumor growth (Figure 6.4a,b). Further, discontinuation of the nano-$CaCO_3$ treatment partially reversed this trend, resulting in the acceleration of tumor growth rate (Figure 6.4c,d). This finding suggest the potential of tumor cell reprograming in response to an initial assault by nano-$CaCO_3$. Future studies will explore this concept. Our results suggest that if a therapeutic outcome using this method is envisaged, multiple doses of nano-$CaCO_3$ may be required to sustain the neutralizing effect until either depletion of the nanoparticles or reprogramming of the tumor cells in response to treatment. To achieve a sustainable tumor-inhibitory effect, it will be necessary to optimize dosing, combine nano-$CaCO_3$ with other therapies, and improve targeting of the nano-$CaCO_3$ to tumors.

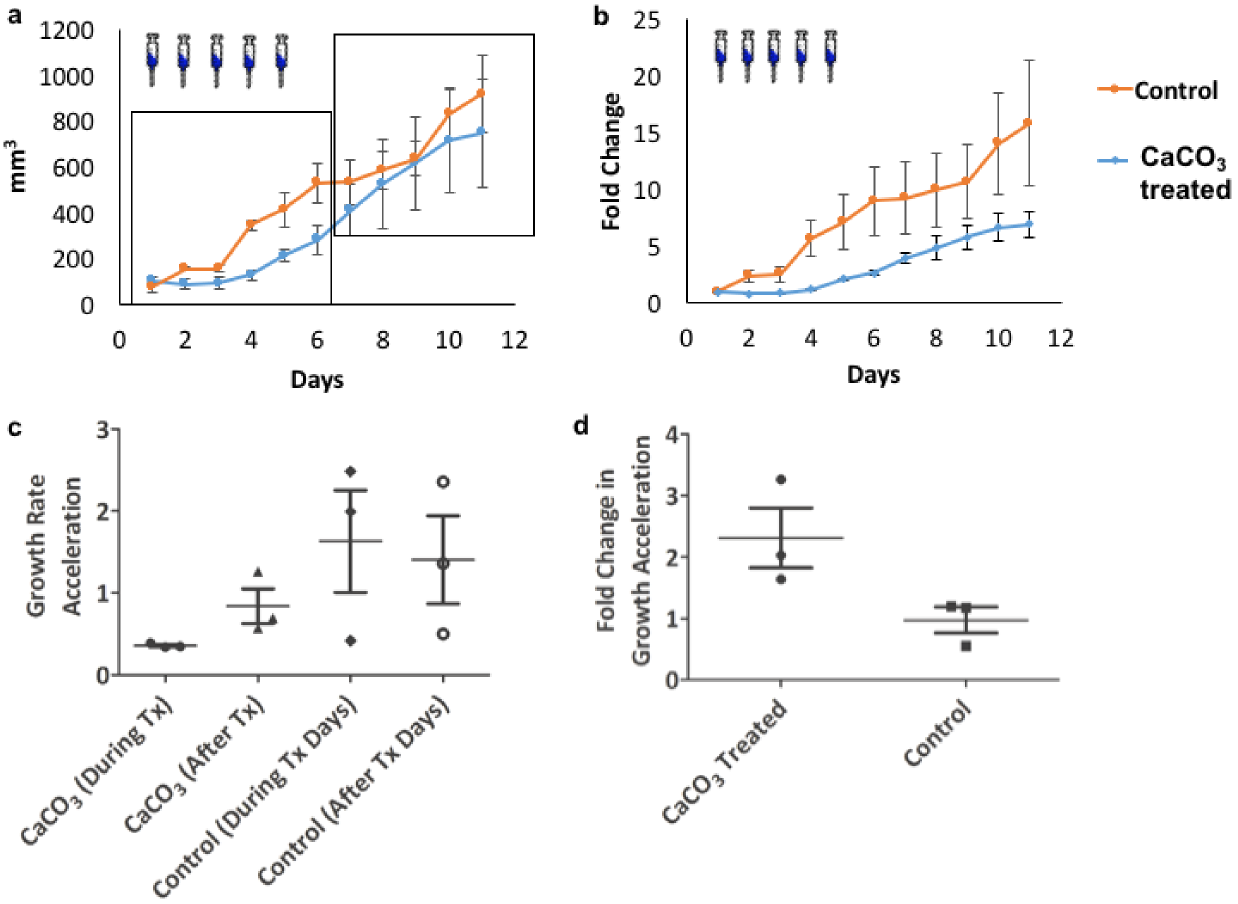

Fig. 6.4 Repeated administration of 100 nm nano-$CaCO_3$ inhibits tumor growth *in vivo*. (a), Tumor size during treatment (first box) is significantly lower than control, which partially equalizes after treatment ends (second box). (b), Controlling for initial size, the fold change in tumor size is significantly reduced in treated tumors. (c), Growth rate of treated tumors is decreased compared to control during treatments and only partially returns to normal after treatment removal. (d), Removal of $CaCO_3$ doubled the growth rate acceleration of the tumor after treatment removal, with little change in control over the same time period. Error bars represent standard error. Error bars refer to standard error with an n= 3 biologic replicates for each arm.

6.3.2 Persistent neutralization of pH via infusion of $CaCO_3$ can inhibit growth and metastasis.

$CaCO_3$ infusion induces a persistent amount of $CaCO_3$ buffer in the blood stream. Under these conditions, we find metastasis is inhibited significantly via both the orthotopic and IV infusion model. In particular we find that the orthotopic tumor is significantly inhibited in growth. Based on the results of the IV infusion model, we note that the particles may have some inhibition of the extravasation step. Based on the results of the orthotopic model suggests that $CaCO_3$ may have an effect on metastasis by both an effect on intravasation and extravasation. (Figure 6.5)

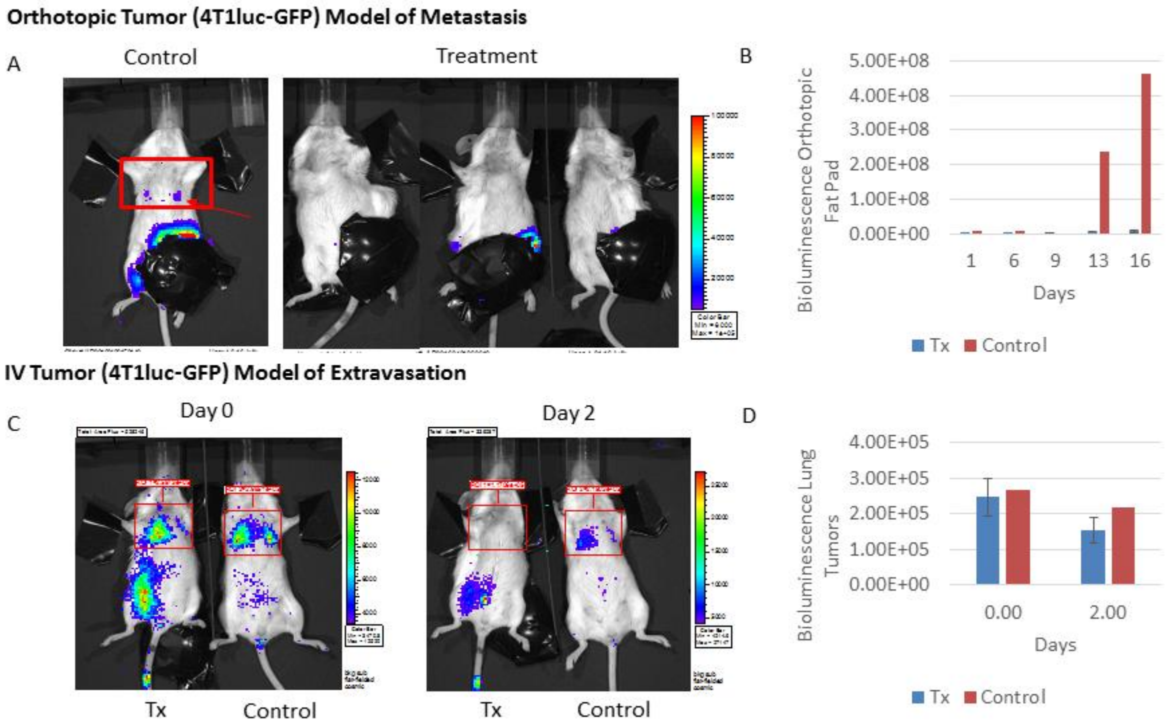

Fig. 6.5 Continuous $CaCO_3$ infusion inhibits tumor growth and metastasis. (a) Tumor metastasis can be seen in control versus lack therof in treatment mice in the orthotopic 4T1 model. (b) Orthotopic tumor growth in control versus treatment. (c) Reduction in tumor extravasation in an IV model of metastasis under $CaCO_3$ control vs treatment. (d) Quantification of the reduction in lung bioluminescence immediately post injection of 4T1luc GFP tumor cells and 2 days later.

6.4 Discussion

We have identified a facile, scalable method for mass production of sub-micron vaterite calcium carbonate nanoparticles that are stable in biological media. Two different methods wherein particle nucleation and cluster growth could be effectively controlled was demonstrated to obtain the desired size ranges and crystal phases of calcium carbonate nanoparticles. (Chapter 4) For the first time, we have demonstrated the capability of modulating the pH of solid tumors using nano-$CaCO_3$. Efficient neutralization of the acidic pHe of tumors depends on particle size. Our results suggest that large (> 300 nm) and small (< 20 nm) particles are less effective in neutralizing pHe in vivo because of limited diffusion and transient retention in the tumor environment, respectively. The ability of nano-$CaCO_3$ to inhibit tumor growth and metastasis in vivo could serve as a treatment paradigm for long-term tumor static therapy. Future studies will focus on dose optimization, enhancement of tumor-targeting capability, determination of synergistic treatments with complementary therapies, and assessment of potential tumor cell reprograming following nano-$CaCO_3$ treatment. A summary of all experiments in this chapter and above can be seen in Table 6.1.

Table 6.1: Experimental plan to develop nano $CaCO_3$ for modulating pH in tumors

Experiment	**Objective/hypothesis**	**Techniques**	**Notes**
Simulation of $CaCO_3$ dissolution in vivo	To analyses pH transition with μm resolution	MATLAB	Simulation of nano $CaCO_3$ dissolution *in vivo*

Synthesis of $CaCO_3$ nanoparticles	Synthesis of 20 nm, 100 nm and 300 nm	Sol-gel synthesis, gas diffusion synthesis	Morphological controlled nanoparticle synthesis
Characterization of nanoparticles	Morphology, zeta potential	TEM, DLS	Fractal nature and hydrodynamic diameter
	Crystal nature	XRD	Vaterite
Aqueous Solvent Identification	Stability of nanoparticles	TR-DLS, TEM, XRD	Using different vector system
In vitro cell free testing of nano-$CaCO_3$	Test the kinetics and dose response pH neutralization in cell free conditioned media and serum	pH probe	$CaCO_3$ dissolution and pH changes in conditioned media
In vitro cell incubation with particles	Dose response on pH change post incubation period with cells	pH probe, HT1080 Cell culture	To verify the experimental results of cell free experiments with cells
In vivo testing of nano-$CaCO_3$	pH changes in vivo post bolus particle IV injection	HT1080 tumors,	

		ncr/ncr nude balb/c mice	To verify pH modulating in model organism
	pH increases post multiple injections	HT1080 tumors, ncr/ncr nude balb/c mice	
	Demonstrate decrease in tumor growth from the increase in pHe over time in immunodeficient mice	HT1080 tumors, ncr/ncr nude balb/c mice	Tumor growth rate is inhibited with CaCO$_3$ that partially reverses with removal
	Demonstrate inhibition in tumor growth and metastasis from the increase in pHe over time in immunocompetent mice with continuous infusion	4T1luc-GFP tumors, Balb/c mice	Metastasis and tumor growth is inhibited with CaCO$_3$ continuous infusion.

A shortcoming of our study is the difficulty in using an invasive method to determine in vivo pHe, which could affect the accuracy of the pH measurement. Additionally, repeated measurements requiring removal and replacement of the pH probe is cumbersome and prone to error. These challenges could be addressed by developing a precise and accurate noninvasive imaging approach to measure pH longitudinally.

6.5 Copyright acknowledgment

All figures and written work was taken in whole or in part from the following manuscripts:

Avik Som, Ramesh Raliya, Limei Tian, Walter Akers, Joseph E. Ippolito, Srikanth Singamaneni, Pratim Biswas, and Samuel Achilefu. **“**Monodispersed calcium carbonate nanoparticles modulate local pH and inhibit tumor growth *in vivo” Nanoscale,* December 2015.

6.6 References

1 Bellone, M. *et al.* The acidity of the tumor microenvironment is a mechanism of immune escape that can be overcome by proton pump inhibitors. *Oncoimmunology* **2**, doi:10.4161/onci.22058 (2013).

2 Robey, I. F. *et al.* Bicarbonate increases tumor pH and inhibits spontaneous metastases. *Cancer Res* **69**, 2260-2268, doi:10.1158/0008-5472.CAN-07-5575 (2009).

3 Marion Stubbs, P. M. J. M., John R. Griffiths, and C. Lidsay Bashford Causes and Consequences of tumour acidity and implications for treatment. *Molecular Medicine Today* **6**, 15-19 (2000).

4 Robey, I. F. & Nesbit, L. A. Investigating mechanisms of alkalinization for reducing primary breast tumor invasion. *Biomed Res Int* **2013**, 485196, doi:10.1155/2013/485196 (2013).

5 Calcinotto, A. *et al.* Modulation of microenvironment acidity reverses anergy in human and murine tumor-infiltrating T lymphocytes. *Cancer Res* **72**, 2746-2756, doi:10.1158/0008-5472.CAN-11-1272 (2012).

6 Neri, D. & Supuran, C. T. Interfering with pH regulation in tumours as a therapeutic strategy. *Nat Rev Drug Discov* **10**, 767-777, doi:10.1038/nrd3554 (2011).

7 Supuran, C. T. Inhibition of carbonic anhydrase IX as a novel anticancer mechanism. *World J Clin Oncol* **3**, 98-103, doi:10.5306/wjco.v3.i7.98 (2012).

8 Amin, M. R., Postma, G. N., Johnson, P., Digges, N. & Koufman, J. A. Proton pump inhibitor resistance in the treatment of laryngopharyngeal reflux. *Otolaryngol Head Neck Surg* **125**, 374-378, doi:10.1067/mhn.2001.118691 (2001).

9 Logue, J. S. & Morrison, D. K. Complexity in the signaling network: insights from the use of targeted inhibitors in cancer therapy. *Genes Dev* **26**, 641-650, doi:10.1101/gad.186965.112 (2012).

10 Martin, N. K. *et al.* Predicting the safety and efficacy of buffer therapy to raise tumour pHe: an integrative modelling study. *Br J Cancer* **106**, 1280-1287, doi:10.1038/bjc.2012.58 (2012).

11 Schroeder, A. *et al.* Treating metastatic cancer with nanotechnology. *Nature reviews. Cancer* **12**, 39-50, doi:10.1038/nrc3180 (2012).

12 Yang, S. & May, S. Release of cationic polymer-DNA complexes from the endosome: A theoretical investigation of the proton sponge hypothesis. *J Chem Phys* **129**, 185105, doi:10.1063/1.3009263 (2008).

13 Ueno, Y., Futagawa, H., Takagi, Y., Ueno, A. & Mizushima, Y. Drug-incorporating calcium carbonate nanoparticles for a new delivery system. *Journal of controlled release : official journal of the Controlled Release Society* **103**, 93-98, doi:10.1016/j.jconrel.2004.11.015 (2005).

14 Jinhuan Wei *et al.* The inhibition of human bladder cancer growth by calcium carbonate/CalP6 nanocomposite parrticles delivering AIB1 siRNA. *Biomaterials* **34**, 1246-1354 (2013).

15 Gallagher, F. A. *et al.* Magnetic resonance imaging of pH in vivo using hyperpolarized 13C-labelled bicarbonate. *Nature* **453**, 940-943, doi:10.1038/nature07017 (2008).

16 Zoonens, M., Reshetnyak, Y. K. & Engelman, D. M. Bilayer interactions of pHLIP, a peptide that can deliver drugs and target tumors. *Biophys J* **95**, 225-235, doi:10.1529/biophysj.107.124156 (2008).

Chapter 7. Conclusions and Future Directions

7.1 Conclusions

The extracellular pH of cancer remains a hallmark worth manipulating for cancer treatment. Prior to this work, it had been difficult to modulate pH in tumors in a sustainable fashion in vivo without significant side effects for long durations.[1-7] In this thesis we describe the importance of pH on the extracellular environment in cancer and demonstrate the development of a nanomaterial method to modulate this pH in vivo. This new tool enables both providers and researchers to practically tackle the question of extracellular pH modification. We discover that the use of the novel nanomaterial (nano-$CaCO_3$) does have a significant therapeutic effect on both tumor growth and metastasis, at dosage levels of carbonate that are almost 8000x smaller than by oral systemic dosing of aqueous sodium bicarbonate. [1,3] In the process, we present new biological observations, diffusion and dissolution modeling of nanomaterials, novel material synthesis methods, new MR contrast agents for bio distribution profiling, and the use of nanomaterials in osmotic pumps for continuous administration.

The observation of OCT-4 expression under acidic stress in fibroblast stromal cells is significant in that it demonstrates how the acidic pH generated by tumors has a functional effect on its surroundings. The implications of this observation remain significant, including a potential avenue to explain the recruitment of stromal cells to the tumor microenvironment. Perhaps further interesting is how widespread the phenomenon appears, in multiple solid tumor types, further emphasizing the ubiquity of pH and its downstream effects as a hallmark of cancer.

The mathematical modeling of $CaCO_3$ dissolution *in vivo* is one of only a few studies describing modeling of a nanomaterials. [8-11]The subsequent studies validate the model's prediction, primarily that $CaCO_3$ despite having a pKa of 9, *in vivo*, retains a physiological pH sensitivity to 7.4. It also implies significant things about the proposed biodistribution and pH maintenance paradigms that influenced doping schedule. For instance, because there is a stable point at 7.4, raising the pH itself to 7.4 may require substantial amounts of nanoparticle, but maintaining the pH requires very little, only enough to remove any newly produced acid. Importantly this also meant that under continuous infusion, the first bolus would be used primarily to increase pH, with subsequent dosages only serving to increasing the buffering capacity of the tissue. Continuous presence of a small amount $CaCO_3$ nanoparticles thus is very important to maintain this equilibrium. The pH dropping again would mean the entire process has to start over. This fundamental prediction influences the usage of the continuous osmotic pump and helps explains the significantly greater growth inhibition under continuous infusion than daily bolus injections.

The synthesis of nano-$CaCO_3$ required a new way to develop and stabilize nano-crystals. Carbonate nano-crystals in particular are hard to make and grow because of their propensity to fuse and become larger. Interestingly, in the process of development, we discover a vacuum diffusion method where the size is actually a function of the ammonium bicarbonate nanocrystals. This result means that we can make carbonate nanocrystals of a number of metals as shown by the formation of $AuCO_3$, $FeCO_3$, and $ZnCO_3$.

An important component of making pH modulation a practical therapeutic modality was toxicity and biodistribution. Via this section, we demonstrate the production, characterization and imaging of $CaCO_3$-magnetite which identified $CaCO_3$ as undergoing an approximately 24 hour clearance pattern. Toxicity studies with rats also demonstrate the safety of $CaCO_3$ suggesting further its capability to be a practical therapeutic modality.

Further studies then looking a pH increases demonstrate how $CaCO_3$ injection induces a localized increase in pH at the tumor site that only goes up to 7.4. The therapeutic implications are seen both in a serial injection model of a fibrosarcoma, and a continuous infusion model of syngeneic breast cancer model. We see both growth inhibition and importantly metastasis inhibition. This effect validates what was seen during systemic administration of base albeit without the toxic side effects of metabolic alkalosis.

7.2 Future Work

Further work remains to be done to continue the story and make the therapeutic modulation of pH a viable therapeutic modality in the clinic. These studies can be roughly divided into explorations of biology and biological effects, as well as advances in the material science.

Focusing on the biology, further studies will explore whether the nano-$CaCO_3$ induced pH increase causes downstream biological effects on both the tumor and surrounding stroma, including OCT-4 expression observed as being caused by extracellular acidity. With this tool, many of the earlier *in vitro* studies on pH can be validated *in vivo.* Identification of changes in protein expression and RNA/DNA expression of both the stroma and tumor cells will guide subsequent therapeutic questions. The synergy with other therapies is an entirely separate field of study that will be exciting to dive into. Already, we know that several chemotherapies have significant susceptibility to extracellular pH. Increasing pH may synergistically increase those chemotherapies effectiveness.

Focusing on the materials science, further work is needed on methodology for scaling the materials, develop of an appropriate pump to distribute longer than 1 month. A larger pump for larger animals will be needed to demonstrate benefit. Alternative delivery methods, including peritoneal administration, remains possible and unexplored. Nano-$CaCO_3$ remains unadorned. Although this is valuable for systemic nonspecific administration, this means further work is necessary to add a targeting capability to the particle, including adding a coating, and/or a targeting group, potentially increasing the retention of nano-$CaCO_3$. The development of other carbonates such as gold carbonate, zinc carbonate, and iron carbonate, may have utility on both the extracellular pH in cancer, but also applications throughout the sciences. Further work is necessary to characterize these other carbonate nanocrystals for their properties.

Excitingly, nano-$CaCO_3$ lays a foundation for significant headway into a number of biological questions regarding modifying pH in cancer, and advancing the field of material science for nanocrystal design and engineering. Perhaps most importantly, nano-$CaCO_3$ enables the practical application of a novel therapeutic modality: increasing the extracellular pH in cancer.

7.3 References

1 Robey, I. F. *et al.* Bicarbonate increases tumor pH and inhibits spontaneous metastases. *Cancer Res* **69**, 2260-2268, doi:10.1158/0008-5472.CAN-07-5575 (2009).

2 Robey, I. F. & Martin, N. K. Bicarbonate and dichloroacetate: evaluating pH altering therapies in a mouse model for metastatic breast cancer. *BMC Cancer* **11**, 235, doi:10.1186/1471-2407-11-235 (2011).

3 Martin, N. K. *et al.* Predicting the safety and efficacy of buffer therapy to raise tumour pHe: an integrative modelling study. *Br J Cancer* **106**, 1280-1287, doi:10.1038/bjc.2012.58 (2012).

4 Robey, I. F. & Nesbit, L. A. Investigating mechanisms of alkalinization for reducing primary breast tumor invasion. *Biomed Res Int* **2013**, 485196, doi:10.1155/2013/485196 (2013).

5 Luciani, F. *et al.* Effect of proton pump inhibitor pretreatment on resistance of solid tumors to cytotoxic drugs. *J Natl Cancer Inst* **96**, 1702-1713, doi:10.1093/jnci/djh305 (2004).

6 Calcinotto, A. *et al.* Modulation of microenvironment acidity reverses anergy in human and murine tumor-infiltrating T lymphocytes. *Cancer Res* **72**, 2746-2756, doi:10.1158/0008-5472.CAN-11-1272 (2012).

7 Bellone, M. *et al.* The acidity of the tumor microenvironment is a mechanism of immune escape that can be overcome by proton pump inhibitors. *Oncoimmunology* **2**, doi:10.4161/onci.22058 (2013).

8 J. Siepmann , A. G. Mathematical modeling of bioerodible, polymeric drug delivery systems. *Advanced drug delivery reviews* **48**, 229-247 (2001).

9 Arifin, D. Y., Lee, L. Y. & Wang, C. H. Mathematical modeling and simulation of drug release from microspheres: Implications to drug delivery systems. *Advanced drug delivery reviews* **58**, 1274-1325, doi:10.1016/j.addr.2006.09.007 (2006).

10 Lin, C. C. & Metters, A. T. Hydrogels in controlled release formulations: network design and mathematical modeling. *Advanced drug delivery reviews* **58**, 1379-1408, doi:10.1016/j.addr.2006.09.004 (2006).

11 Cruz, L. *et al.* Diffusion and mathematical modeling of release profiles from nanocarriers. *International journal of pharmaceutics* **313**, 198-205, doi:10.1016/j.ijpharm.2006.01.035 (2006).